ELECTRICAL CONTACTS TO P-TYPE ZINC SELENIDE

By

JOHN JOSEPH FIJOL

A DISSERTATION PRESENTED TO THE GRADUATE SCHOOL
OF THE UNIVERSITY OF FLORIDA IN PARTIAL FULFILLMENT
OF THE REQUIREMENTS FOR THE DEGREE OF
DOCTOR OF PHILOSOPHY

UNIVERSITY OF FLORIDA

1996

ACKNOWLEDGMENTS

First and foremost, I must thank my wife, Sheryl. For four years she put her life on hold so that I could attend graduate school. During this time her support and patience have been a steady source of motivation to finish my graduate studies. Now that it is finished, we can finally move home.

I must also thank Dr. Paul Holloway, who has been a source of inspiration to me since I began investigating schools for graduate study. Over the years he has provided outstanding guidance and support, distinguishing himself as a professor who values education above personal gain. Working under him I have come to understand that the knowledge you take with you is not nearly as important as your desire and ability to learn.

Many people have helped with the work presented in this dissertation and deserve recognition. At the University of Florida, J. Kim and Dr. Jones helped with TEM analysis, L. Calhoun and Dr. Park grew samples, Dr. Lambers helped with Auger analysis and Dr. Puga-Lambers helped with SIMS analysis. At 3M corp. in St. Paul, Minnesota, P. Baude also grew samples and at AT&T in Orlando, Florida, F. Stevie assisted with FIB preparation of cross sectional TEM samples. I would also like to thank ARPA for funding this research.

Finally I would like to thank Dr. G. William Tasker, my former supervisor at Galileo Electro-Optics. While working under him, he repeatedly encouraged me to return to school to pursue a doctoral degree. Without his insistence and belief in my abilities, I may never have attended graduate school.

TABLE OF CONTENTS

page

ACKNOWLEDGMENTS....ii

ABSTRACT....v

CHAPTERS

1 INTRODUCTION....1

2 REVIEW OF THE LITERATURE....6

- Schottky and Ohmic Contacts....6
- Metallic Contacts to p-ZnSe....13
- HgSe Contacts to p-ZnSe....20
- ZnTe/ZnSe Contacts to p-ZnSe....23

3 Au AND Ag CONTACTS....40

- Introduction....40
- Experimental Setup....40
- Results....46
  - Sputtered Au Contacts....46
  - Sputtered Ag Contacts....48
  - Evaporated Ag Contacts....49
- Discussion....50
  - Au Contacts....50
  - Ag Contacts....54
- Summary....57

4 HgSe CONTACTS....73

- Introduction....73
- Experimental Setup....73
- Results....79
- Discussion....83
  - HgSe Formation....83
  - Electrical Characterization....86
  - Summary....91

5 DEGRADATION STUDIES OF MULTIQUANTUM WELL CONTACT..108

Introduction..108
Experimental Setup...108
Results...115
    Electrical Degradation..115
    Au Probe..117
    Cu Probe..118
    Silver Paint Electrical Probes................................124
    Heat treated Samples..125
    Post Degradation Surface Reactions....................126
Discussion..127
    Diffusion of Zn and Te..127
    Thermal Stress..129
    Impurity Diffusion and Blisters in Region II..........133
    Rectangular Raised Features in Region III..........136
    High Temperature Effects......................................141
    MQW Contact Degradation and DLDs.................143
    Effects of Contact area...144
    Post Degradation Surface Reactions....................144
Summary...145

6 CONCLUSIONS...186

Metal Contacts..186
HgSe Contacts...189
Multiquantum Well Contacts..191

7 FUTURE WORK..196

Au and Ag Contacts...196
HgSe Contacts...197
Multiquantum Well Contacts..199

REFERENCES...202

BIOGRAPHICAL SKETCH...208

Abstract of Dissertation Presented to the Graduate School
of the University of Florida in Partial Fulfillment of the
Requirements for the Degree of Doctor of Philosophy

ELECTRICAL CONTACTS TO P-TYPE ZINC SELENIDE

by

JOHN JOSEPH FIJOL

May, 1996

Chairman: Dr. Paul Holloway
Major Department: Material Science and Engineering

The electrical properties and structure of three different electrical contacts to p-ZnSe were studied. Sputter deposited Au and Ag contacts were heat treated over a range of 150 to 400 °C to determine the effect of heat treatments on the reverse bias breakdown voltage of these Schottky contacts. The minimum breakdown voltage for Au contacts was found to be ~3 volts following heat treatment at 350 °C for 30 minutes. Analytical data indicated that Au diffused into the ZnSe during heat treatment, resulting in the formation of deep acceptor levels which led to defect assisted avalanche breakdown dominating conduction. The minimum reverse bias breakdown voltage for Ag contacts was found to be 2.3 volts following heat treatment at 150 °C for 45 minutes. Analytical data indicated that oxygen was incorporated at the Ag/ZnSe interface during deposition and heat treatment which co-doped the surface region of the ZnSe and led to field emission dominating conduction.

The electrical properties and conduction mechanisms of HgSe/p-ZnSe contacts were also studied. These contacts were formed by a novel *ex situ* process which involved capping the ZnSe with amorphous Se, diffusion of Hg into the Se to form a solid solution, and precipitation of HgSe from solution. Auger, secondary ion mass spectrometry and transmission electron microscopy showed that this process yielded a stoichiometric HgSe layer with regions epitaxed to the underlying ZnSe. Temperature dependant measurements showed that the valence band offset between HgSe and ZnSe was 0.55 eV.

The degradation of ZnTe/ZnSe multiquantum well contacts under high current loading (1000 to 1500 A/cm^2) were also studied. Localized temperatures during degradation was measured to be 300 °C or greater at the point where electrical power was supplied. Auger data from degraded samples indicated that due to the localized heating, Zn and Te from the ZnTe layers and Zn from the ZnSe layers diffused through the Au metallization to the sample surface. In addition, thermal stress from the localized heating generated micro-cracks in the ZnSe which acted as high diffusivity paths for impurities. Rectangular defects oriented to the micro-cracks had similar geometries to dislocation patches (dark line defects) which form in the quantum well region of degraded ZnSe based laser devices. This suggests the formation of similar dislocation patches in the quantum well region of the multiquantum well contacts.

CHAPTER 1

INTRODUCTION

There is currently a strong desire to fabricate opto-electric devices which emit light in the blue region of the visible spectrum for applications such as optical data storage and flat panel displays. The present optical storage industry is dominated by AlGaAs/GaAs based devices which operate in the near infrared region. The need to replace infrared devices with blue light emitting devices arises because shorter wavelengths (blue) can be focused to half the minimum spot sizes of longer wavelengths (near infrared), yielding the ability to write four times as much data in the same surface area [And93]. Another potential and growing application for blue light emitting materials and devices is for use in full color displays [Wer94]. This need for materials which emit in the blue region with high brightness and efficiency has stimulated significant research, but the materials and devices have been difficult to develop.

One of the more promising materials for use in blue light emitting applications is zinc selenide (ZnSe). ZnSe is a II-VI compound semiconductor which has a zincblende structure, a 5.668 **Å** lattice parameter [Wea76], a band gap of 2.67 eV [Shi80] and an electron affinity of 4.09 eV [Swa66], at room temperature. The ability to produce n-type ZnSe by chlorine doping has been possible for many years and is commonly used during molecular beam epitaxial (MBE) growth of n-ZnSe [Ohk87, Ren91, Ohk92]. However, the ability to reproducibly dope ZnSe p-type was reported in 1990 [Par90]. This process, demonstrated by Park and coworkers, used nitrogen gas (N_2), which is dissociated by an RF discharge, as the dopant source during MBE growth of p-type ZnSe. The availability to produce both n and p-type doping techniques has lead to the fabrication of ZnSe based light emitting diodes (LEDs) [Qui93, Fan92] and laser diodes (LDs) [Fan92, Haa91, Gai93] which emit in the blue to green regions with wavelengths of 490 nm to 516 nm.

Although ZnSe devices have been demonstrated, there are still many areas which require further advancement before commercial devices can be manufactured and marketed. One of the more critical problems facing ZnSe based LEDs and LDs is their short lifetimes under both pulsed and continuous wave (cw) operation. Currently the highest pulsed output power (~0.5 watts), highest operating temperature (394 K), and lowest threshold current (2.5 mA) for laser devices have been obtained from devices based on a single quantum well (QW) design which consists of a strained CdZnSe layer between ZnMgSSe/ZnSeS confinement layers [Zor93]. Work performed by S. Guha et al. [Guh94] indicates that degradation in these devices occurs by the "emission" of dark line defects (DLDs) along the <001> direction which grow into patches of dislocations along the <011> direction. In addition to short lifetimes, other problems arise from the fact that free hole levels in p-type ZnSe typically plateau in the 10^{17} cm^{-3} range, reportedly due to the formation of self compensating defects [Woo90, Qui91]. These doping limitations have led to difficulties in forming ohmic contacts. Since poor contact performance is believed to be a contributing factor to poor device lifetimes, several studies, including the present, have focused on establishing a simple and reliable method of forming long-lived, robust ohmic contacts to p-type ZnSe.

An ohmic contact is a non-rectifying metal/semiconductor contact which exhibits linear current vs voltage characteristics and has a negligible resistance in comparison to the bulk resistance of the semiconductor. Ohmic contacts allow power to be efficiently applied to the active region of the device as opposed to being consumed in the contacts. Identifying a process for forming ohmic contacts to p-ZnSe has proven to be a difficult task, due to the properties and processing limitations of ZnSe. Significant effort has been expended studying conventional metal contact schemes to p-ZnSe, but these have not resulted in the formation of ohmic contacts. These efforts and the fundamental problems associated with ohmic contact formation to p-ZnSe will be discussed in chapter two which is a review of the literature.

The inability to form ohmic metallizations to p-ZnSe has lead to the use of more elaborate techniques. The first pseudo-ohmic contacts developed were based on mercury selenide (HgSe) which is a narrow gap semimetal [Lan92]. In addition, contact schemes have been identified which are based on alternating layers of ZnTe and ZnSe arranged in pseudograded [Fan92] or multiquantum well [Hie93] structures. Both the HgSe and ZnTe/ZnSe contacts will also be discussed in more detail in chapter two.

The tremendous interest in developing ZnSe devices has lead to many researchers contributing to ohmic contact research, leading to rapid progress over the past several years. The research in this dissertation focused on three different contacts schemes. This work is described in chapters three, four, and five of this dissertation, with the electrical characterization of Au and Ag contacts to p-type ZnSe presented in chapter three. For these metals, heat treatments were identified which reduced the metal contact's reverse bias breakdown voltage (V_B) and the composition and structure of the contacts were analyzed to identify changes, induced by the heat treatments, which led to the reduction in $V_{B.}$ In chapter four, results from a second rectifying contact scheme, based on HgSe contacts, is reported. This work focussed on the characterization of mercury selenide (HgSe) contacts formed by a novel *ex situ* process. HgSe/p-ZnSe contacts, which are know to have a small valence band offset (ϕ_B) [Fan92], were formed by reacting a Se capping layer (on p-ZnSe) with Hg vapor to form HgSe. These contacts were found to have a lower ϕ_B than Au and Ag metallizations, but were not ohmic.

Although significant progress has been made in reducing the rectifying properties of metal and semimetal contacts and researchers are still studying both, the ZnSe/ZnTe contacts are currently the most promising solution [Fan92, Hie93]. Since further refinement of ZnSe devices requires reliable, low resistance contacts, chapter five reports work focused on refining ZnSe/ZnTe contacts. As will be described, observations at 3M Company indicate that high current densities (>30 A/cm^2) cause the formation of DLDs (which quench the light output in opto-electric devices) and failure of ZnSe/ZnTe contacts [bau95]. Therefore, the degradation of ZnTe/ZnSe contacts was characterized to provide a thorough understanding of their performance, longevity, and failure mechanisms. Conclusions from these studies are summarized in chapter six and suggested future research is discussed in chapter seven.

CHAPTER 2

REVIEW OF THE LITERATURE

Schottky and Ohmic Contacts

When metal/semiconductor contacts are formed, they commonly result in rectifying Schottky contacts which inhibit current flow across the metal/semiconductor interface [Sch38]. When an intimate electrical contact is made between a metal and a semiconductor, the Fermi level (E_f) in the two materials equilibrate and the vacuum level is continuous, as shown for a metal/n-type semiconductor interface in figure 2.1. This leads to bending of the conduction and valence bands in the semiconductor, which results in a barrier (ϕ_B) that impedes conduction of charge carriers from the metal to the semiconductor. When ohmic contact behavior is required, careful selection of contact materials, surface modifications, interfacial reactions, or the formation of unique structures are required to insure the free flow of charge carriers across the interface. As a result, a review of conduction mechanisms in Schottky contacts is helpful to understand the development of ohmic contacts. In particular, the reverse bias conduction mechanisms,since this will restrict the current flow in our measurements.

There are four conduction mechanisms for reverse biased Schottky contacts: thermionic emission, field emission, electron-hole generation, and minority carrier injection [Sha84, p. 35]. Electron-hole generation and minority carrier injection typically dominate for low carrier concentrations and are rarely utilized in ohmic contacts. However, thermionic or field emission conduction can be utilized, through careful design, to yield ohmic behavior from otherwise Schottky contacts. The expressions describing the thermionic emission currents in a reversed bias Schottky diode were originally developed by Wagner [Wag31], and Schottky and Spenke [Sch39] and are as follows:

$$I = I_o\,[\exp(-qV_R/kT)-1] \qquad (2\text{-}1)$$

where,

$$I_o = SA^*T^2 \exp(\Delta\phi_B-\phi_B/kT) \qquad (2\text{-}2)$$

and,

$$A^* = 4\pi m^* qk^2/h^3. \qquad (2\text{-}3)$$

In these equations, q is the charge on an electron, V_R is the applied reverse bias, k is Boltzmans' constant, T is temperature, S is the contact area, ϕ_B is the barrier height, m* is the charge carrier effective mass, and h is Planck's constant. A* is the Richardson constant, and $\Delta\phi_B$ results from several mechanisms such as image force reduction or by thin oxides (or interfacial layers) between the metal and semiconductor which are sufficiently thin for tunneling to occur (< 20 Å). While thin oxides are not always present, barrier lowering from image force reduction affects all Schottky contacts and may be calculated as follows [Sha84, p. 51]:

$$\Delta\phi_B=[(q^3N_d/8\pi\epsilon_d^2\epsilon_s)(V_i+V_R)]^{1/4}. \qquad (2\text{-}4)$$

Here, N_d is the carrier concentration in the semiconductor, ϵ_d is the dielectric constant in the depletion region, ϵ_s is the dielectric constant in the bulk semiconductor ($\epsilon_d \approx \epsilon_s$), and V_i is the built in potential of the barrier. From the equations above, the reverse bias saturation current can be greatly increased (leading to ohmic behavior) by reducing ϕ_B. Thermionic emission currents in reverse bias Schottky contacts are typically described by one of two conduction mechanisms: thermionic field emission or tunneling. Thermionic field emission usually occurs with lower carrier concentrations when the barrier ϕ_B is wide near the base (low energy above E_f) but is sufficiently thin for tunneling to occur near the top (high energy above E_f). Charge carriers which gain sufficient thermal energy to reach the thin region of the barrier have a high probability of tunneling through the barrier. In the case of high carrier concentrations, the barrier width becomes sufficiently thin at the base for charge carriers to tunnel directly through. Field emission currents in reversed bias Schottky contacts were initially modeled by Padovani and Stratton [Pad66], who developed the following relationship;

$$I = SJ_s \exp(-qV_R/E') \qquad (2\text{-}5)$$

where,

$$J_s = (A^*(\pi E_{oo})^{1/2}/kT)[-qV_R+(\phi_B/\cosh^2(E_{oo}/kT)]^{1/2} \exp(-\phi_B/E_o), \qquad (2\text{-}6)$$

$$E' = E_{oo}[(E_{oo}/kT)-\tanh(E_{oo}/kT)]^{-1}, \qquad (2\text{-}7)$$

$$E_o = E_{oo} \coth(E_{oo}/kT) \qquad (2\text{-}8)$$

and

$$E_{oo} = qh/4\pi(N_d/m^*\varepsilon_s)^{1/2}. \qquad (2\text{-}9)$$

Here, N_d is the semiconductor carrier concentration, and ε_s is the dielectric constant of the bulk semiconductor. This set of equations describes both thermionic field emission and tunneling. If E_{oo} is small in comparison to kT, then the field emission current is dependant on temperature and thermionic field emission will occur. In contrast, if E_{oo} is large in comparison to kT, then the field emission current is relatively independent of temperature and tunneling will occur. Either thermionic field emission or tunneling can result in contact impedances which are sufficiently lower than the bulk resistance of the semiconductor so that ohmic behavior is achieved.

In the early 70's, Sze established criteria for the formation of ohmic contacts based on the observations indicated above [Sze85, p. 196]. These criteria provide categorization of ohmic contacts into two types, depending upon the semiconductors doping level. For semiconductors with low carrier concentrations (<10^{18} carriers/cm^3), conduction across the interface is dominated by thermionic emission as described by Schottky. Therefore, to achieve ohmic behavior in low doped semiconductors, there must be a low ϕ_B for majority carriers. In n-type semiconductors, E_f is near the bottom of the conduction band edge (E_c), therefore to minimize the interfacial barrier height for majority carriers (electrons) a contact metal must be chosen with a work function (ϕ_m) which is approximately equal to or less than the semiconductors electron affinity (χ_s). Since the work function of the metal and semiconductor are matched, ϕ_B is minimized which allows free flow of charge carriers (Fig. 2.2a). For p-type semiconductors E_f is near the top of the valence band edge (E_v), therefore to minimize ϕ_B, ϕ_m must be approximately equal to the semiconductor's band gap (E_g) plus χ_s (Fig 2.2b). This minimizes bending of the valence band in the semiconductor, leading again to a low ϕ_B and free flow of charge carriers (holes). It is important to note that this approach to forming ohmic contacts by matching ϕ_m and χ_s (or χ_s+E_g) only applies to semiconductors without Fermi level pinning. Pinning may be caused by interface or near-surface defect states [Sha84, p. 8].

Defect states commonly occur on the surface of semiconductors which have predominantly covalent bonding (such as Si and GaAs). These defect states, as originally described by Bardeen [Bar47], have a number of origins including impurities and interruption of the crystal lattice. Atoms at the surface of the semiconductor are missing neighboring atoms and therefore broken (dangling) covalent bonds exist at the surface. These dangling bonds may result in the formation of defect states with energy levels in the forbidden gap. In order to preserve charge neutrality on the surface, an energy level (ϕ_o) exists, below which the defect states will be filled with electrons and have donor-like behavior. Above ϕ_o, the defect states will be empty and have acceptor-like behavior (Fig. 2.3). Since E_f at the surface of the semiconductor must be aligned with E_f in the bulk, bending of the conduction and valence bands will occur, causing the Fermi level at the surface to shift towards mid gap. When a metal layer is deposited on the semiconductor, charge exchange occurs primarily between the metal and surface states, if the density of surface states is large. Therefore, the charge distribution in the semiconductor is relatively unaffected by the metal overlayer and the Schottky barrier height is no longer dependant upon the metal's work function. As a result, E_f at the semiconductor surface is referred to as pinned.

The second method of forming ohmic conducts established by Sze is based on formation of a highly doped semiconductor surface region (10^{18} carriers/cm^3 or greater). As a result of these high doping levels, any interfacial barrier becomes very narrow and the probability of tunneling becomes high. Since the tunneling current is independent of the polarity of the voltage, ohmic behavior results (Fig 2.4). This second approach allows the formation of ohmic contacts even when defects states dominate the surface properties of the semiconductor. Of the two contact techniques, tunneling contacts are used with greater frequency since the majority of semiconductor devices are fabricated from Si or GaAs which can both experience Fermi level pinning.

Commonly, electrical contacts require a post deposition heat treatment to achieve ohmic behavior. Heat treating commonly results in alloying between the contact metal and the semiconductor [Hal50]. Therefore metals are often chosen which dope the semiconductor to create a highly doped region and lead to ohmic behavior through tunneling. Examples of such systems [Sze81, P. 85] are aluminum(Al) on p-Si heat treated to ~580 °C, and a gold-antimony (Au-Sb) alloy on n-Si heat treated to 400 °C. In other cases, heat treatment results in interfacial compounds, such as metal/silicide/silicon contacts. In these contacts, the metal/semiconductor interface is eliminated and replaced by two new interfaces, a metal/compound and a compound/semiconductor interface. In the case of silicide/silicon interfaces, the interface grows into the bulk silicon (Si), and eliminates or neutralize the surface defects. The resulting ϕ_B is no longer dependant on the surface properties of the silicon or the metal's work function. Instead it depends upon the difference in electron affinity and work function between the metal/silicide and silicide/silicon. As a result, contacts can be reproducibly formed with a predictable ϕ_B. Due to the high conductivity of silicides (often metallic in nature), metal/silicide ohmic contacts are easily formed.

Commonly, a figure-of-merit given for ohmic contact performance is the current density (A/cm^2) at a specific voltage. While this value allows comparisons, both the contact resistance and the bulk resistance of the semiconductor limit the current flow. A more accurate figure for comparison of contacts is the specific contact resistance (R_c) defined as follows:

$$R_c = 1/[\partial J/\partial V]_{v=0} \qquad (2\text{-}10)$$

where J is the current density and V is the applied voltage. For devices with large contact areas such as LEDs and LDs, an R_c between 10^{-2} to 10^{-5} Ωcm^2 is considered acceptable [Wil85].

Metallic Contacts to p-ZnSe

Ohmic contacts to n-ZnSe based on indium (In) metallizations [Ave61, Par77, Wan92] and titanium/platinum/gold (Ti/Pt/Au) [Miy92] are well known. However, the criteria stated above for ϕ_m and χ_s+E_g have been difficult to achieve for p-ZnSe due to the large values of χ_s (4.09 eV) and E_g (2.67 eV). The bonding in ZnSe is mixed covalent and ionic, with neither predominating. Therefore, the fraction of covalent bonding cannot be used to predict whether Fermi level pinning will occur or if ohmic contacts based on thermionic emission currents can be obtained. However, experimental data indicate that Fermi level pinning does not occur with ZnSe. Ultraviolet-photo emission measurements from thin (< 4 Å) Au films on intrinsically n-type MBE grown ZnSe(100) indicate that an interfacial dipole forms between the Au and ZnSe [Xu88]. For thicker coverages, the Schottky barrier height was measured to be 1.45 eV. After correcting for the interfacial dipole, this was in reasonable agreement with the values predicted for an unpinned Fermi level.

These results were confirmed, by other photoelectron spectroscopy measurements, for Au and Al films deposited on MBE grown ZnSe(100) [Vos88, Che94]. In work by Vos et al. on intrinsically n-type ZnSe, the Schottky barrier height was found to be higher for Au (1.45 eV) as compared to Al (0.50 eV). This result is expected for a semiconductor with an unpinned Fermi level since Al has a lower work function (4.36 eV) than Au (5.2 eV). Chen et al. measured the Schottky barrier heights for Au and Al on n-type (Cl doped, 2×10^{18} cm^{-3}) and p-type (N doped, 5×10^{17} cm^{-3}) MBE grown (100)ZnSe. For Au on n and p-type ZnSe, ϕ_B was found to be 1.55 eV and 1.15 eV, respectively. For Al, ϕ_B was 0.55 eV on n-type and 2.15 eV on p-type ZnSe. As seen previously for Au on n-ZnSe, these Schottky barrier heights are in good agreement with predicted values using the Schottky model, indicating that Fermi level pinning does not occur. From these results, the first method of forming ohmic contacts outlined by Sze (selection of $\phi_m \leq \chi_s$) should work for n-ZnSe. In the case of Ti/Pt/Au, the low ohmic contact resistance was attributed to matching of the metal and ZnSe work functions.

Despite the lack of Fermi level pinning, ohmic contacts dominated by thermionic emission currents on p-ZnSe are not easily realized because $E_g + \chi_B \approx 6.76$ eV, which is significantly greater than the work function of metals such as Au (5.2 eV). This fact not withstanding, many introductory devices based on N doped p-ZnSe(100) were constructed using evaporated Au as the contact metal [Qui93, Fan92, Haa91]. In agreement with the photoelectron spectroscopy data, all the Au contacts were found to be rectifying, resulting in LEDs and LDs with high threshold voltages.

In an effort to improve contacts, Ohkawa et al. [Ohk91] used Pt as a contact material, which has a higher work function (5.32 eV) [Whi36] than Au. The contacts were formed by plasma etching 1000 Å of ZnSe (N doped (100) with a carrier concentration of 4.4×10^{15} cm^{-3}) from the sample surface using a 20 W radio frequency (RF) argon (Ar) plasma at 200 mTorr. Next, ~3000 Å of Pt was deposited on the etched region by RF sputtering using Ar ions, 300 W input power, and a pressure of 20 mTorr. For comparison, evaporated Au contacts were also deposited on unetched p-ZnSe. Although the Pt contacts were found to have current densities which were 10 times that of the Au contacts, they were still found to be rectifying.

In another attempt to reduce the ϕ_B of metal/ZnSe contacts, Chen et al. [Che94] deposited several monolayers of Se at the interface between N doped p-ZnSe ((100), 5×10^{17} cm^{-3}) and evaporated Au. In this work, ZnSe was capped by a thick Se layer prior to removal form the MBE growth chamber. Upon transferring the samples to an surface analytical system (capable of low energy electron diffraction, ultraviolet, x-ray, and soft x-ray photo emission spectroscopy), the Se cap was desorbed at temperatures of 280 to 540 °C. For heat treatment at T< 310 °C, several monolayers of Se were found to remain on the ZnSe (100) surface which resulted in a 400 meV decrease in the semiconductor's work function. Upon heating to 340 °C, the remaining Se was desorbed and the work function was found to increase. The reduction in work function was attributed to the high electronegativity of Se. This lead Chen and co-workers to intentionally deposit several monolayers of Se on p-ZnSe (100), prior to depositing thin Au layers. Photoelectron spectroscopy measurements through the thin Au layers showed that the Schottky barrier height was reduced from 1.15 eV to 0.89 eV, due to the interfacial Se. This 0.25 eV difference in ϕ_B was found to disappear following heat treatments at 300 °C. At this temperature the Se was lost due to vaporization and the contact structure approximated the Au/p-ZnSe contacts without interfacial Se.

Attempts to apply Sze's second ohmic contact approach (i.e. highly doped surface layers) have also failed due to the inability to produce highly doped ($>5\times10^{18}$ cm^{-3}) ZnSe. Prior to the development of N doping, the highest carrier concentrations for p-ZnSe were achieved using lithium (Li) with 8×10^{16} cm^{-3} as the maximum free hole concentration [Haa90]. Higher Li concentrations were reported to be compensated, leaving the ZnSe highly resistive. Oxygen (O) was also reported to be a p-type dopant for ZnSe, resulting in a maximum 1.2×10^{16} cm^{-3} free hole concentration [Aki89a]. Nitrogen radical doping [Par90] has yielded maximum free hole concentrations of $\sim1\times10^{18}$ cm^{-3}, but increasing compensation prevented higher free hole concentrations from being achieved at higher nitrogen densities [Woo90]. Mandel [Man63] used energy balance equations to show that in II-VI semiconductors, CdTe and ZnTe, self compensation occurs when the energy of defect formation is small compared to the energy gained by compensation. This situation occurs in more ionic semiconductors which have band gaps that are large in comparison to the cohesive energy of the crystal. When the energy gained by a crystal following the non-radiative recombination of a free carrier at a defect is equivalent to the energy required to create the defect (the lattice cohesive energy), then compensating defects have a high probability of being generated. This postulate provides a potential theoretical explanation for the difficulties associated with generating a highly doped p-ZnSe region.

As expected from the discussion above, attempts to improve contact performance by increasing the carrier concentration in the near-surface region have met with limited success. Qui et al. [Qui93] demonstrated that the incorporation of active N dopant in p-ZnSe could be increased using a low temperature (150 °C) MBE growth. Qui reported the highest carrier concentration for p-ZnSe of ~2×10^{18} cm^{-3}, but analysis by transmission electron microscopy (TEM) indicated this material had a high density of dislocations (10^{9} cm^{-2}). The I-V characteristics were measured for Au contacts deposited on ZnSe with doping concentrations of 1×10^{18} cm^{-3} and growth temperatures of 150 °C and 230 °C. While extensive characterization of the contacts was not performed, the data indicate that the reverse bias breakdown voltage for the contacts decreased from ~4 volts to < 2 volts when the growth temperature was decreased from 230 °C to 150 °C. Based on this study, the reduction in reverse bias breakdown voltage was postulated to be due, in part, to defect-assisted tunneling where the defect state was at ~0.5 eV above the valence band maximum.

Ohmic Au contacts on p-ZnSe (dominated by tunneling currents) have been reported for p-ZnSe doped with oxygen (O) [Aki91]. Although maximum free hole concentrations in O doped epitaxial films have been limited to the 10^{16} range for MBE grown ZnSe, in this work, a highly doped p-ZnSe surface region was created by exposing the O-doped p-ZnSe to an oxygen plasma. This surface modification is reported to result in ohmic contacts dominated by tunneling currents. However, oxygen doping of ZnSe has proven to be unreliable and difficult to reproduce [Hel93]. In addition, these contacts have low current densities and exhibited large hysteresis loops under AC bias. As a result, these contacts do not appear to be useful for device applications.

Based on the review of metal contacts to ZnSe, it is unlikely that metal contacts will be identified with work functions high enough to result in ohmic contacts dominated by thermionic emission. Similarly, the literature reviewed also indicates the many obstacles associated with obtaining ohmic contacts (dominated by tunneling) by generating a highly doped p-ZnSe surface region. However, attempts to produce metal/ZnSe ohmic contacts have focused on selecting contact materials based on their work functions, or surface modifications prior to deposition. Researchers have not explored the effects of heat treatments on metal/p-ZnSe contacts. Since heat treatments are a fundamental step in many ohmic contacts process, work in this dissertation was aimed at identifying heat treatments that will induce interfacial modifications leading to improved metal/p-ZnSe contacts.

Based on the literature review, increasing the ZnSe near-surface carrier concentration is difficult due to self compensation. Thus it is difficult to reduce the interfacial barrier width to increase the probability of tunneling. However, Sze indicated that tunneling can occur through defect states in the forbidden gap as shown for a p-n junction in figure 2.5 [Sze81, p. 528]. This mechanism was reported by Qui et al. [Qui93] to reduce the reverse bias breakdown voltage for Au/p-ZnSe Schottky contacts. Photoluminescence measurements by Dean [Dea82] indicated that Au and Ag form deep acceptor levels in ZnSe with ionization energies of 550 meV and 430 meV, respectively. These ionization energies are >> 3kT so an insignificant fraction of either should be ionized at room temperature. Therefore, neither would contribute to p-type doping. However, the defect states have energies similar to those reported by Qui et al. and may participate in defect assisted tunneling.

Heat treatments of Ag contacts are interesting for another reason. Oxygen has a high permeability (10^{-11} to 10^{-14} $cm^{-1}s^{-1}$ at 400°C to 800°C respectively) through Ag. This permeability can be increased even more by using a glow discharge to dissociate upstream O_2 to produce O [Out92]. As discussed above, O is a p-type dopant in ZnSe, forming a shallow acceptor level with ionization energies of ~80 meV [Aki89b]. Although compensation is still a concern, heat treatments of Ag/ZnSe contacts in an oxygen ambient has the potential to generate a highly O doped surface region by co-doping with N and O. The results and discussion of heat treated Au and Ag contacts on p-ZnSe are presented in chapter 3.

HgSe Contacts to p-ZnSe

The inability to form ohmic contacts to p-ZnSe using the methods outlined by Sze has resulted in a need to apply more elaborate contact techniques to p-ZnSe. The first of these techniques is based on reducing ϕ_B, by using HgSe as a contact material. HgSe is a highly electronegative semimetal with a negative band gap of -0.15eV [Wil81, Ekp90], a zinc blende structure and a lattice parameter of 6.08**Å** [Han58]. Research on mercury chalcogenide contacts to ZnSe by Best et al. [Bes76] and Scranton et al. [Scr77] predate the ability to reproducibly dope ZnSe p-type. As a result, these studies were performed on ZnSe heated in liquid Zn to produce n-type carrier concentrations of 5×10^{17} cm^{-3}. In both of these studies, HgSe was deposited by evaporating Se from a boron nitride crucible which was then passed through a hot quartz tube (to crack the resulting Se ring structures) producing Se_2. A droplet of liquid Hg was placed in the evaporation chamber which produced Hg vapor. The Hg and Se_2 reacted at room temperature and formed HgSe on the substrate surface. Capacitance-voltage and photoresponce measurements from these samples indicated that HgSe formed Schottky barriers which were ~0.5 eV larger than those formed by

Au. As a result of the high ϕ_B on n-type semiconductors, Scranton et al. proposed that one possible application for the HgSe contacts was low ϕ_B contacts to p-type semiconductors (which they speculated could lead to ohmic contacts).

Additional studies of mercury chalcogenides on common anion II-VI compound semiconductors were performed by Hsu and Faurie [Hsu88]. In this work, core level X-ray photoelectron spectroscopy (XPS) measurements were used to determine ϕ_B for HgTe contacts on CdTe and ZnTe. This work showed that ϕ_B for the HgTe/semiconductor contacts was ~20% of the semiconductors band gap (E_g). Based on this and other work, Lansari et al. [Lan92] proposed an empirical "common-anion" rule for mercury chalcogenides which describes the behavior of several systems. For HgSe on p-ZnSe, this rule indicates that ϕ_B for hole transport will be ~0.2 E_g, where E_g is the band gap of the common-anion semiconductor. Since HgSe is a semimetal with a negative band gap, the corresponding conduction band offset (ΔE_c) is ~0.8 E_g . Based on this rule, ϕ_B for HgSe on p-ZnSe is ~0.6 eV, as shown in figure 2.6. Proceeding under this assumption, Lansari et al. grew HgSe by MBE [Lan93] for contacts on p-ZnSe [Lan92]. The optimal MBE growth temperature for HgSe was ~100 °C, yielding material with n-type carrier concentrations of 10^{18} cm^{-3} and mobilities of $1x10^{-14}$ cm^2/V-S at 300 °K.

The growth of HgSe/ZnSe contacts required the use of two MBE systems to prevent Hg from contaminating ZnSe during growth. The first chamber was used to grow N doped p-ZnSe(100) (or n-on-p diode structures with a top p-ZnSe layer) with carrier concentrations of 5x10^{17} cm^{-3}. Next, the samples were moved to the second MBE chamber, through a vacuum transfer system, where the HgSe was grown. As a final step, gold (Au) or indium (In) was deposited to form ohmic contacts to the HgSe.

HgSe contacts, shown schematically in figure 2.6, were found to have pseudo-ohmic behavior for $\geq$ 5x10^{17} cm^{-3} p-ZnSe at 300 °K [Lan92]. They were rectifying for lower carrier concentrations. For 300 μm X 300 μm square contacts, current densities of ~0.333 A/cm^2 were observed at 1 volt. The HgSe contacts have been further improved by growth of a thin (~100 Å) $ZnTe_{0.2}Se_{0.8}$ layer between the HgSe and p-ZnSe [Ren94]. The $ZnTe_{0.2}Se_{0.8}$ layer was heavily doped by nitrogen, which was reported to result in the formation of deep levels. These deep levels were indicated to promote resonant tunneling which leads to enhanced current flow (Fig. 2.7). The R_c or current densities for these type of contact structures alone have not been reported. However, forward biased ZnSe diodes with these contacts were reported to have current densities of 200 A/cm^2 at 4 volts.

While HgSe contacts have shown significant promise, the growth procedure for these contacts requires significant capital investment which complicated device fabrication. In addition, the empirical common anion rule has never been confirmed by measuring the ϕ_B of HgSe on p-ZnSe. To improve the utility of HgSe contact, research presented in chapter four of this dissertation focused on developing a simpler *ex situ* process for forming HgSe contacts. Se has been reported to act as a passivating layer which protects the surface of ZnSe upon exposure to atmosphere, and can subsequently be removed by heating the sample to 115-150 °C in ultra-high vacuum. This yielded a clean single crystal, stoichiometric and well ordered surface [Jon88]. In fact, Se capping was used in some recent HgSe contact experiments to protect the ZnSe surface while transferring the sample between the ZnSe and HgSe MBE growth chambers [Ren94]. An *ex situ* process was developed in this dissertation to form HgSe on capped ZnSe. This capping protects the ZnSe samples so that atmospheric processing can be used without risk of contamination. Once the capped samples were removed from vacuum, it was reacted with Hg vapor to form HgSe. The structural and interfacial properties of *ex situ* HgSe contacts to p-ZnSe were characterized along with their electrical properties, including $\phi_{B.}$ The results and discussion of HgSe contacts formed by the *ex situ* process are given in chapter four.

ZnTe/ZnSe Contacts to p-ZnSe

Recently, a very promising ohmic contact process to p-ZnSe was derived from contact work to GaAs, originally developed by Woodall et al. [Woo81]. As indicated above, ohmic contact formation to GaAs is complicated by Fermi level pinning. To circumvent this problem, a graded junction ($Ga_xIn_{1-x}As$) was formed between the device semiconductor (GaAs) and a narrower gap semiconductor (InAs). By grading the composition between the two semiconductors, a gradual change in the band structure occurred which did not present a significant impediment to charge carriers (Fig. 2.8). A final layer of silver (Ag) was deposited on the structure to form an ohmic contacts to the InAs. The contact resistances (R_c) were estimated to be between 5×10^{-7} Ωcm^2 and 5×10^{-6} Ωcm^2, indicating that this was a viable method of producing low resistance ohmic contacts.

Following this approach, Fan et al. demonstrated pseudograded ohmic contacts to p-ZnSe using zinc telluride (ZnTe) [Fan92, Fan93]. ZnTe was selected as a suitable material for forming graded contacts to ZnSe because it had the same zinc blende crystal structure, it could be doped p-type with free hole concentration > 10^{19} cm^{-3} using the same nitrogen radical doping technique described above for p-ZnSe, and Au/p-ZnTe ohmic contacts are easily formed [Oza93]. However, attempts to grow optical devices using $ZnTe_xSe_{1-x}$ graded alloys have proven to be difficult due to competition between Te and Se on the growth surface [Kol88]. In this work, this problem was avoided by growing ultrathin layers of ZnTe and ZnSe with appropriate dimensions so that the composition approximated that of a graded compound. This approach was also used in the design of the multilayer pseudograded contact structures to p-ZnSe (Fig. 2.9). These structures were made up of 17 cells which were 20 **Å** thick, with each cell consisting of a ZnTe and ZnSe layer. The thickness of the ZnSe and ZnTe layers in the first cell were 18 Å and 2 Å, respectively. In each consecutive cell, the ZnSe layer was reduced by 1 Å, while the ZnTe was increased by the same amount, yielding thicknesses of 2 Å and 18 Å for the ZnSe and ZnTe layers in the final cell. These contacts were deposited on p-ZnSe with carrier concentrations of $3x10^{17}$ cm^{-3} and were reported to have linear I-V characteristics with an R_c of $2x10^{-3}$ Ωcm^2 to $8x10^{-3}$ Ωcm^2.

A second ZnSe/ZnTe based contact scheme has been developed which is based on obtaining resonant tunneling through the formation of a multiquantum well structure [Hie93]. Resonant tunneling occurs in quantum well structures when electrons approaching the well have energies equivalent to the quantum energy states created by the well. These electron tunnel through the quantum well at the energy level of the quantum state. Therefore, the multiquantum well contacts have a series of p-ZnTe quantum wells with widths of 0.3, 0.4, 0.5, 0.6, 0.8, 1.1, and 1.7 nm between 2 nm p-ZnSe layers, followed by a p-ZnTe overlayer (Fig. 2.10a). The resulting quantum wells were calculated to all have energy levels which corresponded to the valence band maximum (E_V) in the bulk ZnSe [Hie93], as shown in figure 2.10b. As a result, resonant tunneling occurred allowing charge carriers to tunnel from the ZnSe, through the barrier, to the ZnTe. The multiquantum well contacts were found to have linear I-V characteristics with an R_c of $5x10^{-2}$ Ωcm^2 on nitrogen doped p-ZnSe with carrier concentrations of $7x10^{16}$ cm^{-3}. The ability to produce ohmic contacts on p-ZnSe with such low carrier concentrations have made this approach the most promising scheme developed to date.

Since both pseudograded and multiquantum well contacts require ohmic contacts to ZnTe overlayers, researchers have recently been investigating methods of improving these contacts. Ozawa [Oza93] has shown that the R_c of Au ohmic contacts to ZnTe can be reduced from 2×10^{-4} to 5×10^{-6} Ω cm^2 by depositing a thin ~100 Å layer of palladium (Pd) at the Au/ZnTe interface. The minimum R_c was obtained following heat treatment at 200 °C for 2 minutes. The reduced R_c of the Au/Pd contacts to ZnTe has led to their use in current ZnTe/ZnSe superlattice contacts to p-ZnSe.

Despite the successful incorporation of multiquantum well contacts into ZnSe based devices, degradation of quantum well contacts have been linked to degradation of the laser structures. As discussed in chapter 1, single CdZnSe strained quantum well lasers with ZnMgSSe/ZnSeS confinement layers have resulted in the highest output power (~0.5 watts), highest operating temperature (394 K), and lowest threshold currents (2.5 mA). Guha et al. [Guh94] showed that degradation of these devices occurred through the "emission" of dark line defects (DLDs) along the <100> direction which grow into patches of dislocation along the <011> direction. These dark line defects act as non-radiative recombination centers and quench the light output of the laser. Hua et al. [Hua94] have further studied the degradation of these laser structures under pulsed operation and report that dark line defects originated as V-shaped stacking faults which nucleated at the ZnSSe/GaAs interface (Fig 2.11). The intersection point of the V-shaped stacking faults and the quantum well region were the point at which patches of dislocation networks originate. The dislocation network spread away from this point, through the quantum well region. Note that the V-shaped stacking faults were postulated to originate from defects formed during growth of the structure. Similar defect generation was reported by Hovinen et al. [Hov95] in identical laser structures pumped by a dye laser with an optical fluence of 100 µJ/cm^2.

Currently, the optimal ZnSe based laser designs used Au/Pd metallizations to multiquantum well contacts to p-ZnSe, grown on the same single quantum well laser structures described above. The threshold current for room temperature cw operation of these ZnSe based laser diodes is >200 A/cm^2. During operation the multiquantum well contacts have been found to fail after several minutes at current densities > 100 A/cm^2. In addition, optical inspection of the device during operation shows the evolution of DLDs at the point where the electrical probe contacts the multiquantum well contact (personal communications with P. Baude at 3M company, 3M Center, St. Paul, Minnesota).

In order to identify the failure mechanism of the contacts and correlations between contact failure and DLD formation, the degradation of multiquantum well contacts under high current loading have been studied as reported in chapter 5. Contact failure was characterized as a function of current density and temperature. Structural and compositional changes, resulting from degradation, and their relation to DLD formation were identified.

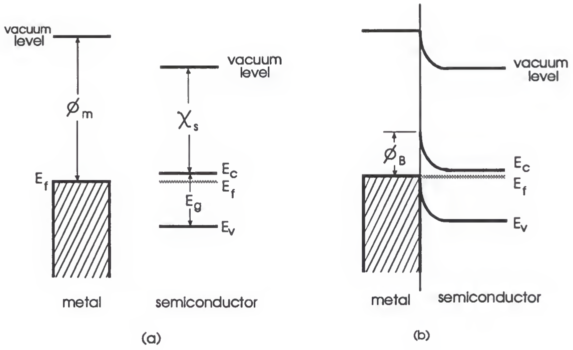

Figure 2.1: Energy band diagram for a metal and semiconductor a) prior to making an intimate contact and, b) showing bending of the conduction and valence band edges after making intimate contact.

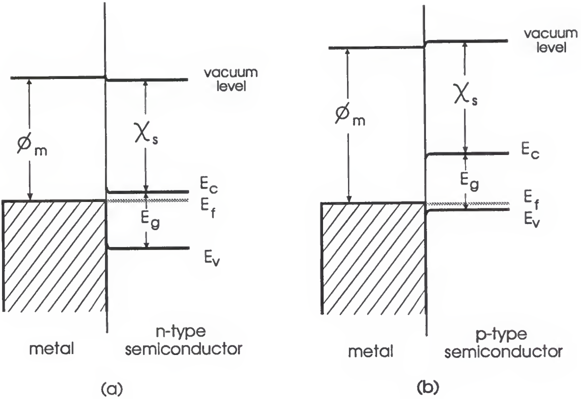

Figure 2.2: a) Energy band diagram for Schottky contact on a n-type semiconductor with the metal's work function nearly equal to the semiconductor's electron affinity. b) Energy band diagram for Schottky contact on a p-type semiconductor with the metal's work function nearly equal to the semiconductor's band gap and electron affinity.

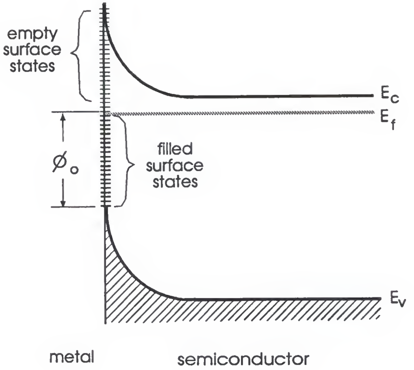

Figure 2.3: Energy band diagram showing midgap surface states, generated by dangling covalent bonds, resulting in the Fermi level pinning at mid gap.

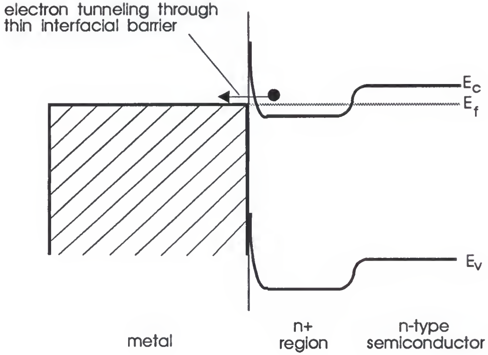

Figure 2.4: Energy band diagram for ohmic contacts with a heavily doped (n+) region between the metal and semiconductor. The thin interfacial barrier leads to tunneling currents dominating conduction.

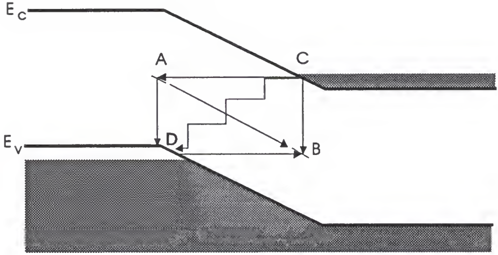

Figure 2.5: Band diagram illustrating the mechanism of tunneling via states in the forbidden gap for excess current flow. Path CBD is the basic mechanism, CAD and CABD are alternative paths, and the stepped CD path illustrate tunneling between local levels.

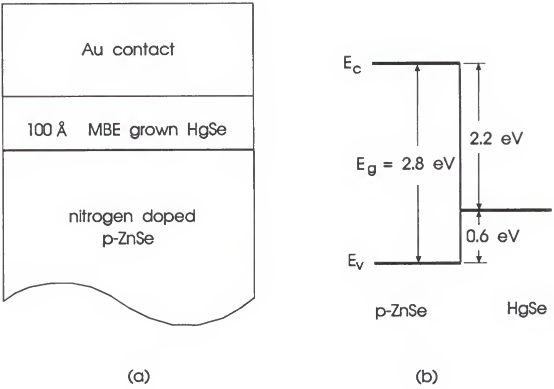

Figure 2.6: a) Schematic diagram of HgSe contact structure, and b) the energy band diagram for HgSe on p-ZnSe showing the valence band offset to be equal to 20 % of the band gap.

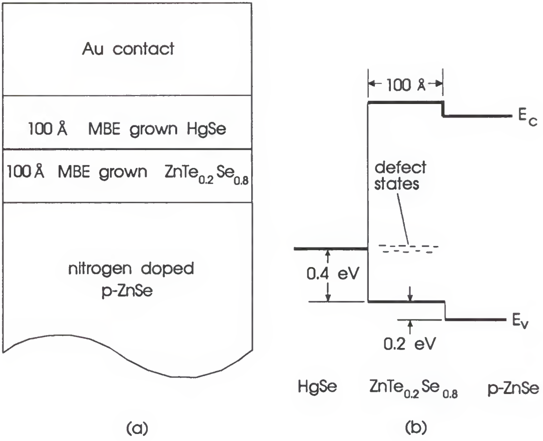

Figure 2.7: a) Schematic diagram of HgSe contact structure with $ZnTe_{0.2}Se_{0.8}$ layer, and b) the energy band diagram for the modified HgSe contacts showing the proposed defect states which lead to resonant tunneling.

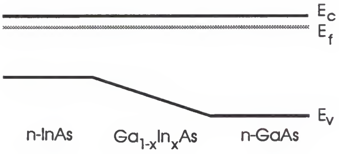

Figure 2.8: Energy band diagram for a graded n-GaAs\n-InAs contact indicating that the graded structure has no conduction band offset to impede the flow of charge carriers.

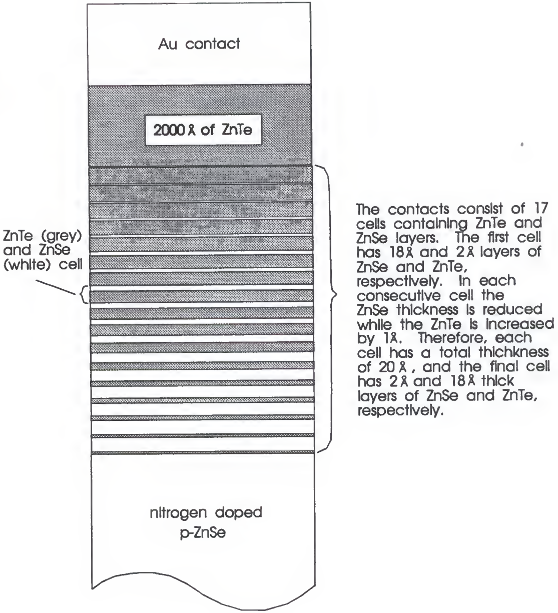

The contacts consist of 17 cells containing ZnTe and ZnSe layers. The first cell has 18Å and 2Å layers of ZnSe and ZnTe, respectively. In each consecutive cell the ZnSe thickness is reduced while the ZnTe is increased by 1Å. Therefore, each cell has a total thichkness of 20 Å, and the final cell has 2Å and 18Å thick layers of ZnSe and ZnTe, respectively.

Figure 2.9: Schematic diagram showing the structure of ZnTe/ZnSe pseudograded contacts which are composed of cells containing ZnTe and ZnSe layers.

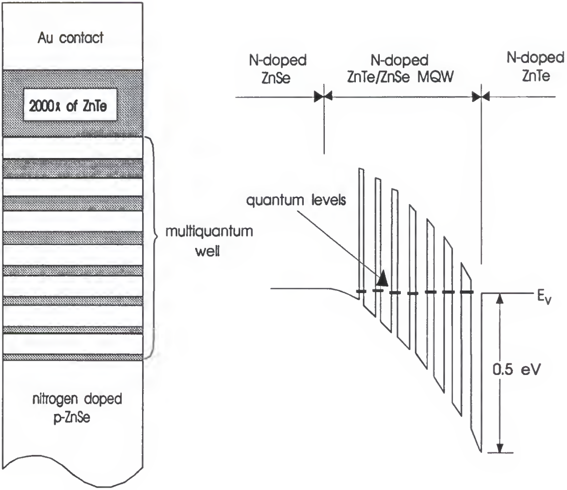

(a) (b)

Figure 2.10: a) Schematic diagram showing the structure of ZnTe/ZnSe multiquantum well contacts which are composed of ZnTe (grey) wells 0.3, 0.4, 0.5, 0.6, 0.8, 1.1, and 1.7 nm thick between 2 nm ZnSe (white) layers. B) The energy band diagram for multiquantum well contacts.

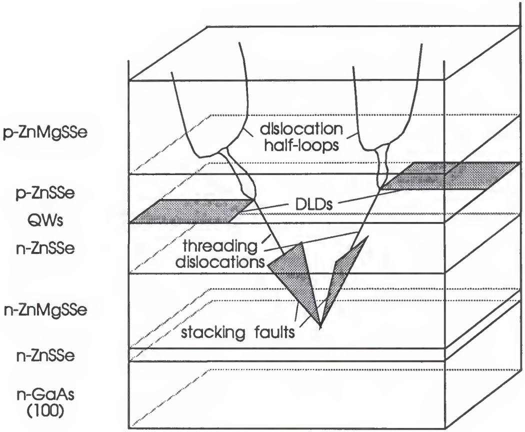

Figure 2.11: Schematic of degraded ZnSe based diode laser structure showing stacking faults and dislocations which lead to dark line defects (DLDs) forming in the quantum well (QW) region of the laser.

CHAPTER 3

Au AND Ag CONTACTS

Introduction

The following chapter describes the effects of heat treatments on Au and Ag contacts to p-ZnSe. In this work, heat treatments were identified which lead to a reduction in the reverse bias breakdown voltage for these rectifying contacts. Analytical characterization including secondary ion mass spectrometry and Auger depth profiling were used to identify structural and compositional changes induced in the contacts by heat treatment. These analytical results were correlated to changes in the dominant conduction mechanisms across the metal/semiconductor interfaces that lead to the reductions in reverse bias breakdown voltage.

Experimental Setup

Studies of Au and Ag contacts were performed using nitrogen radical doped ZnSe grown by MBE on semi-insulating GaAs substrates. Growth conditions for the ZnSe were chosen to produce free hole concentrations in the low to mid 10^{17} cm^{-3} range [par90]. No surface preparation was used on the

MBE grown surface. Instead, the metal contacts were deposited on the ZnSe which was kept clean by careful storage in desiccated chambers. Au contacts were deposited by sputtering, while Ag contacts were deposited by sputtering and evaporation. The sputtering was performed in a custom built sputter deposition system designed at the University of Florida [Tru92]. The system contained two radio frequency (RF) and two direct current (DC) 2" diameter planar magnetron sputter guns manufactured by US Inc. The system also contained a centrally located sample rotation stage which allowed samples to be sequentially rotated in front of the four sputter guns. The vacuum chamber for the system was a quartz bell jar with a Viton seal, seated on a stainless steel base plate. The system was pumped by a diffusion pump (Varian VHS-6) which was backed by a Sargent-Welch mechanical pump, model number 1397. The ultimate pressure reached by the system was ~$2x10^{-7}$ Torr.

Prior to sputter deposition, samples were loaded in the deposition chamber which was pumped down to a base pressure of $2x10^{-6}$ Torr. The Au and Ag contacts were deposited using the DC sputter guns with DC potentials of 375-400 V in argon at a pressure of 27 mTorr. Although a single sputter gun was used during either the Au or Ag depositions, the rotation stage was used to improve the uniformity of the film thickness and to reduce sample heating during deposition. These deposition parameters and sample rotation resulted in a deposition rate of 125 to 150 A/min. for both Au and Ag. The depositions were 8 to 10 minutes long yielding metal layers with a thickness of 1000 to 1500 **Å**.

The Au and Ag were patterned into 1 mm dot contacts onto rectangular ZnSe substrates with dimensions of ~4 mm x 6 mm, with ~ 6 contacts per sample. The patterning was accomplished by placing a stainless steal mask with 1 mm holes in contact with the ZnSe surface, between the ZnSe and the sputter gun.

Following deposition, the sputtered samples were heat treated in a quartz tube furnace in a reducing atmosphere of forming gas (10% hydrogen, 90 % nitrogen). Separate Au/ZnSe samples were individually heat treated at temperatures of 150, 200, 300, 350, and 400 °C, and separate Ag/ZnSe samples were heat treated at temperatures of 150, 200, and 300 °C. At each temperature the samples were heated in consecutive intervals yielding total heat treatment times of 15, 30, 45, 60, and 90 minutes.

Ag contacts were also deposited using evaporation. These contacts were deposited in a Veeco evaporator from an alumina (Al_2O_3) crucible heated by a tungsten wire. The vacuum chamber for this system was also a quartz bell jar on a stainless steel base plate, similar to the sputter system. This system was pumped by a Veeco EP 41W diffusion pump backed by a Sargent-Welch 1937 mechanical pump and has an ultimate pressure of 1×10^{-7} Torr. Unlike the sputter system, this system is not equipped with sample rotation.

Prior to evaporation, samples were loaded and the system was pumped to a base pressure of 2×10^{-6} Torr. The thickness and deposition rate of the metal layers were monitored during deposition using an Inficon quartz crystal oscillator. Power was supplied to the tungsten filament to maintain a deposition rate of 5 to 10 Å/s, and deposition was terminated at a thickness of 1000 Å. As with the sputtered contacts, patterning was performed using a stainless steel mask yielding an average of 6 contacts (1 mm diameter) on ~4 x 6 mm ZnSe substrates. During deposition, the pressure in the system was observed to rise, but remained at $<5\times10^{-5}$ Torr.

The evaporated Ag contacts on ZnSe were sequentially heat treated at consecutively higher temperatures, as opposed to using separate samples at each temperature. These contacts were heat treated at 150, 200, 250, and 300 °C in the same tube furnace used for the sputtered contacts. Starting at 150 °C, the samples were heat treated in 15 minute intervals to total times of 15, 30, 45, 60, 75, and 90 minutes. After 90 minutes, the temperature was increased and the sample was heat treated over the same 15 minute intervals. This was repeated until the samples had been heat treated for a total of 90 minutes at each temperature. Unlike the sputtered samples, which were heat treated in only forming gas, the evaporated contacts were heat treated in both forming gas and oxygen (O). The oxygen atmosphere was used to identify if heat treating would result in oxygen diffusing through the Ag to co-dope the ZnSe, while samples heated in forming gas were used for controls.

Prior to heat treatment, and following each heat treatment interval, the current vs. voltage (I-V) characteristics of the contacts were measured for sputtered and evaporated Au/ZnSe and Ag/ZnSe contacts. The I-V data was obtained by measuring the current flow between two of the dot contacts under an applied bias. The resulting data, collected over a range of applied biases, represent the reverse bias break down voltage for one of the two back-to-back Schottky diode barriers formed by the metal-semiconductor contacts. The I-V characteristics were measured using an Tektronix 177 curve tracer, and by an automated system which consists of an IBM PC with IEEE-488 communications, a Hewlett-Packard 6112A DC power supply, and a Keithely 485 picoammeter. The reverse bias breakdown voltage was determined by extrapolating the linear portion of the I-V curve back to the voltage axis. The voltage at which the extrapolated line crossed the axis was recorded as the breakdown potential. The I-V data was also used to determine a normalized resistance by calculating the slope of the linear portion of the I-V curve, taking it's reciprocal, and multiplying this value by the area of the dot contacts. These measurements of normalized resistance include both the bulk semiconductor resistance and contact resistance (similar to the reporting of current density at a specific voltage as described in chapter 2). Therefore, the normalized resistance values are only qualitative values to be used for comparing the Au and Ag contacts between themselves. The barrier height and normalized resistance measurements for Au/ZnSe contacts were calculated using I-V data recorded with a vertical axis scale of 25 μA/cm and a horizontal axis scale of 6.25 volts/cm, while the Ag/ZnSe contacts had a vertical axis scale of 25μA/cm and a horizontal axis scale of 2.5 volts/cm.

Following heat treatment and electrical characterization, the sputter deposited Au and Ag contacts which exhibited the lowest reverse bias breakdown voltage were characterized by scanning Auger depth profiling using a Perkin-Elmer PHI 660 Auger spectrometer and by secondary ion mass spectrometry (SIMS) using a Perkin -Elmer PHI 6600. The Auger depth profile was performed using a 10 keV, 30 nA electron beam. The SIMS analysis was performed using a 5 KeV, 30 nA Cs^+ beam with a 100 μm x 100 μm raster size and 65% linear gating. The data for all elements except zinc (Zn) were obtained with the SIMS' quadrupole mass spectrometer set to analyze positive ions. Obtaining the Zn profiles required the quadrapole to be recalibrated for negative ions, therefore, the Zn profiles were collected separately from data for other elements. The SIMS data collected from both positive and negative ions were overlaid to produce a single composite set of data.

The Au/ZnSe and Ag/ZnSe samples selected for Auger and SIMS analysis were heat treated at 350 °C for 90 minutes and at 150 °C for 90 minutes, respectively. An additional Ag/ZnSe sample was selected for analysis to help identify the cause for resistance increases observed for Ag/ZnSe contacts heat treated at temperatures > 150 °C. This sample was heat treated at 300 °C for 30 minutes. SIMS and Auger data were also obtained from non-heat treated samples for comparison.

Results

Sputtered Au Contacts

Sputter deposited Au contacts will be presented first, followed by the results from the sputter deposited Ag contacts. Finally, the evaporated Ag contacts will be presented. Due to the volume of I-V data collected, only the I-V data from the contacts showing the minimum reverse bias breakdown voltages are shown. The remainder of the I-V data has been summarized in plots of breakdown voltage vs time and normalized resistance vs time. These plots of reverse bias breakdown voltage and normalized resistance data for the sputtered Au contacts are shown in figures 3.1 and 3.2, respectively. Prior to heat treatment, the sputtered Au contacts were found to be rectifying with reverse bias breakdown voltages of 10 to 15 volts. Heat treating these samples at 150 and 200 °C did not produce any appreciable change. A slight reduction in reverse bias breakdown was observed at 300 °C, but the reduction became much more pronounced at higher temperatures. For samples heat treated at 350 °C, the breakdown voltage dropped significantly after the first 15 minutes to a value of ~3.5 volts, reached a minimum value of ~3 volts after 30 to 45 minutes, and then increased to ~4 volts following additional heat treatments of up to 90 minutes. The results for heat treatments at 400 °C were similar to those obtained at 350 °C, with a minimum breakdown voltage of ~3 volts obtained following 15 to 30 minutes of heat treatment time. The normalized resistance of the contacts remained relatively constant over the range of temperatures and times used in this experiment. The I-V data for the sputtered Au contacts heat treated at 350 °C is shown in figure 3.3.

Comparison of the SIMS data from the as deposited and heat treated (350 °C for 90 minutes) sputtered Au contacts indicates that Au diffused into the ZnSe as a result of heat treatment. The SIMS data for the as deposited and heat treated samples are shown in figures 3.4a and 3.4b, respectively. In addition to Au diffusion, these data indicate that Zn and Se out diffused into the Au contact. The native ZnO interfacial oxide was observed in the as deposited sample. However, there was no evidence in these data to indicate the formation of any compound the Au/ZnSe interface as a result of heat treatment.

Auger depth profiling data from the sputtered Au contacts heat treated at 350 °C for 90 minutes and in the as deposited condition are in good agreement with the SIMS data. These data also indicate that Au diffused into the ZnSe, and that Zn and Se out diffused into the Au contacts as a result of heat treatment. The Auger data for the as deposited and heat treated Au contacts are shown in figures 3.5a and 3.5b.

The reverse bias breakdown voltage and normalized resistance data for the sputter deposited Ag contacts are shown in figures 3.6 and 3.7, respectively. The as deposited contacts were found to have a reverse bias breakdown voltage of 3 to 4.5 volts, which was significantly lower than for the sputtered Au contacts (10 to 15 volts). Heat treatment at 150 °C was found to produce the best contact performance with a minimum breakdown voltage of ~2.3 volts occurring after 45 minutes of heat treatment time. The I-V data for these samples are shown in figure 3.8. Samples heat treated at 200 and 300 °C were also found to have breakdown voltages close to ~2.3 volts they exhibited significantly increased normalized resistance as compaired to samples heated to 150 °C. The resistance increase was observed to occur after only 15 minutes of heat treatment time and became more severe for higher temperatures and longer heat treatments.

Sputtered Ag Contact

The SIMS data for the sputtered Ag contacts indicate that there was little change in the depth profiles between the as deposited sample versus those heat treated at 150 °C for 90 minutes. Both profiles indicate an abrupt junction between the Ag and ZnSe with the native ZnO interfacial oxide being obvious at 1 minute of sputter time. The data suggest that neither compound formation or diffusion occurred at the interface as a result of heat treatment. Even for samples heat treated for 30 minutes at 300 °C, the SIMS data still indicate a moderately abrupt junction with slight broadening of the Ag, O, and C profiles. Although this broadening could indicate simultaneous diffusion of all three elements, the similarity in the profiles suggests that the Ag has roughened, perhaps due to grain grown, leading to a broader interface. The SIMS profiles for the as deposited, 150 °C for 90 minutes, and 300 °C for 30 minute samples are shown in figures 3.9a through 3.9c.

The Auger data from the sputter deposited Ag contacts are again in good agreement with the SIMS data (Fig. 3.10a through 3.10c). The as deposited, 150 and 300 °C samples were all found to have abrupt interfaces, and as in the SIMS data, there is a slight broadening of the interface for the 300 °C case. It is also interesting to note that neither the SIMS nor Auger data showed any indication of Zn or Se diffusion through the Ag contact to the ambient surface, in contrast to the behavior of the Au contacts. A variation in Ag film thickness was observed from one sample to the next in the Auger depth profiles (Fig 10). While this was due in part to variations in the amount of Ag deposited, it was also due to the location on the dot contact at which the depth profile was performed. The stainless steel mask resulted in shadowing of the Ag contacts during deposition, leading to the film having a greater thickness at the center of the dot as opposed to the edges. Due to a limited amount of space in which to perform SIMS and Auger depth profiles, all profiles were not performed at the same relative position on the dot contact.

Evaporated Ag Contacts

The reverse bias breakdown voltage and normalized resistance data for the evaporated Ag contacts heat treated in oxygen and forming gas are shown in figures 3.11 and 3.12. In these data, the as deposited samples were found to have breakdown voltages of 3.9 to 4.6 volts which are similar to the sputtered contacts. Heat treatment at 150 °C in oxygen was found to produce a decrease in breakdown voltage, reaching a minimum of 2.3 volts after 75 minutes at temperature. For subsequent heat treatments, the barrier height was found to increase with increasing heat treatment temperatures and times. In contrast, the barrier height of the sample heat treated in forming gas did not decrease during heat treatments at 150 °C, but instead they remained at ~ 4.0 volts. At higher heat treatment temperatures in forming gas, an increase in barrier height was observed. For 150 and 200 °C heat treatments, the normalized resistance was found to be similar for both heat treatment ambients. However, for the samples heat treated in forming gas at 250 °C, a much greater increase in normalized resistance was observed compared to samples heat treated in oxygen. For 300 °C heat treatments, the samples in oxygen exhibited a severe increase in normalized resistance, while the resistance of samples in forming gas was too large to measure barrier height or normalized resistance. The I-V data for the evaporated Ag samples heat treated at 150 °C are shown in figure 3.13.

Discussion

Au Contacts

The analytical results from sputter deposited Au contacts heat treated in forming gas show that Au diffused into the ZnSe (and vice versa) at a temperature of 350 °C, leading to a reduction in reverse bias breakdown voltage. As indicated in chapter two, Au is reported to be a deep acceptor in ZnSe with an ionization potential of 550 meV[Dea82]. Qui et al. [Qui93] have hypothesized that these deep levels could assist tunneling currents across the Au/ZnSe interface. In order to rule out the possibility that thermionic emission was dominating transport in these contacts, the thermionic emission currents for the contacts were modeled using Eq. (2-1) through (2-4). In these calculations, the value of ϕ_B for Au on ZnSe was taken to be 1.15 eV [Che94], a temperature of 300 °K was used, an area of 0.008 cm^2 (1 mm diameter), an N_d of 3×10^{17} cm^{-3}, a hole effective mass of 0.60 and a low frequency dielectric constant of 9.20 [Rud86]. The junction's built in potential (V_i) was calculated by determining the position of the Fermi level as described by Sze [Sze85, p. 25] and subtracting this value from ϕ_B. In addition to image force reduction, these calculations were corrected for the effects of barrier height reduction due to thin interfacial oxides $\Delta\phi_{B(oxide)}$ as follows [Sha84, p. 16],

$$\Delta\phi_{B(oxide)} = -\alpha\ |\mathscr{E}_m| \qquad (3\text{-}1)$$

where $\mathscr{E}_m$ is the electric field intensity immediately inside the semiconductor and α is given by the following,

$$\alpha = \delta\epsilon_s/(\epsilon_i + q^2\delta D_s). \qquad (3\text{-}2)$$

Here, δ is the width of the interfacial oxide, ϵ_i is the dielectric constant of the oxide, and D_s is the density of interface states. Due to the lack of Fermi level pinning, D_s was assumed to be negligible in these calculations. The calculations were based on an oxide thickness of 20 Å and indicate that the reverse bias breakdown voltage for the Au/ZnSe contact would be > 30 volts if thermionic emission were dominating conduction. From these results, and the lack of any compound formation with a larger work function than Au, it is unlikely that thermionic emission dominated the Au/ZnSe contacts.

It also appears that the equations for field emission do not accurately model the I-V characteristics for the Au contacts. Field emission may be described by the exponential relationship in Eq. (2-5). By talking the natural log of Eq. (2-5), and with some simple rearrangements, Eq. (2-5) can be rewritten as follows:

$$\ln(I) = \ln(SJ_s) + \ln(-qV_R/E'). \qquad (3\text{-}3)$$

Based on this equation, a plot of the natural log of current vs voltage should produce a straight line if tunneling is dominating conduction. Figure 3.14 shows a plot of ln(I) vs V, over a voltage range of 0.5 to 3 volts, for the sputtered Au contacts heat treated at 350 °C for 30 minutes. In addition, the data from the Ag contacts heat treated at 150 °C for 45 minutes are also shown. In this plot, data collected below 0.5 volt were excluded since the measured current levels were below the noise level of the picoammeter. Values above 3 volts were also excluded since the bulk resistance of the semiconductor dominated in this range. Figure 3.14 shows that the plot of ln(I) vs V for the sputtered, heat treated Au contact did not produce a straight line indicating that tunneling was not dominating conduction. To understand the mechanism limiting charge transport, consider the following argument.

Schottky contacts are similar to one-sided abrupt semiconductor junctions in which avalanche multiplication begins to contribute to and dominates conduction at applied voltages of $4E_g/q$ and $6E_g/q$, respectively. In the case of the Au/ZnSe contacts heat treated at 350 °C, diffusion of Au also is expected to generate deep levels at 550 meV. Therefore, in these contacts, thermally excited carriers which initiate avalanche breakdown and carriers generated by impact ionization do not have to gain sufficient energy to be excited across the band gap. Instead, these charge carriers only have to gain sufficient energy to reach the 550 meV Au acceptor levels. This would lead to avalanche breakdown dominating conduction at lower voltages, provided the electric fields are high enough. If the 550 meV ionization potential of the Au defects is substituted for E_g in the $6E_g/q$ relationship, avalanche breakdown is predicted to dominate at 3.3 volts. This is in good agreement with the observed value of ~3 volts. The critical field strength for avalanche multiplication (E_c) is given by:

$$E_c = 2V_R/W \qquad (3\text{-}4)$$

where W is the depletion region width [Sze85, p. 101]. For a Schottky barrier, W can be calculated as follows [Sha84, p. 29]:

$$W = [(2\varepsilon_s/qN_d)\ |V_i - V_R|]^{1/2}. \qquad (3\text{-}5)$$

Using the same values as for the calculation of thermionic emission above, the depletion region width for the Au contacts is found to be ~100 nm at an applied bias of 3 volts. This yields a field strength of 6 x 10^7 V/m at breakdown. Since field strengths of 10^7 to 10^8 V/m are typically required for avalanche breakdown, this supports the postulate that avalanche breakdown occurred in the Au contacts. Based on these results and the abrupt change in conductivity for the Au contacts observed in figure 3.14, defect assisted avalanche breakdown is believed to be dominating conduction in the Au contacts.

Ag Contacts

For the sputtered Ag contacts, the work function of Ag (4.71 eV) is smaller than for Au (5.20 eV), which should lead to a higher ϕ_B for the Ag. Therefore, based on the Schottky model, the Ag contacts should have a higher reverse bias breakdown voltage than the Au contacts. On the contrary, the experimental results show that both the as deposited and heat treated Ag contacts had lower breakdown voltages than the Au contacts. SIMS data from the Ag contacts showed that significantly more oxygen (O) was present at the interfaces of the as deposited and 150 °C heat treated samples (Figs. 3.9a and 3.9b), as compared to the as deposited Au samples (Fig. 3.4a). After heat treatment at 300 °C, the O peak is found to drop by approximately an order of magnitude (Fig 3.9.c) and the contact resistance was found to increase. Due to the correlation between the I-V data and interfacial O, the electrical properties of the ZnSe are believed to be effected by this oxygen.

The presence of a larger concentration of O at the Ag/ZnSe interface, versus low concentrations at the Au/ZnSe interface is consistent with the reported values of permeation for O in Ag and Au. As discussed in chapter 2, O_2 has significant permeability through polycrystalline Ag (10^{-11} to 10^{-14} $cm^{-1}S^{-1}$ at temperatures ranging from 400 to 800 °C) which can be increased by approximately two orders of magnitude at 650 °C using a glow-discharge-assisted dissociation of the upstream O_2 [Out92]. In contrast, O_2 has negligible permeability through Au [Ebe92]. Residual O_2 in the sputter system during deposition of the contact metals is postulated to be dissociated by the glow-discharge of the magnetron source and to permeate through the Ag contact to the Ag/ZnSe interface. However, the O did not permeate through the Au contact, explaining the higher levels of O in the Ag contacts as opposed to the Au contacts. This also explains the lower reverse bias breakdown voltages of the as deposited Ag contacts, since O would be expected to reduce the barrier thickness by doping.

In order to verify the correlation with O, Ag contacts were evaporated onto p-ZnSe. Since this deposition process does not use a glow discharge, the amount of residual O incorporated into the Ag contacts was expected to be reduced. The similarity in as deposited I-V characteristics of the sputtered (Fig. 3.8) and evaporated (Fig. 3.13) Ag contacts indicates that incorporation of O was not reduced as significantly as expected. However, the reduction in breakdown voltage observed for evaporated Ag contacts heat treated in oxygen, and lack of reduction for those heat treated in forming gas provide further evidence that O plays an important role in the conduction mechanisms of the Ag/p-ZnSe contacts.

In chapter 2, oxygen was reported to be a shallow (~80 meV) p-type dopant in ZnSe [Aki89b] and exposure of ZnSe to an oxygen plasma prior to Au deposition were found to reduce barrier heights by generating a highly doped ZnSe surface region [Aki91]. Based on this information, one plausible explanation for the relation between the I-V data and O is that the O is doping the surface region of the ZnSe, resulting in conduction which is dominated by field emission. The plot of ln(I) vs V for Ag contacts in Fig 3.14 is linear, which is consistent with tunneling being the conduction mechanism.

An additional possibility is that the interfacial barrier was reduced, due to the high electronegativity of oxygen. As discussed in chapter 2, work reported by Chen et al. showed that several monolayers of Se deposited at the interface between Au and p-ZnSe resulted in a 0.25 eV reduction in ϕ_B. This drop in ϕ_B

was attributed to a reduction in the ZnSe work function due to termination by highly electronegative Se. According to the Pauling scale [Pau60], the electronegativity of Au and Se are fairly close at 2.4 eV while oxygen has a value of 3.5 eV. Since the electronegativity of O is significantly larger than for Se, interfacial O would be expected to result in a larger reduction in ϕ_B. Modeling of thermionic emission currents, using the same equations and values used above for Au contacts, indicate that ϕ_B would have to be reduced to ~0.75 eV for thermionic emission to result in the I-V characteristics observed for the Ag sample heat treated at 150 °C for 45 minutes. While this mechanism is a possibility, the linear plot of ln(I) vs V in Fig 3.14 is a strong indication that oxygen acts as a dopant, leading to field emission currents as opposed to thermionic emission.

Summary

The results from Au contacts indicate that Au diffusion into ZnSe results in a reduction in reverse bias breakdown voltage for Au/ZnSe Schottky contacts, with a minimum reverse bias breakdown voltage of 3 volts obtained for heat treatments at 350 °C for 30 minutes. The data also strongly indicate that this reduction occurred due to Au diffusion, resulting in 550 meV defect states which allowed defect assisted avalanche breakdown to dominate conduction. Conduction in th Au contacts was not by defect assisted tunneling. Results for the Ag contacts also indicate that heat treatments did not lead to defect assisted tunneling. The minimum breakdown voltages for Ag contacts heat treated at 150 °C for 45 minutes were found to be 2.3 volts, which is 0.7 volts less than for Au contacts. These results indicate that interfacial oxygen was responsible for the low reverse bias breakdown voltage, and is believed to act as a co-dopant in ZnSe. Additional work outlined in chapter 7 would help verify O as a co-dopant. However, it is doubtful that a heat treatment could be developed which would result in ohmic contacts.

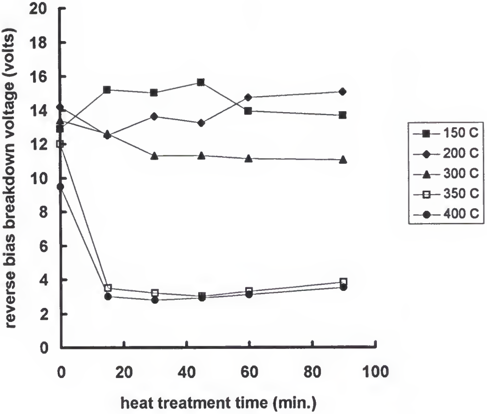

Figure 3.1: Plot of reverse bias breakdown voltage for sputter deposited Au/ZnSe contacts heat treated in forming gas at 150, 200, 300, and 400 °C.

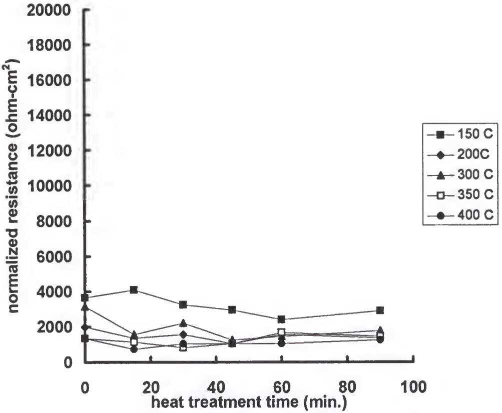

Figure 3.2: Plot of normalized resistance for sputter deposited Au/p-ZnSe contacts heat treated in forming gas at 150, 200, 300, 350, and 400 °C.

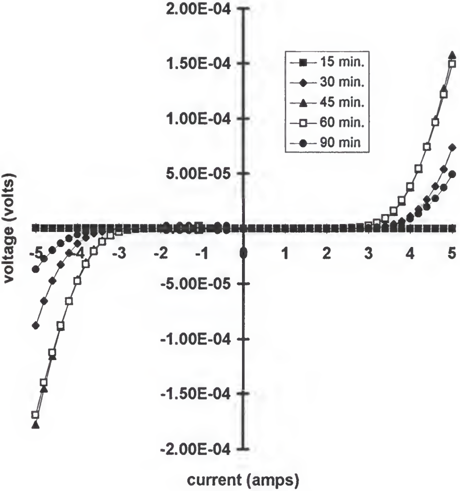

Figure 3.3: Current vs voltage characteristics for sputter deposited Au contacts heat treated in forming gas at 350 °C for 15, 30, 45, 60, and 90 minutes.

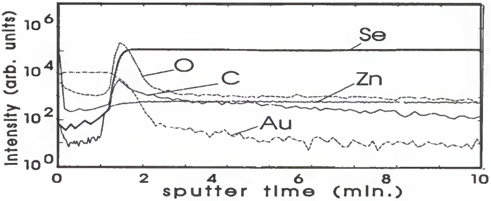

(a)

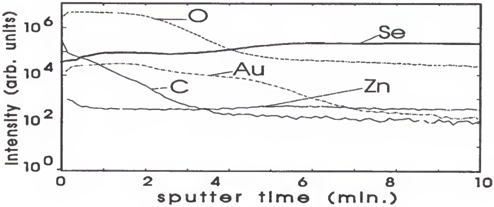

(b)

Figure 3.4: SIMS data for as deposited Au/p-ZnSe contacts, and b) contacts heat treated in forming gas at 350 °C for 90 minutes.

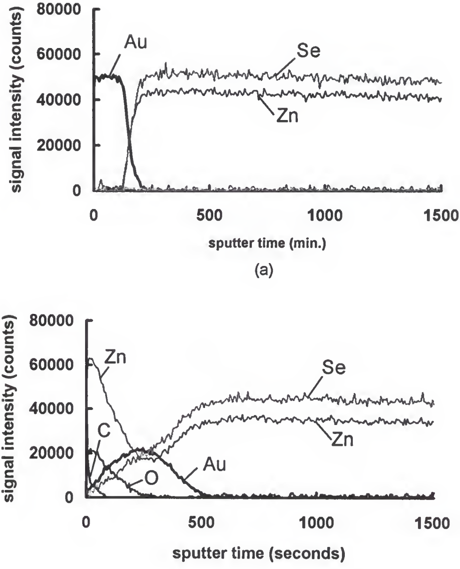

(a)

(b)

Figure 3.5: a) Auger sputter depth profiles for as deposited Au/p-ZnSe contacts, and b) contacts heat treated in forming gas at 350 °C for 90 minutes.

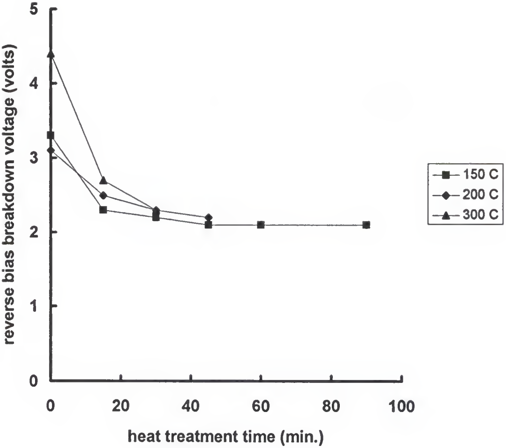

Figure 3.6: Plot of reverse bias breakdown voltage for sputter deposited Ag/p-ZnSe contacts heat treated in forming gas at 150, 200, and 300 °C.

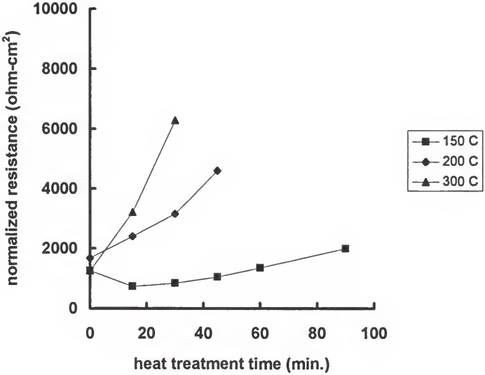

Figure 3.7: Plot of normalized resistance for sputter deposited Ag/p-ZnSe contacts heat treated at 150, 200, and 300 °C.

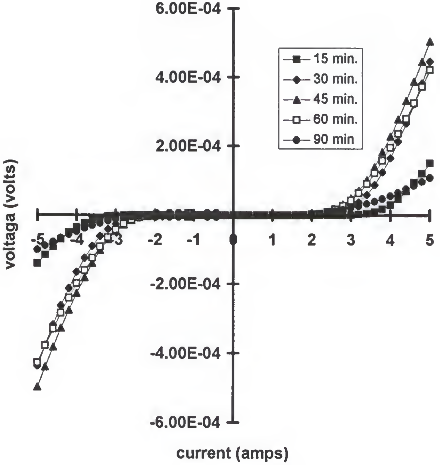

Figure 3.8: Current vs voltage characteristics for Ag/p-ZnSe contacts heat treated in forming gas at 150 °C for 15, 30, 45, 60, and 90 minutes.

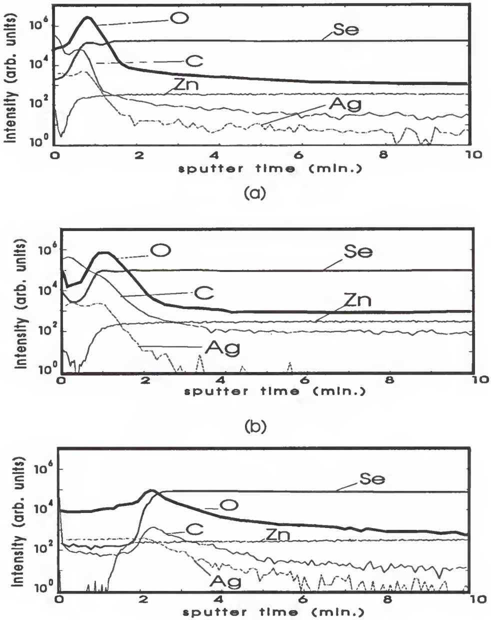

(a)

(b)

(c)

Figure 3.9: a) SIMS data for as deposited Ag/p-ZnSe contacts, b) contacts heat treated in forming gas at 150 °C for 90 minutes, and c) contacts heat treated in forming gas at 300 °C for 30 minutes.

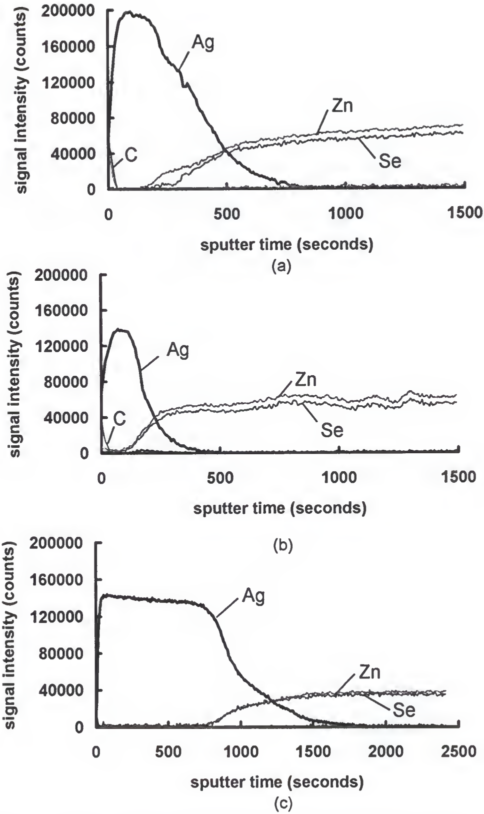

Figure 3.10: Auger sputter depth profile from as deposited Ag/p-ZnSe contacts, and b) contacts heat treated in forming gas at 150 °C for 90 minutes, and c) contacts heat treated in forming gas at 300 °C for 30 minutes.

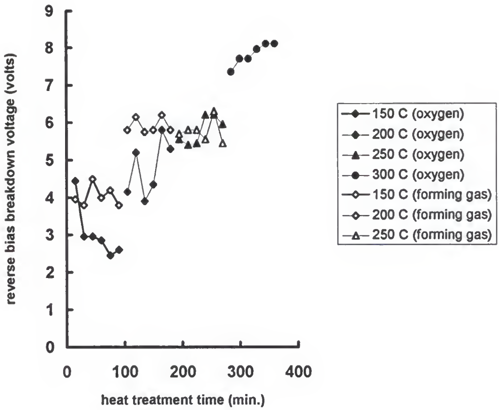

Figure 3.11: Reverse bias breakdown voltage for evaporated Ag/p-ZnSe contacts heat treated in oxygen and forming gas at 150, 200, 250, and 300 °C.

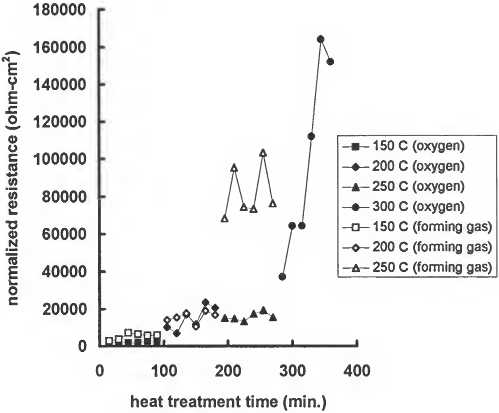

Figure 3.12: Normalized resistance for evaporated Ag/p-ZnSe contacts heat treated in oxygen and forming gas at 150, 200, 250, and 300 °C.

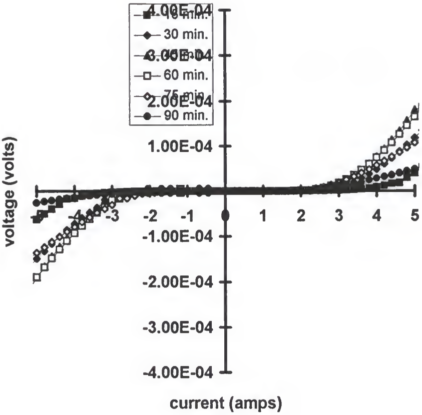

Figure 3.13: Current vs voltage characteristics for evaporated Ag contacts heat treated at 150 °C in oxygen for 15, 30, 45, 60, 75, and 90 minutes.

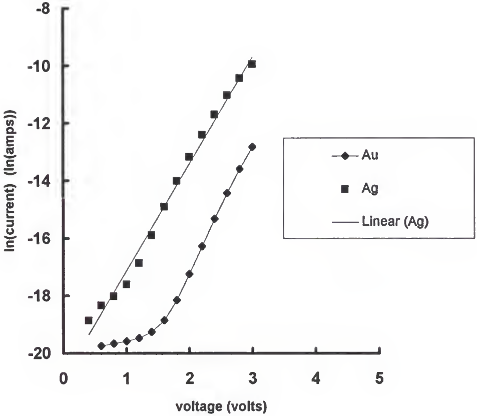

Figure 3.14: Plot of ln(current) vs voltage for sputter deposited Au contacts heat treated at 350 °C for 45 minutes and Ag contacts heat treated at 150 °C for 30 minutes.

CHAPTER 4

HgSe CONTACTS

Introduction

The work described in the following chapter, discusses an *ex situ* method of forming HgSe contacts to p-ZnSe. This process involves capping the samples with Se, prior to removing it form the MBE growth chamber, then heating the capped sample in Hg vapor to form HgSe. Auger, X-ray, and TEM were used to characterize the composition and structure of the contacts. Temperature dependant current vs voltage data were used to measure the valance band offset and conduction mechanisms across the HgSe/p-ZnSe interface.

Experimental Setup

The p-ZnSe samples used for HgSe contact studies were grown by molecular beam epitaxy (MBE) on semiinsulating GaAs. The MBE system used to grow the ZnSe consisted of a UHV stainless steel chamber which was pumped by a CTI Cryo Torr 8 cryo pump and has an ultimate pressure of $\sim 2\times10^{-9}$ torr. Prior to the growth of the ZnSe, the GaAs substrates were heated to 450 °C in a hydrogen atmosphere to desorb the native oxide [Rou93]. This process resulted in a clean , smooth GaAs surface, verified by reflectance high energy electron diffraction (RHEED). Following the removal of the oxide, a 1 to 4 μm undoped ZnSe buffer layer was grown. During the growth of ZnSe, pressure in the system was ~10^{-7} Torr, the ratio of the Se and Zn beam flux were 2:1 (measured using an ionization gauge), and the substrate temperature was 298 °C. Next, the p-ZnSe was grown using nitrogen radial doping from an Oxford source, with a nitrogen background pressure of 10^{-6} Torr. This yielded carrier concentrations in the low to mid 10^{17} cm^{-3} range [Par90]. Immediately following growth, the ZnSe was capped with Se. This was accomplished by closing the shutter on the Zn effusion cell and leaving the Se effusion shutter open while the substrate was allowed to cool. The sample was monitored by laser reflectance interferometry (LRI) to determine the thickness of the Se capping layer [Rou92]. The LRI measurements indicated that the deposition of Se began when the substrate temperature cooled to ~90 °C, and was terminated by closing the Se effusion cell shutter when a thickness of 1500 Å was reached. Once the capping was completed, the samples were removed from the MBE growth chamber.

Upon removal from the MBE chamber, the capped ZnSe was cleaved into ~4x5 mm sections, which were then inserted into the system shown in figure 4.1 where the Se capping layer was reacted with Hg to form HgSe. This system (Fig. 4.1) consists of a 200 ml Pyrex flask which contained ~5 grams of liquid Hg and a stainless steel chamber with a volume of ~ 25 cm^3 constructed from ultra high vacuum (UHV) components. The capped sample was located in the stainless steel chamber during the reaction. Tygon tubing (1/4") was used to connect a 99.99% pure nitrogen (N_2) gas cylinder to the Pyrex flask, a second section of tubing connected the flask to the stainless steel chamber, and a third section connected the steel chamber to a Hg scrubber. N_2 gas, monitored by a rotameter, was flowed from the flask to the chamber at 100 ml/min. The flask containing the Hg was heated to 100 °C, in a boiling water bath, to produce Hg vapor (the equilibrium vapor pressure of Hg at 100 °C is 0.3 Torr) which was transported to the stainless steel chamber by entrainment in the flowing N_2. Using a thermocouple to monitor temperature, the chamber was heated to 150 °C by a hot plate, driving the reaction of the Se capping layer with the Hg Vapor.

During the reaction process, the samples were inserted in the stainless steel chamber, the Hg was heated to 100 °C, and the N_2 gas was turned on prior to heating the sample. The sample temperature was ramped from room temperature to 150 °C over a ~45 minutes period and held at 150 °C for times ranging from 5 to 45 minutes. The samples were then removed from the stainless steel chamber and cooled to room temperature in air.

For samples made for electrical characterization, the HgSe was patterned into dot contacts using adhesive (Scotch) tape with 1 mm diameter holes spaced 1 mm apart. The tape was applied to the Se capped surface of the p-ZnSe samples prior to insertion in the stainless steel chamber, and remained on the samples until they were removed from the reaction chamber. The adhesive tape was used to restrict exposure of the Se capping layer to the Hg vapor. Auger sputter depth profiling, which will be discussed in the results section of this chapter, confirm that HgSe did not form in the areas masked by the adhesive tape.

Temperature dependant I-V measurements were used to determine the conduction mechanisms dominating in the HgSe/p-ZnSe contacts. These measurements were performed by mounting the samples on an ADP cold finger/heater stage with a Scientific Instruments Inc. Series 5500 temperature controller. This stage was used to heat the samples from 290 to 390 °K. Silver epoxy was used to connect electrodes to two separate HgSe/p-ZnSe contacts. Therefore, the I-V data was collected from two back-to-back Schottky diodes. The I-V data were collected for applied biases of -10 to +10 volts using the same automated setup and curve tracer used for the Au and Ag contacts described in the experimental setup section of chapter 3. The temperature was increased in 10 to 15 °K increments and required ~30 minutes between measurements for the temperature to stabilize.

Four additional types of samples were made for analytical characterization. Samples made for cross sectional transmission electron spectroscopy (XTEM) analysis had a similar structure as those made for electrical characterization, except that a thicker Se cap was used (3000 Å) to provide a large cross sectional area. The XTEM samples were reacted without patterning for 45 minutes at 150 °C in Hg vapor. Cross sections were cut by a diamond saw and thinned by mechanical polishing, then thinned to < 2000 Å by ion milling. The samples were analyzed using a JEOL 4000 FX high resolution transmission electron microscope with energy dispersive spectroscopy (EDS) capabilities for X-rays.

Samples for X-ray diffraction (XRD) analysis were made using Se evaporated onto glass slides, instead of Se capped ZnSe. Glass slides were chosen as substrates because they are amorphous and therefore do not generate X-ray diffraction peaks. The thermal evaporator used to deposit the Se onto the glass slides was the same evaporator used to deposit Ag contacts and was described in the experimental setup section of chapter 3. The base pressure in the thermal evaporator used to deposit Se was ~ 5×10^{-7} Torr. Se was deposited at 20 Å/sec. from an alumina crucible heated by a tungsten filament, onto a substrate which was at room temperature. The final thickness of the Se film was ~ 4500 Å as measured by the Inficon quartz crystal monitor. These samples were reacted at a temperature of 150 °C for 45 minutes. These parameters were chosen to produce a samples which would closely resemble the electrical contacts, but could also be examined by X-ray diffraction to verify the structure of the HgSe. The samples were analyzed using a Phillips APD 3720 powder diffractometer using Cu Kα radiation over a range of $0° \leq \theta \leq 100°$, with 0.05 ° increments and 20.0 second collection times per degree. In addition to the reacted sample, an as deposited samples was also characterized by XRD to determine the structure of the as deposited Se.

The third set of samples were made for compositonal analysis of the HgSe contacts on p-ZnSe using Auger electron spectroscopy (AES). These samples were fabricated by thermally evaporating a 3700 Å layer of Se onto room temperature ZnSe. Patterned (1 mm dot) samples were formed by reaction at 150 °C for 45 minutes in Hg vapor. Auger analysis was performed using a PHI 660 scanning Auger system with a ~30 nA, 10 KeV primary electron beam and the sample tilted at 30°. Sputtering for the depth profile was performed using a 3 KeV argon ion beam with a 3mm x 3mm raster. These conditions resulted in a sputter rate of ~100 Å/minute for Ta_2O_5.

A final set of HgSe samples were made so that both X-ray and Auger analysis could be used to identify diffusion and /or intermediate reaction occurring during the formation of HgSe. These samples had a similar structure as the X-ray samples discussed above, with 8,000 to 10,000 Å of Se thermally evaporated onto glass slides. These samples were heat treated in Hg vapor at temperatures of 25, 50, and 70 °C for 60 minutes. X-ray analysis was performed using the same parameters as above while Auger was performed using a ~20 nA, 5 KeV primary electron beam. The lower beam current and energy were required to prevent the Auger's primary electron beam from damaging the thick Se layer.

Results

The temperature dependant I-V data from contacts held for 15 minutes at 150 °C (423 °K) in Hg vapor are shown in figure 4.2. These data show that both the as deposited and heat treated HgSe/p-ZnSe contacts were rectifying. For temperature dependant I-V data taken between the temperatures 291 °K and 350 °K, the current increased and the reverse bias breakdown voltages decreased with increasing temperature . At temperatures $\geq$ 360 °K, a large drop in current was observed, indicating degradation of the contacts and/or ZnSe epilayer. The degradation was larger at higher temperatures and was irreversible upon cooling.

XRD data from the HgSe samples on glass slides reacted at 150 °C for 45 minutes matched the 2θ angles and relative intensities of X-ray diffraction peaks for cubic HgSe reported in the JCPDS files [Mcc88, File No. 8-469]. Both the experimental data and cataloged data (JCPDS) are shown in Table 4-1. Note that all HgSe peaks in the JCPDS data with intensities > 2% were observed in the experimental data. Two additional peaks at 2θ angles of 23.5° and 48.7° were also observed in the experimental data. These peaks were found to correspond to cataloged peaks for hexagonal Se [Mcc88, File No. 6-362]. The XRD data from the as deposited Se on glass slides showed no identifiable diffraction peaks, indicating that it was amorphous.

Table 4.1

Experimental XRD data for Se on glass slide reacted for 45 minutes at 150 °C in Hg vapor compared to XRD data from JCPDS files for cubic HgSe and hexagonal Se

reacted sample		HgSe (cubic)		Se (hexagonal)	
2Θ angle	Intensity (%)	2Θ angle	Intensity (%)	2Θ angle	Intensity (%)
23.55*	26.9	25.35	100	23.51	55
25.33	100	29.35	16	29.70	100
29.31	7.9	41.96	50	41.30	16
41.97	34.7	49.64	30	43.64	35
48.17*	1.7	52.00	4	45.35	20
49.62	20.5	60.85	6	48.10	4
51.87	1.9	66.97	10	51.72	20
60.77	2.7	68.94	2	55.65	10
66.95	3.6	76.63	8	56.14	12
76.58	3.4	82.29	4	61.21	8
82.19	1.6	91.46	2	61.66	10
91.35	1.0	96.98	4	65.27	10
97.19	1.4	98.85	<1	68.25	4
				71.59	6

*hexagonal Se; balance of peaks from cubic HgSe

Auger depth profiles from the HgSe dot contacts and from a p-ZnSe region between dot contacts are shown in figures 4.3 and 4.4, respectively. From the dot contacts region, the Auger data has constant signals for Hg and Se over the first 10 minutes of sputtering. After 10 minutes of sputtering , the Hg signal began to decline and the Zn signal began to increase above zero. These trends continued until about 27 minutes of sputter time, when the Hg signal intensity had dropped to zero and the Zn signal has maximized. Note that the Se signal remained at a constant value throughout the depth profile. The Auger data taken on the masked area between dot contacts show a constant signal intensity for Se and Zn with no Hg being detected. Note that the signal intensities for the Se and Zn profiles on the masked area closely match the signal intensities for these elements at the end of the profile take on the dot contacts.

The TEM diffraction data from reacted samples were consistent with the formation of crystalline HgSe (Fig. 4.5). Energy dispersive spectrometry of X-rays (EDS) were used in the TEM to verify that the reacted compound consisted of Hg and Se, and to verify the composition of the ZnSe substrate. Matched sets of diffraction patterns from the interface between ZnSe and HgSe indicate that at least some regions of the HgSe formed epitaxial layers on the ZnSe (Fig. 4.5). An image at 100K magnification showing isolated regions of HgSe which have formed on the ZnSe surface is shown in figure 4.6. Figure 4.7 shows areas where these HgSe has coalesced into a continuous film. High resolution images, at a magnification of 500K, of the interface between the HgSe and ZnSe are shown in Figure 4.8. The composition of the material surrounding the HgSe could not be verified by EDS and is presumed to have originally consisted of Se which sublimated away, or was mechanically removed during sample preparation.

A montage display of the X-ray data from the HgSe samples on glass slides heat treated in Hg vapor at 25, 50, and 70 °C is shown in figure 4.9. In addition, the X-ray data for the sample heat treated at 150 °C for 45 minutes are also shown for comparison. These data indicate that only very small fractions of HgSe were present in the 25 and 50 °C samples, suggesting the layers were primarily amorphous. The Auger data from the 25 and 50 °C samples, shown in Figs. 4.10 and 4.11, indicate a surface coverage of Hg but no diffusion into the Se layer. Diffraction peaks with 2θ angles which correspond to HgSe were observed for the 70 °C sample, although their relative peak heights do not match the JCPDS data. The Auger data for this sample (Fig. 4.12) indicates that a significant amount of Hg is present in the surface region of the Se layer. After ~ 10 minutes of sputter time, the Hg signal dropped in intensity and then remained constant, at this reduced value, until the Se/glass interface was reached. Note that once the Se/SiO_2 interface was reached, the signals were very noisy due to charging of the glass slide which caused spurious signals when the HgSe was sputtered away. Therefore these data are not shown.

Discussion

HgSe Formation

Atmospheric exposure and *ex situ* processing of the Se capped p-ZnSe samples was expected to be possible due to the reported passivation and protection provided by Se capping of ZnSe [Jon88]. These reports indicate that a Se cap prevented oxidation or contamination of the Se surface upon exposure to atmosphere. This layer was easily removed by heating the sample to 115-150 °C in ultrahigh vacuum, which yielded a clean single crystal, stoichiometric, and well ordered ZnSe surface.

X-ray data from Se/glass samples and dot contacts on ZnSe, both heat treated at 150 °C for 45 minutes, indicated that HgSe was formed using the *ex situ* process outlined in this dissertation. From the TEM results, the HgSe was shown to form at the Se/ZnSe interface as small (50 to 200 nm) isolated precipitates which were oriented to the ZnSe (similar to a coherent precipitate). This unique micro structure indicated a complex series of events must take place during the formation of HgSe to result in the epitaxial growth. The HgSe reaction process is believed to begin with the diffusion of Hg into Se. The equilibrium binary phase diagram calculated for the Hg-Se system indicated that there is no solid solubility of Hg in Se below the melting temperature of Se (221 °C) [Shu69]. Instead a two phase region exists between Se and HgSe. In addition, HgSe has a stoichiometry range of 48.8 to 50.75 at. % Se at room temperature. However, the phase diagram cannot accurately describe the behavior of the Se capping layer because it is in a metastable amorphous state (a-Se), as reported above. The formation of a-Se is consistent with literature reports indicating a-Se was obtained from evaporative deposition on Al at temperatures below the peak recrystallization temperature [Lar81, Kas87, Kas93]. It has been reported that a-Se had a glass transition temperature (T_g) between 30 and 60 ° C, a peak recystallization temperature (T_c) between 110 and 140 °C, and was composed of 30-50 % Se_8 rings with the remainder forming Se_x polymer-like chains. Due to this open structure, a-Se is expected to have far greater solubility for Hg as compared to crystalline Se. As a result, an a-Se/Hg solid solution is believed to have formed during the 45 minutes required to ramp the temperature of the Se capped ZnSe samples (in Hg vapor) up to 150 °C.

Heating the a-Se/Hg solid solution above the peak recrystallization temperature (110 to 140 °C) is believed to result in devitrification, causing the transformation of metastable a-Se and Hg to the HgSe phase predicted by the equilibrium phase diagram. Therefore, devitrification caused the Hg in solution to precipitate out as HgSe and the remaining Se had a hexagonal crystal structure. The hexagonal phase (trigonal) was reported to consist of Se_x chains in a helical pattern [Kot92, Oze90]. In this work, the growth of Se crystallites from a-Se films on Al_2O_3 were found to nucleate at the substrate/film interface and propagate toward the Se film surface. This must have resulted from a higher Se/a-Se interface energy $\gamma_{se/a\text{-}Se}$ as compared to a lower substrate/Se interface energy $\gamma_{S/Se}$. Since the crystal structure (zinc blend) and lattice constant for ZnSe (5.668 Å) and HgSe (6.084 Å) are similar, $\gamma_{ZnSe/HgSe}$ would be expected to be low. In the case of epitaxy, this interface would be eliminated, resulting in low or zero interfacial energy. In either case, precipitates of HgSe would be expected to nucleate at the Se/ZnSe interface. This was observed by TEM analysis in regions where HgSe precipitates had formed but had not yet coalesced into a continuous film (Fig 4.5).

The Se/glass samples heat treated at 25, 50, and 70 °C were used to determine the reaction steps which took place during the formation of HgSe. The Se layer was much thicker for these samples (8,000- 10,000 Å) as opposed to other samples, to help determine the diffusion profile of Hg through Se. The Auger data from these samples indicate that Hg did not diffuse at temperatures below 25 and 50 °C but significant diffusion occurred at temperatures $\geq$ 70 °C. X-ray data from the sample heat treated at 70 °C indicates that some of the diffused Hg has reacted with the Se to form HgSe. In addition, some of the Se has devitrified to form crystalline Se (Fig 4.9). The HgSe is believed to have formed in the top third of the Se layer. This conclusion is based on similarity between the relative intensity of the Hg and Se signals in the surface region of the 70 °C sample (Fig. 4.12) and the HgSe region of the sample heat treated to 150 °C (Fig. 4.3)

Despite the apparent formation of some HgSe at 70 °C, the most important observation from the Auger depth profile is the significant amount of Hg present throughout the bottom two thirds of the 8,000-10,000 Å Se layer. This indicates that Hg had diffused through the 8,000 to 10,000 Å layer during heat treatment at 70 ° C for 60 minutes. Since the x-ray peak intensities for HgSe were significantly lower for the 8,000-10,000 Å sample (70 °C) than for the 1500 Å sample (150 °C), the majority of the 70 °C sample was believed to consist of a-Se. Therefore, the combined results showing diffusion of Hg and relatively small amount of HgSe or crystalline Se verifies the formation of an a-Se/Hg solid solution prior to the precipitation of HgSe.

Electrical Characterization

Temperature dependant I-V data were collected and analyzed to determine the conduction mechanisms and barrier heights for thermionic emission. The data were reduced using the equations for reverse bias conduction for Schottky diodes. In this analysis, the HgSe was treated as a metal due to its' negative band gap and high carrier concentrations which are 1 to 2 orders of magnitude greater than the p-ZnSe. For contacts dominated by thermionic emission over the valence band offset, the saturation current is described by Eq. 2-2. A simple rearrangement of this equation yielded the following:

$$\ln(I_o/T^2) = \ln(SA^*)+(\Delta\phi_B-\phi_B)/kT. \qquad (4\text{-}1)$$

From this equation, plotting the temperature dependant I-V data as $\ln(I_o/T^2)$ vs $1/T$ should produce a straight line if thermionic emission was the only mechanism resulting in conduction. The slope of this line multiplied by -k is equal to ϕ_B-$\Delta\phi_B$. From the equation for image force reduction shown in Eq. 2-4, the value of ϕ_B-$\Delta\phi_B$ should vary as a function of $(V_R)^{1/4}$. Therefore, by determining ϕ_B-$\Delta\phi_B$ over a range of values for V_R, a plot of ϕ_B-$\Delta\phi_B$ vs $(V_R)^{1/4}$ can be obtained which should also produce a straight line. Extrapolation of this line at zero reverse bias yielded the barrier height, ϕ_B, which is equal to the valence band offset for contacts dominated by thermionic emission.

A typical plot of $\ln(I_o/T^2)$ vs $1/T$ for the HgSe/p-ZnSe contacts is shown in figure 4.13. From these data, a plot of ϕ_B-$\Delta\phi_B$ vs $(V_R)^{1/4}$ was produced which is shown in figure 4.14. Due to the degradation of these contacts (increased resistance) which occurred at temperatures > 360 °K, the data fitted to the ϕ_B-$\Delta\phi_B$ vs $(V_R)^{1/4}$ plots were limited to data collected at temperatures below 360 °K. Possible reasons for this degradation are discussed below.

The data for the HgSe samples plotted as ϕ_B-$\Delta\phi_B$ vs $(V_R)^{1/4}$ do not produce a completely straight line. Instead the plots have a knee in the curve which occurs at a reverse bias of ~2.5 volts (1.25 volts$^{1/4}$), resulting in two lines with different slopes (Fig. 4.14). The two different slopes indicate a change in activation energy for conduction across the HgSe/p-ZnSe interface. Extrapolation of the best fit line for V_R between 0 and 2.5 volts yields a barrier of ~0.55 eV, which is in good agreement with the expected value of 0.6 eV [Lan92]. This indicates that thermionic emission is responsible for the I-V characteristics of the contacts for $V_R < 2.5$ volts. Further, the barrier height clearly suggests that the Fermi level of ZnSe is not pinned at the surface, consistent with previous literature reports.

The equation for thermionic field emission in a reversed biased Schottky diode can be used to explain the I-V characteristics for a reverse voltage $V_R >$ 2.5 volts. Thermionic field emission in Schottky diodes is a commonly observed transport mechanism at lower carrier concentrations under reverse bias because even moderate reverse biases cause the potential barrier to become sufficiently thin to tunnel through the top of the barrier. Charge carriers, with thermal energies large enough to reach the thin region of the barrier, have a much greater probability of tunneling through the barrier rather than attaining sufficient thermal energy to be emitted over the barrier. The equations for current (I) generated by thermionic field emission in a reversed Schottky diode are given in Eq. 2-5 through 2-9, and as shown in chapter 3, Eq. 2-5 can be rewritten to show that a plot of ln(I) vs V_R should produce a straight line if thermionic field emission is dominating conduction (Eq. 3-3). The reciprocal slope of this line multiplied by

-q yields the value of -E'. E_{oo} can be determined from the experimental data using equation 2-7 and the experimental value of E'. These values can be compared to theoretically determined values of E_{oo} (calculated using equation 2-9). For the HgSe contacts heat treated at 150 °C for 15 minutes, the temperature dependant I-V data collected for $V_R > 2.5$ volts does produce a straight line when plotted as ln(I) vs V_R. These data are shown in figure 4.15. The value of E_{oo} calculated from the data was found to vary from 0.0073 to 0.0086 eV. The average value for E_{oo} was 0.007 eV which is in reasonable agreement with the theoretical value of 0.005 eV. As with thermionic emission, data collected at temperatures > 360 °C were not used due to degradation of the contacts.

Thus temperature dependant I-V data indicate that thermionic emission dominates for $V_R < 2.5$ volts and that thermionic field emission dominates for $V_R > 2.5$ volts. This is in agreement with I-V curves predicted for the HgSe/p-ZnSe contacts using the thermionic and thermionic filed emission equations from chapter 2. The current versus voltage curves from these calculations are shown in figure 4.16, in which thermionic emission dominates conduction for V_R up to 5 volts after which thermionic field emission currents dominate conduction. For $V_R > 5$ volts, the top of the barrier becomes sufficiently thin allowing tunneling to occur. The reverse bias crossover between the two conduction mechanisms is larger for the theoretical curves (5 V) than observed experimentally (2.5 V), probably due to the fact that the effect of image force reduction is neglected in the thermionic field emission equations. Image force reduction will result in thermionic emission currents which are slightly larger than predicted, causing crossover at a lower voltage.

A possible explanation for the degradation of contacts at temperatures >360 °K can be obtained by reviewing the electrical properties of HgSe. HgSe is an n-type semimetal with charge carriers generated by ionized donor-type defects [Kum76]. The dominant point defects in HgSe, indicated by thermodynamic analysis, are Hg interstitials and Schottky vacancies. Hg interstitials are doubly ionized donors and therefore control the carrier concentration. Heat treatment of HgSe single crystals in Hg vapor has been shown to increase the carrier concentrations at 200 °C for 16 to 36 hours, from the low 10^{17} cm^{-3} to the high 10^{18} cm^{-3} range. This corresponds to an increase in Hg vapor pressure of 10^{-6} atm (RT) to 10^{-4} atm (200 °C). This increase in carrier concentration is believed to result from an increase in Hg interstitials incorporated during heat treatment. Without an over pressure of Hg vapor, Hg interstitials will diffuse to the surface of HgSe and vaporize, reducing the carrier concentration. Loss of Hg interstitials during the temperature dependant I-V measurements would result in the experimentally observed degradation of the contacts. This suggests the possibility that HgSe contacts are inherently thermally unstable.

Summary

The analytical results have shown that a stoichiometric, epitaxial HgSe layer was formed using the *ex situ* process described in this chapter. In addition, the results verified the ability to form a solid solution of Hg in a-Se, which was a critical step in the formation of HgSe. The electrical characterization identified a valence band offset of 0.5 eV across the HgSe interface, and that the dominant conduction mechanism was thermionic emission for V_R <3 volts but changes to thermionic field emission for V_R > 3 volts.

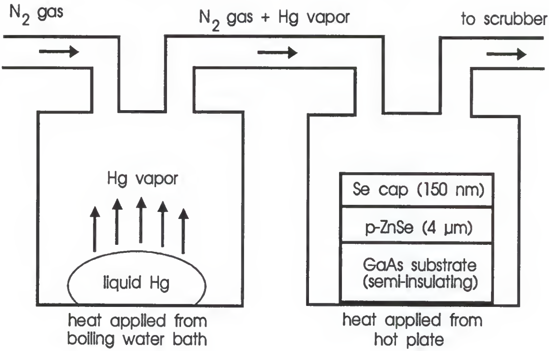
N_2 gas
N_2 gas + Hg vapor
to scrubber
Hg vapor
liquid Hg
Se cap (150 nm)
p-ZnSe (4 μm)
GaAs substrate (semi-insulating)
heat applied from boiling water bath
heat applied from hot plate

Figure 4.1: Schematic of system used to react Hg vapor with the Se capping layer to form HgSe contacts.

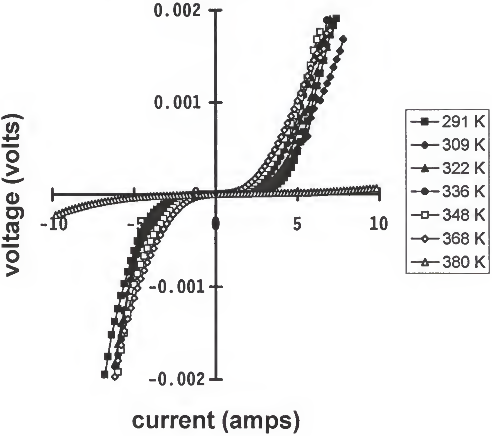

Figure 4.2: I-V data for HgSe/p-ZnSe contacts reacted for 15 minutes in Hg vapor. The data was taken over temperatures ranging form 291 to 380 °K.

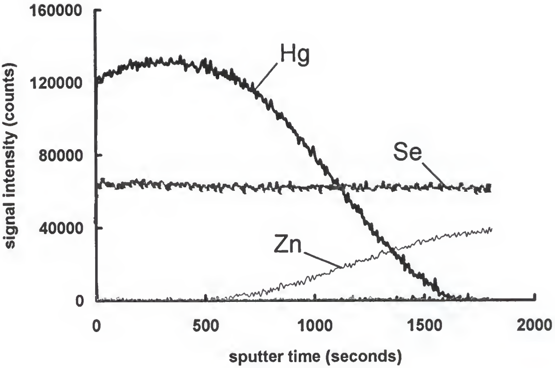

Figure 4.3: Auger depth profiles of HgSe/ZnSe contacts formed by reacting ZnSe with a 370 nm Se layer in Hg vapor at 150 °C for 45 minutes. Note that the Se signal intensity remains contacts throughout the profile indicating all the Se has reacted to form HgSe.

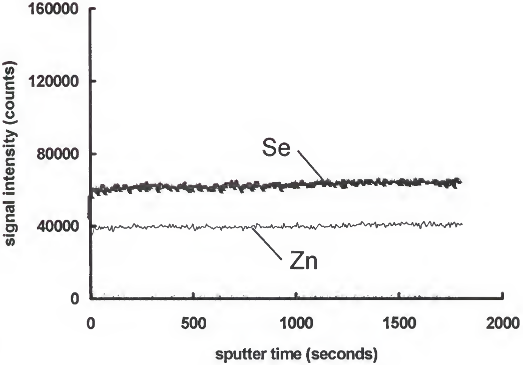

Figure 4.4: Auger depth profile of ZnSe region between HgSe dot contacts. Note that no Hg (or HgSe) is present on the surface of the sample indicating that the adhesive tape successfully masked the sample surface from exposure to Hg vapor. Also note that the Se surface layer has been removed, presumably by removal of the adhesive tape followed by cleaning in acetone , methanol, and deionized water.

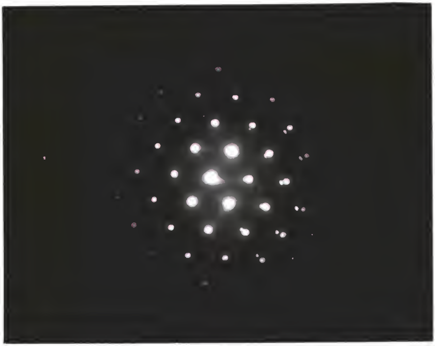

Figure 4.5: Diffraction pattern from the interface between HgSe and ZnSe. Note the matched set of diffraction patterns indicating epitaxial growth of HgSe.

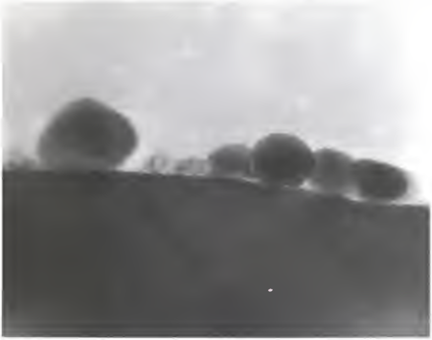

Figure 4.6: TEM image showing 50 to 200 nm isolated precipitates of HgSe which have formed on ZnSe by reacting an Se/ZnSe sample in Hg vapor for 45 minutes at 150 °C.

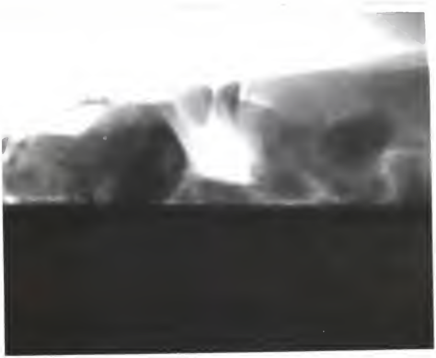

Figure 4.7: TEM image showing a region were a continuous layer of HgSe has formed.

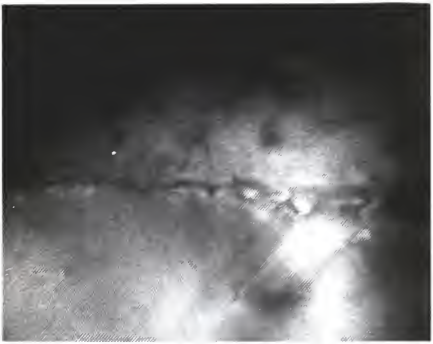

Figure 4.8: High resolution TEM image of HgSe (top)/ZnSe (bottom) interface. Note that the interface is rough but epitaxial.

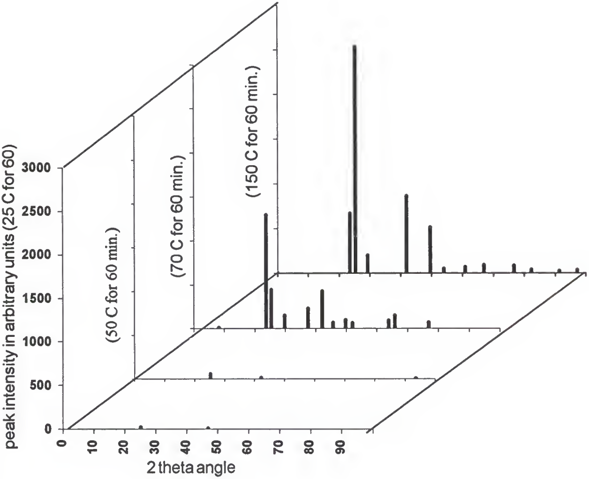

Figure 4.9: Montage display of X-ray data from HgSe samples on glass slides heat treated at 25, 50, 70, and 110 °C in Hg vapor for 60 minutes. Also included for comparison is the X-ray data from an HgSe sample on a glass slide heat treated at 150 °C for 45 minutes.

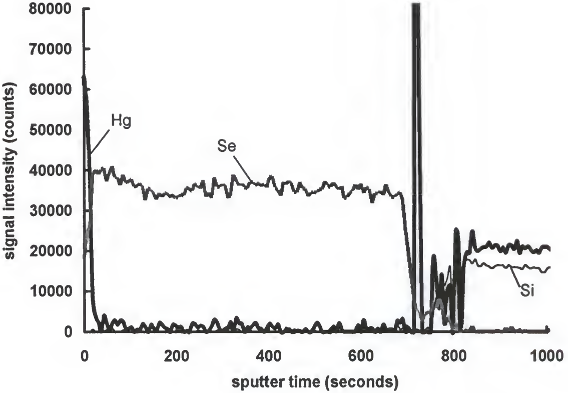

Figure 4.10: Auger depth profile of Se/glass sample reacted in Hg vapor at 25 °C for 60 minutes. Note the spike in the Hg signal at the interface and anomalous Hg signal after the glass slide is reached, resulting from charging of the glass slide.

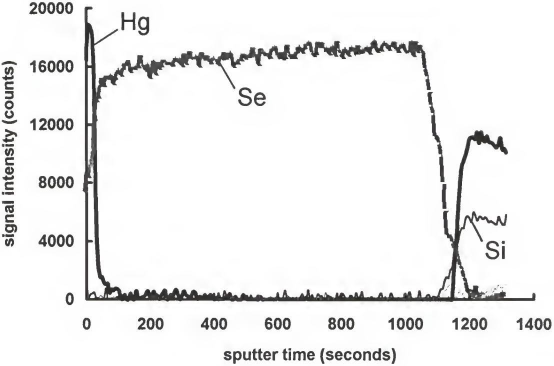

Figure 4.11: Auger depth profile of Se/glass sample heat treated at 50 °C for 60 minutes. As in figure 4.10, an anomalous Hg signal is observed once the glass substrate is reached due to charging.

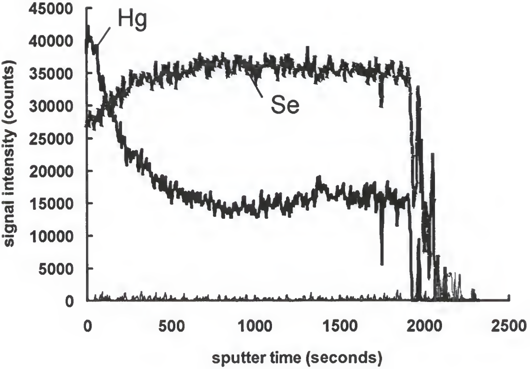

Figure 4.12: Auger depth profile of Se/glass sample reacted in Hg vapor at 75 °C for 60 minutes. The profile shows that an HgSe layer has formed in the top third of the sample, while Hg has diffused into the underlying amorphous Se without reacting. Auger signals were not detectable once the Se/glass interface was reached due to charging.

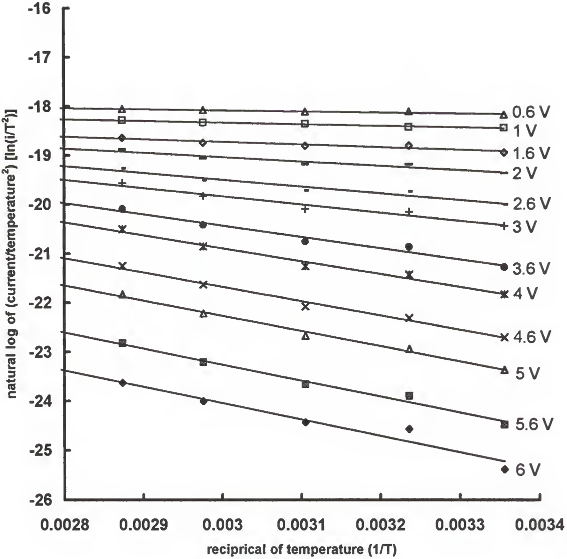

Figure 4.13: Plot of ln (I/T^2) vs 1/T for HgSe/p-ZnSe contacts with reverse biases ranging from 0.6 to 6 volts. The slope of these lines yield the value of ϕ_B-$\Delta\phi_B$ for the given reverse bias (V_R).

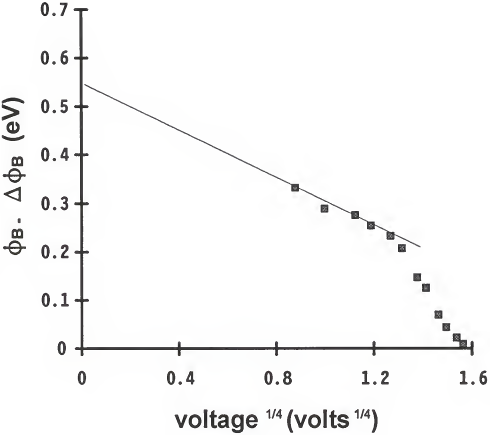

Figure 4.14: Plot of ϕ_B-$\Delta\phi_B$ vs voltage$^{1/4}$ for HgSe/p-ZnSe contacts held for 15 minutes at 150 °C in Hg vapor, indicating a barrier height of 0.55 eV.

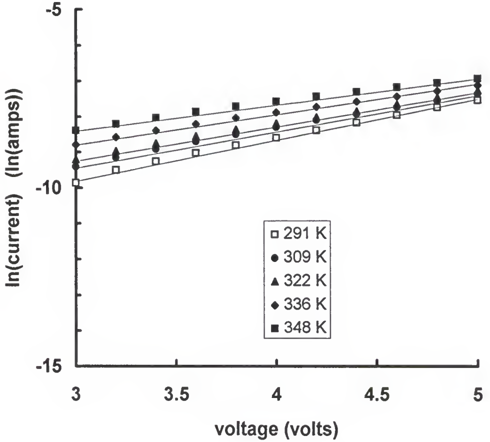

Figure 4.15: Plot of ln(current) vs voltage for HgSe/p-ZnSe contacts with reverse biases of 3 to 5 volts and temperatures ranging from 291 to 348 °K.

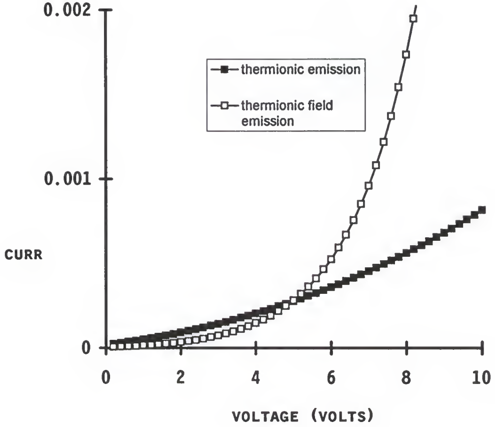

Figure 4.16: Theoretical thermionic emission and thermionic field emission I-V data for HgSe/p-ZnSe contacts. From these calculations, the crossover point between thermionic and thermionic field emission occurs at ~ 5 volts.

CHAPTER 5

DEGRADATION STUDIES OF MULTIQUANTUM WELL CONTACTS

Introduction

The electrical degradation of multiquantum well ohmic contacts to p-ZnSe are discussed in the following chapter. The contacts were degraded under high current densities (up to 1500 A/cm^2) to simulate the operating conditions which these contacts encounter when used in ZnSe based light emitting diodes and laser diodes operated in a continuous wave mode. Auger depth profiles, atomic force microscopy, energy dispersive spectroscopy of X-rays and secondary electron images were used to identify changes in structure and composition which occurred during degradation. Based on this analytical results, potential links between contact degradation and dark line defect formation in laser diodes will be discussed.

Experimental Setup

The degradation of multiquantum well contacts was performed using samples grown at 3M Corporation in St. Paul, MN. The samples consisted of 1 to 2 μm of N doped p-ZnSe grown by MBE on highly doped p-type GaAs (100) substrates. ZnTe/ZnSe multiquantum well contacts were grown on the ZnSe as described by Hiei et al. [Hie93] (Fig 2.10). The as received samples were cleaned in acetone, methanol, and deionized water prior to depositing the metallization on the multiquantum well contacts. Ohmic metallizations on the multiquantum well structure's top ZnTe layer were formed by depositing 100 Å of Pd followed by 1000 Å of Au (Fig 5.1), using the evaporator described in chapter 3. Although Hiei at. al. [Hie93] reported that a minimum R_c for the Au/Pd contacts on p-ZnTe was obtained by heat treatment at 200 °C for 3 minutes, the contacts used for this work were heat treated at 150 °C for 30 minutes. This lower temperature was used to minimize any reactions in the ZnTe/ZnSe superlattice. The 150 °C heat treatment for 30 minutes was recommended by researchers at 3M, who used a similar heat treatment for Au/Pd contacts to ZnSe based lasers.

Backside ohmic contacts were made to the GaAs by depositing 600 Å of Ti followed by 1000 Å of Au (Fig 5.1), also using the thermal evaporator described in chapter 3. Both front side and backside contacts were deposited, prior to the 30 minutes 150 °C heat treatment. Both metallizations were heat treated at the same time to minimize thermal cycling of the samples.

Once the front and backside metal contacts were deposited and heat treated, the samples were cleaved into sections with dimensions ranging from ~ 4 mm x ~4 mm to 1.5 mm x 2 mm. By cleaving the samples after deposition of metal contacts, the risk of metal depositing on the sides of the samples was eliminated. This prevented the formation of metallic conducting paths which could have short circuited the front and back sides of the samples.

Electrical degradation of the multiquantum well contacts was performed by passing high current densities (1000 to 1500 A/cm^2) through the structure, from the front side contact (held at a positive voltage) to the backside contacts (held at ground potential), as shown in figure 5.2. The electrical connection to the backside of the samples was made through a copper block which also acted as a heat sink. The copper block was ~ 2.5 cm long, 0.8 cm wide, and 0.5 cm high. Electrical connections to the front side of the samples were accomplished using three different electrical probes. The first connection used a spring loaded Cu probe with an Au tip, mechanically held in physical contact with the front side of the contact. The contact area of this probe was estimated to be ~ 6x10^{-4} cm^2 and was determined from SEM images of the samples surface after degradation. This average value of contact area was used to determine the current densities during operation. Note that the area of the sample was much larger (typically 4x10^{-2} cm^2) leading to current densities through the MQW region which were orders of magnitude lower than those through the point of contact by the electrical probe. The second scheme was similar to the first, but the probe was composed entirely of Cu. The Cu probe alloyed with the Au/Pd and introduced impurities into the contact structure which were used to identify diffusion paths. These contacts had a similar contact area as the Au probe and were also held in place by spring loading. A third contact scheme used in this study consisted of a copper lead which was fixed to the surface of the sample using conducting silver paint. These contacts had a surface area of ~ $3x10^{-2}$ cm^2.

The electrical degradation stage described above was mounted on the end of a cold finger (APD model DISPLEX DE-202) which was used to control the temperature of the samples during degradation. The ADP cold finger cryostat was also used for temperature dependant I-V measurements of HgSe contacts described in chapter 4. The semiconductor temperature sensor for the cold finger was mounted in the bottom of the Cu heat sink, allowing the temperature of the heat sink to be monitored during degradation. Additional temperature measurements were made using a type-K (alumel-chromel) thermocouple which was mounted on the end of the Cu probe. The thermocouple was used to measure the localized temperature directly beneath the electrical probe.

An automated setup was used to maintain a constant current density through the contacts during degradation controlled by an IBM PC with IEEE-488 communications. The PC ramped the voltage supplied to the sample by a Hewlett-Packard 6112A DC power supply, and the current flowing through the sample was measured using a Hewlett-Packard 3478A multimeter. The current measured by this multimeter was used to control a feedback loop (through the IBM PC) which adjusted the input voltage, as required, to maintain the desired current densities. The current, voltage, and heat sink temperature were recorded throughout the degradation. Some samples were degraded with a thermocouple attached, and this temperature was also periodically recorded during degradation.

Samples ~2mm x 2mm were degraded for 15 minutes at a constant current of 0.9 A supplied by the Au probe. The resulting current density was ~1500 A/cm^2. The power supply voltages were between 3 to 5 volts yielding an input power of 2.5 to 4.5 watts. The temperature during degradation was limited to a maximum of 110 °C (383 °K) by the cold finger. The temperature was controlled using the cold finger so that additional samples could be degraded under identical conditions. Auger depth profiles were performed using a Perkin-Elmer PHI 660 Auger spectrometer with a 5 KeV, 20 nA electron beam. Sputtering for the depth profile was performed using the standard 3 KeV Ar^+ ion beam with a 3mm x 3mm raster, which would result in a sputter rate of 100Å/min. on Ta_2O_5. Auger depth profiles were collected from three points on this sample, one at the edge of the Au probe's point of contact, one at a point 10 µm away (outside the point of contact), and another at a point 20 µm away from the point of contact (also outside the point of contact).

A second set of 2 mm x 2 mm samples were degraded at current densities of ~1500 A/cm^2 for times of 6 to 90 minutes using the copper probe. As before, the cold finger was set to maintain a maximum temperature of 110 °C during degradation. An additional sample was degraded for 90 minutes at ~1000 A/cm^2 and a temperature of 14 °C to study the effect(s) of temperature on electrical degradation.

Auger depth profiles, using the same spectrometer and conditions above, were also collected from the samples degraded using the Cu probe. To improve the depth resolution, these sputter profile data were collected with a 1.5 keV Ar^+ ion beam with a raster size of 5mm x 5mm. These ion beam conditions yielded a sputter rate of ~80 Å/min on ZnSe. The depth profiles were performed on a flat surface region, ~ 10 µm outside the point where the Cu probe contacted the sample surface. A depth profile was also obtained from a non-degraded sample for comparison. Note that this non-degraded sample received the same 30 minute heat treatment at 150 °C used for the metal contacts.

Atomic force microscopy (AFM) and secondary electron microscopy (SEM) were used to identify changes in surface morphology on samples degraded at 1500 A/cm^2 for 15 minutes. The AFM was performed in tapping mode using a Digital Instruments Nanoscope III and the SEM was performed using either the PHI 660 Auger spectrometer or a JEOL JSM 35C scanning electron microscope. Compositional and structural data were also obtained using focused ion beam (FIB) milling to prepare a cross section of a sample degraded for 15 minutes at 110 °C. The FIB samples were prepared using an FEI 611 focused ion beam system. These samples were analyzed using the energy dispersive spectroscopy of florescent x-rays (EDS) on the SEM or JEOL 4000FX high resolution transmission electron microscope.

An additional sample was degraded using the silver paint contacts at current densities of 40 A/cm^2 for 12 hours at a temperature of 110 °C. This sample had the same input power as those degraded using the Au and Cu probes (~2.5 watts), but the localized current densities were reduced due to the larger area of the silver paint contacts. Following degradation, the silver paint was removed using acetone, followed by a rinse in methanol and DI water. Auger depth profiles were performed through the region originally covered by the silver paint contacts using the same parameters as for samples degraded using the Au probe.

To isolate the effects of high temperature without current, multiquantum well contacts were heat treated at elevated temperatures. These samples structures were similar to the electrically degraded samples (Fig 5.1), but with a thinner Au layer (300 Å) to improve sputter depth resolution. These samples were also heat treated at 150 °C for 30 minutes, as for the electrically degraded samples, and were then given additional heat treatments at 200, 300, and 400 °C for 60 minutes. A second 400 °C sample was studied after a heat treatment time of only 5 minutes. This sample was used to observe the initial reactions resulting from the heat treatment of the multiquantum well contacts at 400 °C. Auger depth profiles were collected from these samples using the same instrument and parameters as with sampled degraded using the gold probe.

Results

Electrical Degradation

The current, voltage, and heat sink temperature for a typical sample degraded for 12, 24, 36, and 96 minutes at ~1500 A/cm^2 are shown in figure 5.3. The degradation was momentarily stopped after each interval (e.g. 12, 24, etc. minutes) so that the I-V data could be collected. As a result, the semiconductor heat sink temperature in figure 5.3 was observed to drop after each degradation interval. These data show that the temperature increased for ~ 10 minutes before reaching a maximum value and stabilizing. This test behavior was typical for all the degraded samples. The temperatures measured using the thermocouple were typically found to reach a maximum temperature ~150 °C higher than those measured by the heat sink semiconductor. During the initial stages of degradation, localized temperatures measured by the thermocouple were found to increase significantly faster than the heat sink leading to temperature gradients >200 °C.

The I-V data as deposited and after 12, 24, 36, and 96 minutes are shown in figure 5.4. The samples exhibit non-linear I-V characteristics due to the valance band discontinuity across the p-GaAs/p-ZnSe interface. The initial I-V characteristics for all the samples were similar and rectifying. However the I-V characteristics for the degraded contacts varied widely, from no electrical conduction to linear I-V characteristics. The data in figure 5.4 show that the characteristics of this contact remained constant throughout the 96 minutes degradation at 1500 A/cm^2 using a Cu probe.

Optical and electron microscopy reveal that the high current degradation resulted in a severely damaged region directly beneath the point of contact for the Au or Cu probes (Fig 5.5). This region directly under the contact will be referred to as region I. For samples degraded using the Cu probe, region II formed around region I and was filled with micrometer sized surface defects resembling blisters. These blistered regions (region II) were not observed for samples degraded using the Au probe. Outside region II was region III, a relatively flat surface similar at low magnification to the original non-degraded surface. For samples degraded 15 minutes or longer, high magnification inspection of region III revealed that raised rectangular features ~2 to 4 μm in length were formed. Note that these features were observed for samples degraded with both Au and Cu probes. The photograph in figure 5.6 shows regions I, II, and III. The point of contact (region I) is in the lower right hand corner, which is surrounded by a ring of blisters (region II). Several raised rectangular features (region III) are faintly visible in figure 5.6, but are presented in better detail below. Outside of region III is the smooth original surface.

Au Probe

As mentioned above, samples degraded using the gold probe formed rectangular raised features, but a much less pronounced blistered region as compared to those degraded with a copper probe. Depth profiles through a sample degraded for 20 minutes at 1500 A/cm^2 and 110 °C were collected at four points. The first point was ~ 20 μm outside the edge of the point of contact (i.e. in region III); the second profile was ~10 μm in region III and taken through a flat region; the third was also 10 μm into region III, but collected at a rectangular feature; the fourth point was directly on the edge of the point of contact (i.e. in region I). The profile from the first point (20 μm into region III) is shown in figure 5.7. A small Pd signal was observed throughout the Au layer indicating that the Pd had alloyed with the Au. After ~300 seconds of sputter time, a sharp Pd peak was observed at the Au/ZnTe interface which corresponded to the 100 Å Pd layer. Some Zn and Te were observed on the surface of the sample, but little or no Zn, Se, or Te were observed throughout the Au layer. Just beyond the Pd peak at ~300 sec., a sharp Te signal was observed and the Zn signal increased. This region corresponds to the ZnTe layer. Next, the Pd and Te signals decreased as the Zn and Se signals rose to a constant level, indicating that the ZnSe layer had been reached. Note that the quantum well structure cannot be resolved in this profile.

Both profiles at a distance of 10 µm into region II, point 2 through the flat surface (fig. 5.8) and point 3 through the rectangular features (not shown), were identical. The primary electron beam was defocused to prevent melting of the sample during the depth profiles. As a result, the beam's spot size was large and the profile showed the average structure and composition across the sample surface. Therefore, the two depth profiles from the flat region and raised rectangular region were identical, and no compositional or structural changes were identified in the raised rectangular regions. Both profiles showed a decrease in the Pd peak between the Au and ZnTe layers, indicating additional Pd has alloyed with the Au as compared to point 1 (20 µm distance). Some diffusion of Au into the ZnTe region was observed from the data taken at points 2 and 3 (Fig. 5.8), as indicated by the tail on the Au signal extending into the ZnTe region. Data from point 4 at the edge of the contacts (Fig 5.9) indicated that all of the Pd in this region had alloyed with the Au. In addition, a more diffuse interface was observed between the Au and ZnTe, with the Au profile extending into the ZnSe region.

Cu Probe

The Auger depth profiles for the non-degraded sample, and after 6 and 90 minutes of degradation at 1500 A/cm^2 at 110 °C using a copper probe, are shown in figure 5.10 through 5.14. As indicated in the experimental section, Auger depth profiles were performed on all samples in the flat region (region III), outside the point of contacts. Unless otherwise stated, all profiles were taken through undefective regions.

In the depth profile from the non-degraded sample (Fig. 5.10), some Pd had alloyed with the Au but the majority resided in a Pd layer at the Au/ZnTe interface. Note that a small C signal was observed at the Pd/ZnTe interface. Despite cleaning efforts, this C resulted from contamination prior to (or during) the deposition of the metal overlayers. After sputtering through the Pd at ~3000 sec., the Zn signal rose along with a sharp Te peak. This region corresponded to the ZnTe top layer. At the right side of the Te peak (~4500 sec.), the Se signal also increased and the Te signal dropped off as the depth profile reached the ZnTe/ZnSe superlattice. Note that the quantum wells again were not resolved. The Zn and Se signals reached constant values between 6000 sec. and 16000 sec. of sputter time, indicating a uniform stoichiometry throughout the ZnSe region. The ZnSe/GaAs interface was reached after 16000 sec.

After 6 minutes of degradation time, significant changes were observed in the sample structures, as indicated by Auger analysis. First, a large surface concentration of Zn was detected and removed by a 30 sec. sputter prior to collecting the depth profile of figure 5.11. The depth profile also showed that additional alloying occurred between the Pd and Au, as evident by the larger Pd signal throughout the Au layer, and the lower Pd peak at the Au/ZnTe interface (compare Figs. 5.10 and 5.11). In addition to Pd, Te, Zn and Se were observed to diffuse into the Au layer. Similar to the non-degraded sample, the Zn and Se signals were relatively constant throughout the ZnSe region, and the ZnSe/GaAs interface was again reached after ~3000 sec. of sputter time.

The blistered region surrounding the point of contact was observed to form very rapidly and was evident on all samples degraded using the Cu probe, including the one degraded for only 6 minutes. Therefore, a second depth profile (fig 5.12) was collected from the 6 minute sample through one of the blistered regions (region II). The profile shows that Cu, from the Cu probe, alloyed with the Au layer. Unlike region III, Te, Zn, and Se did not diffuse into the Au layer. Instead, Cu diffused through the Au/Pd region and collected at the Pd/ZnTe interface. The Cu signal intensity dropped below detectable limits once the Pd/ZnTe interface was reached. The Cu signal was again observed to increase upon reaching the ZnSe/GaAs interface. Clearly, Cu has permeated through the ZnSe layer and into the GaAs. These results were confirmed by the cross sectional FIB sample which will be discussed below. As for the non-blistered area, a surface concentration of Zn was detected but, was removed by a 30 second sputter cleaning prior to depth profiling.

Auger electron data from samples degraded for 90 minutes again had a surface coverage of Zn which was removed by a 30 second sputter cleaning. The depth profile (Fig 5.13) showed that the majority of the Pd alloyed with the Au. The Te peak was broader and had a lower intensity, indicating the possibility of diffusion of Te into ZnSe, or more likely, roughening of the Pd/ZnTe and the ZnSe/ZnTe interfaces. Although small signals were observed for Zn, Te, and Se through the Au/Pd layer, the signal intensities were lower than in the 6 minute sample profiles (Figs. 5.11 and 5.12). Importantly, the Zn and Se signals were no longer constant throughout the ZnSe region. Instead, the Zn signal was lower in the top half of the ZnSe, indicating a substantial loss of Zn from this region. The As signal was also found to be detectable long before the ZnSe/GaAs interface was reached at 18500 sec., indicating that small amounts of As had diffused into ZnSe. Small amounts of Cu were alloyed with the Au layer, but the Cu signal dropped to undetectable limits after 10,000 sec. of sputtering into the ZnSe layer. The Cu signals were not detectable in the GaAs region, indicating that no Cu permeated through to this region. This is in contrast to the blistered regions in the 6 min. sample, as discussed above.

The Auger depth profile from the sample cooled to 14 °C during degraded for 90 minutes at 1000 A/cm^2 using the Cu probe is shown in figure 5.14. This depth profile is similar to the depth profile from a non-degraded sample with one exception. The Pd peak is lower due to the faster sputter rate used during this depth profile. Despite the lower signal intensity, the Pd peak is sharp, and the ZnTe and ZnSe regions are well defined. This indicates that little diffusion took place during the degradation of the samples at low temperature and low current density. In addition, no Zn was found on the surface of this sample, unlike other samples degraded at higher temperatures and current densities (1500 A/cm^2 at 110 °C).

To identify the events leading to the formation of the blistered region surrounding the Cu probe's point of contact, a cross sectional sample was prepared by focused ion beam (FIB) milling. This sample was originally intended to be used for TEM, but was too thick to obtain high resolution images in the JEOL 4000 FX. However, the sample was transparent enough to resolve the layered structure, allowing the collection of EDS data which were correlated with the SEM micrographs shown in Figures 5.15 and 5.16. Figure 5.15 is a high magnification image of the cross section showing the multilayer structure and figure 5.16 is a lower magnification image of the same sample. The composition of each layer, as identified by EDS (Figs. 5.17-5.23), have been indicated in this figure. The top layer was tungsten (W), which was deposited to preserve the underlying structure during the FIB milling of the sample. The next layer, which was the original sample surface during degradation, was a thin Zn rich layer, probably composed of ZnO. The Au/Pd layer lies beneath the ZnO, followed by a region containing Zn, Te and Se (i.e. the MQW region). Notice that Cu was identified in the ZnO, Au/Pd and Zn/Te/Se regions. The next layer consisted of Zn and Se, and corresponds to the ZnSe epitaxial layer. The EDS data in figure 5.21 indicates that very little Cu was present in this region. The next layer, which appeared to be polycrystalline with many voids and defects, was composed of Cu with Ga and As. Beneath this layer was the GaAs substrate. Note that in figure 5.16, the surface topography of the blister was found to follow the varying thickness of the underlying Cu region between the ZnSe and GaAs.

To help identify the origin of the raised rectangle features observed on the surface of the degraded samples, the surface morphology of the features was studied using SEM and AFM. An SEM micrograph from a sample degraded for 90 minutes at 1500 A/cm^2 and 110 °C, used for Auger depth profiles above in figure 5.13 and 5.14, is shown in figure 5.24. This micrograph shows several raised rectangular features which have formed in region II, ~10 μm from the outer edge of the Cu probes point of contact (region I). Figure 5.25 is an AFM image of a sample degraded for 20 minutes at 1500 A/cm^2 and 110 °C u sing the Cu probe. The image was taken just outside the blistered region surrounding the Cu probe's point of contact, with the point of contact being oriented off the top of the picture. The AFM analysis indicated that the rectangular features have an average height of ~50 nm, were 2 to 5 μm long and nearly square, and that the larger and taller features were located closer to region I. The height and density of the features decreased as the distance from region I increased. This indicates that the features resulted from degradation. In addition, the sides of the rectangular features were aligned with the cleaved sides of the samples, which for both GaAs and ZnSe are the {011} planes.

To better observe the rectangular features, the Au/Pd contact was removed from a sample degraded for 20 minutes at ~1500 A/cm^2 and 110 °C using a commercial Au stripping solution called Technistrip Au and was supplied by Technic, inc. (located in Cranston, RI). Upon removal of the Au/Pd layer, cracks were observed along the edge of the rectangular features. Based on the crystallographic orientations reported above, the cracks ran parallel to the <100> directions. Figure 5.26 is an AFM image showing a raised rectangular feature accompanied by a crack. Figure 5.27 is an SEM micrograph of a larger area showing the same feature (rotated ~90° clockwise), plus other micro-cracks. Numerous small cracks were observed in the surrounding area, all of which had orientations parallel to or perpendicular to the bigger cracks. Figure 5.28 is a micrograph showing double rectangular features forming on either side of the cracks, and the cracks propagate along the <110> directions at the end of the rectangular defects. In all cases, the depths of the cracks were too great to measure by AFM.

To ensure that the cracks were not generated by etching of the ZnTe and ZnSe during the chemical stripping of the Au film, identical samples were ion milled using a 5 keV, 30 nA, Cs^+ beam in a PHI 6600 SIMS instrument. Sputter removal of the Au layer also revealed identical cracks adjacent to the raised rectangular features, as observed by wet chemical removal of the Au layer. Additional sputtering revealed that these cracks extended through the entire ZnSe region and into the GaAs substrate.

Silver Paint Electrical Probes

The Auger sputter depth profile from a sample degraded using large area silver paint contacts (Fig 5.29) indicated a different structure than that observed for the contacts degraded using Cu or Au probes. This sample was degraded for 12 hours at a current density of 40 A/cm^2, reaching a maximum temperature of 110 °C. Following degradation, the silver epoxy was removed by cleaning in acetone, methanol, and deionized water. Again Zn and Te were found on the surface of the sample, but aside form a reddish discoloration of the Au metallization under the silver contact, no changes in the contact surface were observed. The depth profile (Fig 5.29) indicated the formation of a Pd/Zn/Te compound and a low Te signal, which suggests a loss of Te. Note that the stoichiometry of the ZnSe is constant throughout the profile.

Heat Treated Samples

The depth profiles for samples heat treated at 200 °C for 60 minutes are shown in figure 5.30. These data indicate some alloying of Pd with the Au layer, but a large amount of Pd was still present between the Au and ZnTe. The data also indicate that a Pd/Zn/Te compound may have formed between the Pd and ZnTe layers. No Zn was found on the surface of the sample, but C contamination was observed at the Pd/ZnTe interface.

For the samples heat treated at 300 °C, the formation of a Pd/Zn/Te compound was more pronounced (fig 5.31). A sharp Pd signal was observed between the Au and ZnTe with both the Zn and Te signals exhibiting a plateau region through the Pd layer. Again, no Zn was found on the surface, the ZnSe stoichiometry was maintained, and C contamination was observed at the Pd/ZnTe interface.

For 5 minutes at 400 °C, the depth profile revealed Zn and Se on the surface of the sample (Fig 5.32). Although significant alloying of the Au and Pd was observed, enough Pd remains between the Au and ZnTe layers to suggest the maintenance of a Pd/Zn/Te compound. Despite the evidence of Zn diffusion to the sample surface, the stoichiometry of the ZnSe was constant. After 60 minutes at 400 °C, the surface of the sample was covered with a ZnO layer (Fig 5.33). Note that significant amounts of Te were also found on the surface and throughout the ZnO layer. The Au and Pd were completely alloyed, and no distinct ZnTe layer remained. As the ZnSe was reached, the slope of the Se signal was greater than the Zn signal, indicating a loss of Zn from this region.

Post Degradation Surface Reactions

Following degradation by high current or heat treatment, all samples were placed in a desiccated chamber for storage. However, the surface morphology was found to change with time. Whisker-like features formed on the samples surfaces which grew into randomly oriented rectangular crystals over a period of several weeks to several months. A micrograph of features which formed after ~3 week is shown in figure 5.34, and after 3 months in figure 5.35. An Auger line-scan over these features (Fig. 5.36) indicates they are composed Zn, C, and

O and are believed to be $ZnCO_3$. The $ZnCO_3$ was found to form on all degraded samples except electrically degraded sample held at 14 °C. For samples degraded by heat treatment at 200 and 300 °C, the $ZnCO_3$ formed only on the sample edges.

Discussion

Diffusion of Zn and Te

The goals of this research were to identify compositional and structural changes which occur during electrical degradation of multiquantum well contacts, and to determine if there was any link between contact failure and the formation of dark line defects (DLDs). These goals were achieved through the analysis of the experimental data based on the following arguments. A damaged region beneath both the Cu and Au probes point of contact (region I) were commonly observed after power was supplied through a point contact. This damage presumably resulted from localized high current densities which led to localized heating of the underlying semiconductor. The localized heating resulted in accelerated diffusional processes and thermal stresses which led to failure of the contact structure.

The fact that localized heating occurred as a result of the high current densities was evident based on the Auger data from samples degraded using the Au probe. The depth profiles at three different locations from the probes point of contact, (data from 20 μm and 10 μm outside and at the edge of the point of contact, Figs. 5.7 - Fig. 5.9, respectively) show that alloying between Pd with Au and interdiffusion of species progressed more rapidly closer to the point of contact (region I). Since alloying and diffusion are exponentially dependent on temperatures, these results strongly suggest that localized temperature were significantly greater at locations closer to the point of contact.

Degradation of the ZnTe/ZnSe multiquantum well contacts, caused by the localized heating, was found to progress as follows based on Auger depth profiles from the non-degraded sample (Fig 5.10) and the samples degraded using the Cu probe at ~1500 A/cm^2 for 6 min. (Fig 5.11), and 90 min. (Fig. 5.13). After 6 minutes, Zn and Te, from the ZnTe layer, and possibly some Se from the superlattice and/or ZnSe layer diffused through the Au/Pd contact. At the same time, Pd alloyed with Au. After 90 minutes, the Pd was observed to have completely alloyed with the Au and long range disruption of the ZnSe stoichiometry resulted from Zn diffusing out of the ZnSe region to the surface of the sample. Note that a localized maximum in the Te profile occurred in the Au layer after 6 minutes with the Cu probe (fig. 5.11). This indicates that a large amount of Te initially diffuses into the Au region towards the sample surface, but the Te flux decreased during subsequent degradation. Note also that after 90 minutes, long range diffusion of Zn out of the ZnSe region was observed, but an overlying Te layer was still present. The remaining Te signal is believed to come from the ZnTe/ZnSe superlattice, suggesting that the ZnTe overlayer dissociated and diffused into the Au layer, but the superlattice did not. Therefore, Zn lost from the underlying ZnSe must have diffused through the remaining ZnTe/ZnSe superlattice. While the data discussed above was obtained for samples degraded using a Cu probe, similar diffusion and alloying were observed in contacts degraded using an Au probe. Therefore, the diffusion of Zn and Te as well as the alloying of Pd and Au occurred independent of the electrical probe's composition.

Thermal Stress

In addition to accelerating diffusion, localized heating from the high current densities during degradation are believed to have generated significant thermal stresses which lead to the formation of the micro-cracks observed on the degraded contacts (Figs. 5.26 - 5.28). Again, these cracks were observed on samples degraded using both Au and Cu electrical probes. If the area under the electrical probe (region I), is treated as rigidly bound, the magnitude of the thermal stress (σ_t) within the contact's locally heated region can be calculated as follows [Ask94]:

$$\sigma_t = \alpha E \Delta T, \qquad (5\text{-}1)$$

where α is the coefficient of thermal expansion, E is Young's modulus, and ΔT is the difference in temperature. Since the mechanical properties of ZnSe have not been studied in as great detail as for GaAs, the calculations below will be performed for the thermal stresses in the GaAs substrate as opposed to the ZnSe epitaxial layer. Thermal stresses sufficient to form micro-cracks in the GaAs are assumed to be sufficient to form cracks in the ZnSe. This is a reasonable assumption since both ZnSe and GaAs cleave along the {011} planes and any cracks originating in the GaAs would be expected to propagate into the ZnSe as described by Griffith's theory of brittle fracture [Die86, p. 246]. The value of σ_t is easily calculated for GaAs using values 5.4×10^{-6} K^{-1} for α [Lid95, p. 12-97], 103 GPa for E [Eri88] , and a ΔT of 200 °C from the results section. Defining the y and z directions in the plane of the sample and the x direction normal to sample surface, the calculated values for σ_t in the y (σ_{ty}) and z (σ_{tz}) directions are both a compressive stress of 111 MPa.

Treating the sample as an elastic solid, the biaxial thermal stress in the y and z directions distort the crystal structure. Compressive stress would decrease the crystal dimensions in the y and z directions, but elongate them in the x direction. This will generate a tensile strain in the x direction. The magnitude of this strain can be calculated using the following equation [Die86, p. 49]:

$$\varepsilon_x = 1/E[\sigma_x - v(\sigma_y + \sigma_z)] \qquad (5\text{-}2)$$

where ε_x is the strain in the x direction, and v is Poisson's ratio. Using the y and z stresses calculated above (σ_x from thermal expansion is assumed to be negligible since expansion can freely occur in this direction), and 0.24 for v [Eri88], the tensile strain in the x direction is $\varepsilon_x = 5.17\text{x}10^{-4}$. Using Hooke's law, ($\sigma$=E$\varepsilon$), the equivalent tensile stress in the x direction required generate the same strain as the biaxial y and z stresses would be 53 MPa. Analysis of GaAs indicates that the material always cleaves along the {110} planes. The fracture stress for GaAs, reported from four point bending measurements, was between 60 to 75 MPa [Bel94]. In this work, the fracture was believed to initiate at pre-existing surface defects on the GaAs generated by normal handling. In other work, fracture stresses of 55 to 80 MPA were observed for GaAs which was precracked by indentation [Yas88]. This indicates that the thermal stress of 53 MPA generated in the MQW contacts during degradation, had sufficient magnitude to cause crack propagation.

This mechanism explains why the micro-cracks intersect the sample surface along the <100> directions. As calculated above, a tensile stress of 53 MPA in the x direction will cause the same strain as biaxial compressive stresses of 111 MPA in the y and z direction. Therefore, the following arguments will treat the samples as if they were under tensile stress in the x direction. Since the GaAs substrate was cut with a (100) surface, the cleavage planes which are at a 45° angle to the (100) surface, such as the (101), intersect the sample surface along the <100> directions (Fig. 5.37a). Due to their 45° orientation to the sample surface, these planes would have a component of tensile stress due to σ_x calculated above. However, the cleavage planes normal to the sample surface, such as the (011) which intersect the sample surface along the <110> direction, are not under tensile stress (Fig. 5.37b). Cracks will propagate along the planes under tensile stress, and therefore will propagate along the {110} planes, intersecting the surface along the <100> directions.

It is possible that the cracks originated at defects on the surface of the GaAs, but another potential location for cracks to originate was along stacking faults at the ZnSe/GaAs interface. This may explain why the cracks in figures 5.26 through 5.28 appear to have kinks, as opposed to being perfectly linear. Stacking faults in ZnSe typically form along the {111} planes and therefore, cracks initiated along stacking faults would initially lie in the {111} planes. As the cracks enlarged, they would tend toward the lower energy {110} cleavage planes. Multiple cracks would then produce a jagged crack with a net displacement along the {110} planes.

Stress generated from the thermal expansion mismatch between GaAs and ZnSe should have been significantly less than the thermal stresses calculated above. This is partly due to the small difference in thermal expansion for GaAs (5.4×10^{-6} K^{-1}) and ZnSe (7.2×10^{-6} K^{-1}). In addition, the samples were grown at ~280 °C, so the stress due to the thermal mismatch should be zero at this temperature. The sample temperatures were measured to be 260 °C, using the thermocouple, yielding a ΔT of only 20 °C. Results from the samples degraded by high temperature heat treatment, which will be discussed in more detail later, indicate that sample temperatures may have been as high as 300 to 400 °C. At these higher temperatures, the larger thermal expansion of ZnSe, as compared to GaAs, would lead to additional compressive stress in the ZnSe. This suggests that the micro-cracks would originate in the ZnSe instead of the GaAs. Other evidence indicating that the micro-cracks for in the ZnSe are that lattice parameter for ZnSe (5.6676 Å) is greater than the lattice parameter for GaAs (5.6531 Å). This results in additional compressive stress in the ZnSe region due to the lattice mismatch, leading to micro-cracks originating in the ZnSe region.

Impurity Diffusion and Blisters in Region II

While diffusion of Zn and Te, as well as the formation of micro-cracks were observed for samples degraded using both Au and Ag contacts, the evolution of raised blisters (in region II) was only observed for contacts degraded using Cu probes. The mechanisms leading to the formation of the raised blisters be explained by considering diffusion of solute atoms (Cu) into the MQW structures, which have numerous micro-cracks throughout them. From the SEM micrograph of the FIB cross sectional sample (Fig. 5.16), the surface topography of the blistered region was found to follow the geometry of the underlying Cu rich region. Both Auger depth profiles and EDS data from the FIB cross section confirm large amounts of Cu at the ZnSe/GaAs interface but little to no Cu in the ZnSe region. Due to the small cross sectional area of the micro-cracks relative to the volume of the bulk crystal, Cu diffusing through ZnSe along micro-crack surfaces would not be detectable by Auger or EDS. However, the cracks should provide a high diffusivity path for Cu through the ZnSe, as shown schematically in figure 5.38. The Cu would diffuse down to and along the ZnSe/GaAs interface, deforming the overlying layers and resulting in the blistered regions. Despite the fact that a crack was not observed in the cross section of figure 5.15, micro cracks repeatedly formed in this region (region II) on all degraded samples studied.

The mechanisms outlined above would require a rapid diffusion rate for Cu along the GaAs/ZnSe interface since the cross sectional sample (Fig. 5.16) showed a ~1 μm thick Cu layer at the ZnSe/GaAs interface which formed after 20 minutes of degradation. A 1 μm thick , 10 μm diameter Cu region at the ZnSe/GaAs interface would consist of ~ $8x10^{12}$ atoms. The number of atoms which could be transported through the micro-cracks observed on the degraded samples can be estimated as follows. The frequency factor (D_o) and activation energy (Q) for Cu bulk diffusion in ZnSe are $1.7x10^{-5}$ cm^2/s and 0.56 eV, respectively [Lid95, p. 12-110]. Since the activation energy for surface diffusion is typically ~1/3 that of bulk diffusion, the activation energy for Cu diffusion along the surface of the micro-crack walls would be ~0.18 eV. The diffusion coefficient (D) is calculated as shown below:

$$D = D_o \exp(-Q/RT) \qquad (5\text{-}3)$$

where R is the gas constant and T is the temperature. Equation 5-3 yields a diffusion coefficient of 3.3×10^{-7} cm^2/s at a temperature of 260 °C (the localized temperature measured by the thermocouple), assuming the same D_o as above, which can be used to calculate the flux rate of Cu through the micro-cracks using Fick's first law:

$$J = -D\,(\partial c/\partial x). \qquad (5\text{-}4)$$

Here $\partial c/\partial x$ is the partial derivative of concentration (c) with respect to distance (x), and can be approximated as $\Delta c/\Delta x$. Assuming a 50 % surface concentration of Cu and no Cu at the bottom of the micro-cracks, Δc is 5×10^{22} atoms/cm^3. Using a diffusion distance of 3 µm (the thickness of the MQW contacts and ZnSe epitaxial layer) for Δx, J is calculated to be 5.5×10^{19} atoms/cm^2 s. Using an area of 2×10^{-11} cm^2 (assuming a crack length of 5 µm and each side of the crack to be one interatomic spacing wide), 1.2×10^{12} atoms could diffuse down the micro-crack in 20 minutes. This is in reasonable agreement with the number of atoms indicated above, required to form the blistered regions. Diffusion along the ZnSe/GaAs should occur almost as rapidly as along the crack surfaces since the activation energy for interfacial diffusion is ~1/2 that of bulk diffusion. Therefore, Cu does have sufficient mobility to diffuse down the micro-cracks and along the ZnSe/GaAs interface to generate the blistered regions after 20 minutes.

Rectangular Raised Features in Region III

Now considering the rectangular features which formed in region III of the degraded contacts, their shape and orientation to the underlying semiconductor suggest at least two possible mechanisms of formation. First, the rectangular features resemble the dislocation patches (DLDs) which form in the quantum well region of degraded diode lasers. The second possibility discussed below consists of diffusion of Zn and Te from the ZnTe layer to the Au layer by a ledge mechanism. Note that Auger depth profiles through the raised rectangular features showed no evidence of Au or Cu diffusion, indicating that the rectangular features did not result form impurity diffusion into the MQW contact structure.

Due to the similarities between the rectangular features and DLDs, a review of DLD formation is in order. The formation of DLDs begins with dislocations that originate at stacking faults at or near the GaAs/ZnSe interface and propagate up through the n-ZnMgSSe (Fig 2.11) [Hua94]. At the n-ZnMgSSe/n-ZnSSe interface, the partial dislocations bounding the stacking faults combine to form narrowly dissociated dislocations which thread upwards. Upon reaching the quantum well, the dislocations dissociate forming small stacking faults. Beyond this point, the dislocation reaction has not been studied in detail, but preliminary results indicate that a dislocation half loop forms at the p-ZnMgSSe/p-ZnSSe interface which threads upward to the sample surface. TEM results indicate that the dislocation networks which form in the quantum well region (DLDs) result from a coalescence of point defects [Hov95]. It has been further suggested that the point defects are vacancies which aid in the relief of compressive strain in the QW region and that the threading dislocations which intersect the QW are paths for accelerated diffusion of these point defects.

In work by Hovinen [Hov95], dark line defects were generated by optical pumping of the laser structures as well as by electrical pumping. This result along with the confinement of the defects to the quantum well region indicates that the formation of DLDs is enhanced by recombination-induced heating [Yas94] at the p-n junction during current injection. Recombination-induced heating results from energy absorbed by the semiconductor when a non-radiative recombination occurs (~2.7 eV for ZnSe). This often leads to generation and enhanced diffusion of point defects [Yas94] and is believed to accelerate point defect diffusion in ZnSe laser diodes resulting in the formation of DLDs.

Although the structures studied in the present study were not QW lasers, the contact structure had a strained ZnSe/ZnTe multiquantum well, in which patches of dislocation may also have formed. The rectangular defects observed in region III of the degraded contacts have rectangular geometries oriented about micro-cracks, similar to the DLDs oriented about threading dislocations. The quantum well contacts are highly strained which suggests that point defects form to reduce strain, also similar to the DLDs. Finally, the micro-cracks have been indicated above as paths for accelerated diffusion, and would therefore assist the formation of dislocation patches in the QW contacts by providing a path for accelerated diffusion of point defects.

A reduction of the density of the ZnTe/ZnSe quantum well, due to dislocation formation, would account for a volumetric expansion leading to the formation of raised features. However, the MQW region of the contacts was initially only ~200 Å, while the rectangular defects were found to be as high as 1000 Å, and would therefore require a 500% increase in volume to account for the observed raised rectangular features. In addition, the DLDs in the laser structures are bounded in the <340> directions, while the rectangular features in the degraded contact structures were bounded in the <110> directions. As a result, it is not certain that patches of dislocation networks alone would lead to the formation of the raised features.

Auger depth profiles discussed above showed that the Zn and Te from the ZnTe layer diffused through the Au layer to the sample surface. Since little Au was found to diffuse in the opposite direction, the interface between the metallization and the ZnTe migrated into the sample structure as described by the Kirkendal effect. However, once the ZnTe/ZnSe superlattice was reached, the superlattice did not dissociate and diffuse into the metallization, impeding further movement of the interface. Therefore, Zn lost from the ZnSe epitaxial layer must have diffused through the superlattice. If patches of dislocations had formed in the superlattice, a much higher atomic flux would diffuse across these regions due to pipe diffusion along the dislocations. The excess material diffusing from the ZnSe to the sample surface in these regions may have slowed the migration of the metal/semiconductor interface in the localized regions, leading to the formation of the raised rectangular features.

With respect to the second mechanism, dissolution of the semiconductor surface into the metallization, through a ledge mechanism is possible. Growth ledges commonly form when growth (or recession) of an interface is interface-controlled [Por81] as opposed to diffusion-controlled. Interface-controlled growth/dissolution commonly occurs across smooth solid/liquid interfaces or coherent (and coherent regions of semicoherent) interfaces, especially when the interface occurs between phases with different crystal structures. These interfaces have a low accommodation factor for atoms diffusing across the interface because the diffusing atom must occupy an unstable, high energy position. Therefore, atoms which jump across the interface are forced back to their original, more stable, positions. Diffusion across these interfaces occurs by the transverse motion of ledges which are typically hundreds of atom layers high (fig. 5.39a). Atoms hopping across the interface to the ledge faces BC and DE are easily accommodated since no new surfaces are generated. As atoms jump to (or from) the ledge faces, the ledges grow (or recede) parallel to the interface, resulting in the structure shown schematically in figure 5.39b. Growth mechanisms which rely on this ledge mechanism are commonly limited by the nucleation rate of new ledges. However, when surfaces recede through a ledge mechanism, the sample edged act as a continuous source for new ledges.

The interface between ZnTe and the Au/Pd metallization is not believed to be coherent, but the MBE-grown ZnTe does have a smooth, single crystal surface. Therefore, atoms randomly diffusing across the metal/semiconductor interface will generate greater surface area, increasing the interfacial energy. To minimize the interfacial energy, diffusion may be occurring through a ledge assisted process. The rectangular features observed on the degraded samples would then result from the impeded lateral movement of ledges as the semiconductor surface dissociates and Zn and Te diffuse across the metal/semiconductor interface. In order to further minimize interfacial energy, the ledges are expected to form along planes with the lowest interface energy. This is in agreement with the rectangular features observed on the degraded samples which have edges that are aligned with the {110} cleavage planes, the only non-polar surface for ZnTe.

The SEM (Fig 5.27) and AFM (Fig 5.26) images of the rectangular features indicate that the lateral motion of the ledges are impeded by the micro-cracks. It is not clear why this would occur. Instead, the cracks would be expected to act as a source for ledge nucleation, resulting in faster dissolution of the surrounding semiconductor and the formation of pits. Therefore, while this mechanism may play a role in the formation of the raised rectangular features, the formation of dislocation patches in the quantum well region appear to be the dominate mechanism.

High Temperature Effects

An important issue which must be discussed is the relation between temperature, degradation mechanisms, and degradation rate. The contact degraded for 90 minutes at 1000 A/cm^2 and 14 °C showed only minor alloying of the Au and Pd, which actually occurred earlier during the initial 30 minute heat treatment at 150 °C (see Fig 5.14) to achieve ohmic characteristics. There was no diffusion of Zn, Te, or Se to the sample surface and no loss of Zn from the ZnSe. In addition, there was no alloying of the contacts with Cu from the Cu probe. This indicates that the degradation of the contacts is strongly dependant on temperature and can be prevented by cooling the sample during operation.

During operation, degradation was observed for samples with a heat sink temperature of 110 °C. Using the thermocouple to obtain localized temperature readings, the maximum probe tip temperature measured was 260 °C, for a heat sink temperature of 110 °C. Despite the use of a thermocouple at the tip of the electrical probe, these measurements of localized temperature are believed to still be significantly lower (by an estimated 50 to 100 °C) than the actual temperatures directly beneath the probe. This observation is based, in part, on reports that ZnSe can be safely processed at temperatures up to 300 °C, yet a severe loss of Zn was observed for samples degraded at heat sink temperatures of 110 °C. Additional support for these conclusions comes from the comparison of the depth profiles form electrically degraded and heat treated samples below.

The samples degraded by heat treatment at 200 and 300 °C showed that the MQW contacts experienced only minor alloying between Au and Pd and no diffusion of Zn, Te, and Se, in contrast to the electrically degraded samples. Instead, a Pd/Zn/Te compound was observed to form at the Pd/ZnTe interfaces, similar to the Pd_5ZnSe compound reported to form at Pd/ZnSe interfaces [Dux95] heat treated between 200 and 400 °C. The Pd/Zn/Te compound was also detected after 5 minutes at 400 °C, but was not stable during longer heat treatments. After 60 minutes, the Pd/Zn/Te compound had disappeared, and the Auger depth profiles from the contacts (Fig 5.33) showed the same trends as the depth profiles from electrically degraded contacts (Fig. 5.7). Note that the Pd_5ZnSe compound was also reported to be unstable at temperatures of 400 °C and higher [Dux95]. Concentrations of Zn, Te, and Se were found at the surface, and the Pd alloyed with Au. In addition, the sample heat treated at 400 °C for 60 minutes showed a loss of Zn from the surface of the ZnSe region. The lack of a Pd/Zn/Te compound in the Auger depth profiles of the electrically degraded samples indicated that the localized temperatures must have been > 300 °C. Further, the similarities between the depth profiles from the 400 °C heat treated samples and electrically degraded samples indicated that degradation under high current loading resulted from localized temperatures close to 400 °C.

MQW Contact Degradation and DLDs

As described above, the formation of DLDs in laser diodes are believed to result from the coalescence of point defects in the QW region. Recombination induced heating was postulated as a mechanism which accelerated the formation and diffusion of these defects. The results in this dissertation show that localized heating results when power is supplied to a multiquatum well contact through a fine tip probe. Potentially, this localized heating would further increase the rate of point defect diffusion and lead to accelerated DLD formation. In addition, the localized heating in the contact structures studied in this work was believed to result in the formation of micro-cracks which extend through the structure. In a quantum well laser structure, these cracks certainly would extend through the active region of the device. Since the micro-cracks were shown to act as high diffusivity paths, the cracks would provide a path for accelerated point defect diffusion (as dislocations have been speculated to act in degraded QW lasers), again leading to accelerated DLD formation.

Effects of Contact Area

The silver paint contacts indicate that the lifetime of MQW contacts can be prolonged by increasing the contact area, while maintaining the same input power. The Auger depth profile through the contact degraded for 12 hours at 40 A/cm^2 suggest that a Pd/Zn/Te compound has formed, similar to the samples heat treated at 200 and 300 °C. This indicates that the localized temperature was significantly reduced by increasing the contact area. Despite the lower temperatures, Zn was still observed to diffuse and collect on the sample surface. The voltage and current during degradation were 3-5 volts and 0.9 A, respectively, resulting in an input power of 2.7 to 4.5 watts. No rectangular features or micro-cracks were observed on the samples surface, nor was a loss of Zn observed in the ZnSe region. This indicates that the long range diffusion of species in the ZnSe region was significantly reduced by larger contacts, presumably due to lower operating temperatures. The implications for ZnSe based diode lasers are that micro-cracking and diffusion in the MQW contact can be decreased by distributing the input current over a larger area during testing and operation.

Post Degradation Surface Reactions

Analysis of degraded samples consistently showed that Zn diffused to, and accumulated on the sample surface. Immediately after degradation, the Zn dispersed and formed an oxide on the surface. After several weeks, the oxide transformed to a carbonate, due to the much larger free energy of formation for $ZnCO_3$ (-731 Kcal/mol) as compared to ZnO (-320 Kcal/mol) [Lid93]. This larger free energy provides the driving force to produce $ZnCO_3$ from ZnO and residual CO_2 from air. The $ZnCO_3$ initially formed as whiskers which eventually grew into crystals that reached tens of micrometers in length. In addition to Zn and Te, Se also diffused to the sample surface. The lower surface concentration of this element on the degraded samples probably resulted from sublimation, since the vapor pressure of Se (2 Torr at 110 °C) is much greater than for Te (2×10^{-2} Torr) and Zn (1×10^{-2} Torr) at 110 °C. The formation of ZnO and $ZnCO_3$ may present adhesion problems for these devices, which must be considered when ZnSe devices are ready for wire bonding and packaging.

Summary

The electrical degradation of the multiquantum well contacts was found to result from localized heating and atomic transport at the electrical probe point of contact. This localized heating became more pronounced as the probe's contact area was reduced, and was found to result in micro-cracks, alloying of the Au and Pd metallizations, and diffusion of Zn, Te, and Se. The micro-cracks were identified as high diffusivity paths through the contact structure. Comparison of electrically degraded samples to those degraded by heat treatment indicated that localized temperatures during degradation by small contacts supplying ~1500 A/cm^2 using Au and Cu probes were close to 400 °C. Larger area contacts were found to reduce the localized heating and slow the degradation, however, Zn was still observed to diffuse to the sample surface. Diffusion of Zn was dsecreased by increasing the area of the contact and prevented by cooling the sample to 14 °C during degradation.

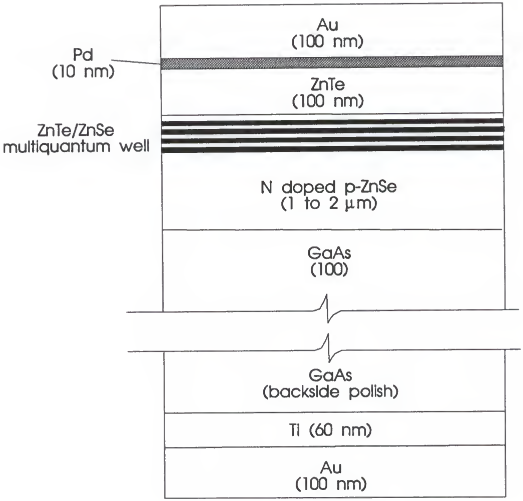

Figure 5.1: Schematic diagram showing the multiquantum well contact test structure. The frontside (Au/Pd) and backside (Ti/Au) metallizations were deposited by evaporation. Following deposition, the samples were heat treated for 30 minutes at 150 °C.

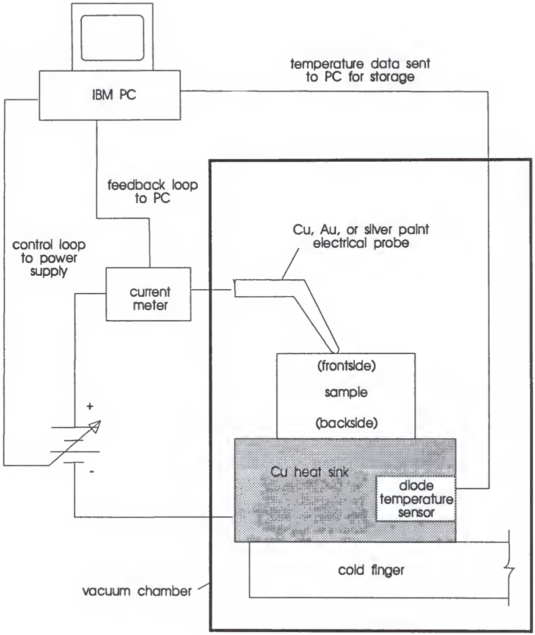

Figure 5.2: Schematic diagram showing electrical degradation apparatus. The samples were mounted on a Cu heat sink which was cooled by a cold finger. An IBM PC was used to control the power applied to the sample and to record the current , voltage , and temperature during degradation

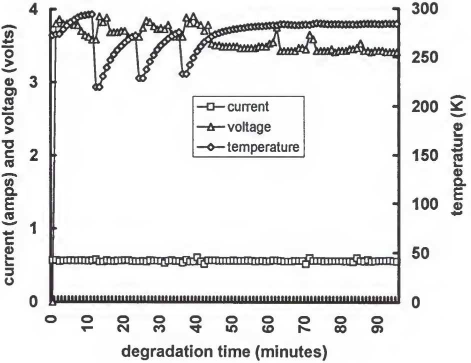

Figure 5.3: Current, voltage, and temperature for a multiquantum well contact degraded at 1500 A/cm^2 for 12, 24, 36, and 96 minutes at 287 °K. Note the temperature drop between degradation intervals.

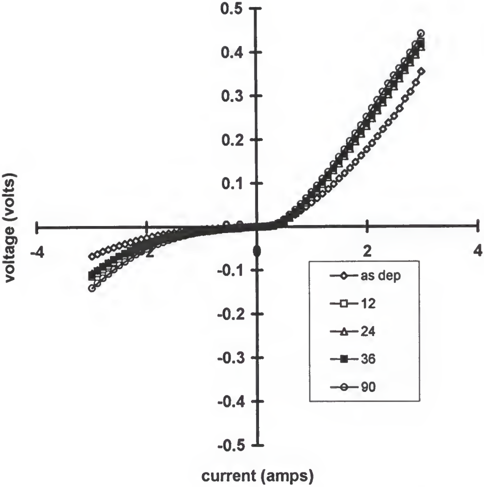

Figure 5.4: I-V curves for multiquantum well contacts as deposited, and degraded at 1500 A/cm^2 and 285 °K for 12, 24, 36, and 96 minutes. Note the recitfying nature of the I-V data from the band offset at the p-ZnSe/p-GaAs interface.

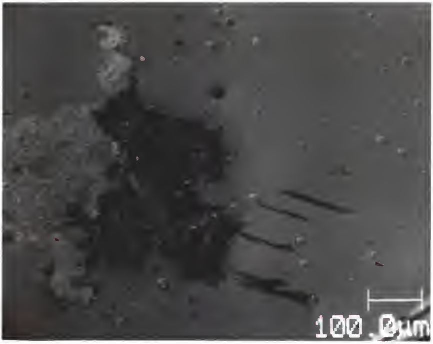

Figure 5.5: SEM micrograph showing a damaged region which occurs beneath the electrical probe's point of contact after electrical degradation.

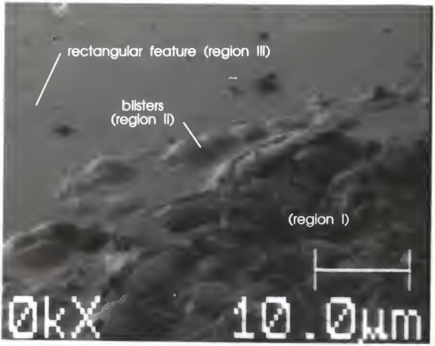

Figure 5.6: SEM micrograph showing a ring of blisters surrounding the point at which the electrical probe contacted the multiquantum well contact during degradation. Note that the point of contact was In the lower right side of the picture. Outside the ring of blisters is a relatively flat region.

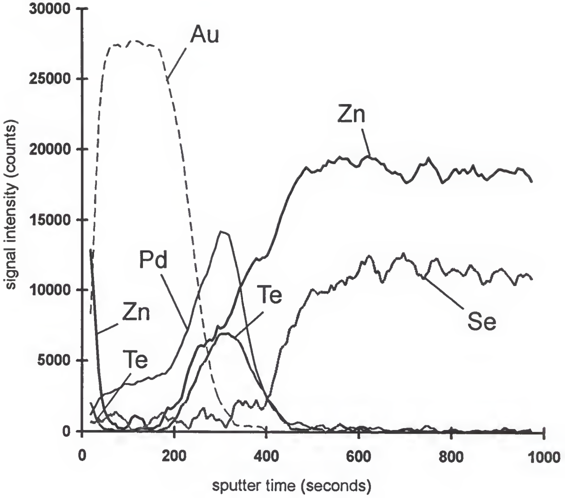

Figure 5.7: Auger depth profile taken ~20 µm from the perimeter of the Au probe's point of contact. The profile shows some alloying between Au and Pd, and a loss of Te, as compaired to non-degraded samples.

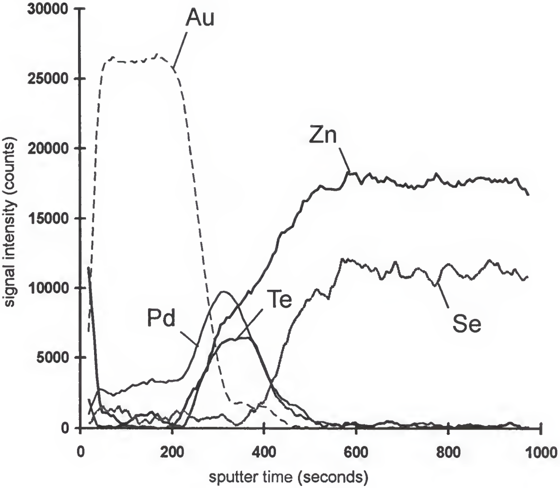

Figure 5.8: Auger depth profile taken in region II, i.e. ~10 μm away from the perimeter of the point of contact by the Au probe used to electrically degrade the sample. This profile shows that alloying between Au and Pd and a loss of Te have progressed farther than at a distance 20 μm away from the contact point (compare data in figures 5.7 and 5.8).

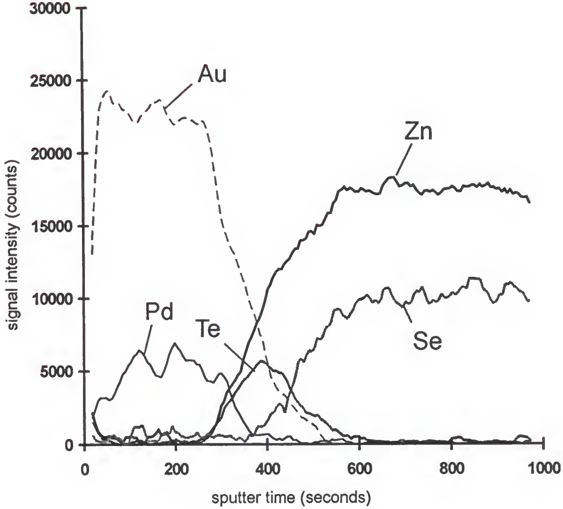

Figure 5.9: Auger depth profile taken on the edge of the point of contact by the Au probe used to electrically degrade the multiquantum well contact. The profile shows that the Au and Pd have completely alloyed.

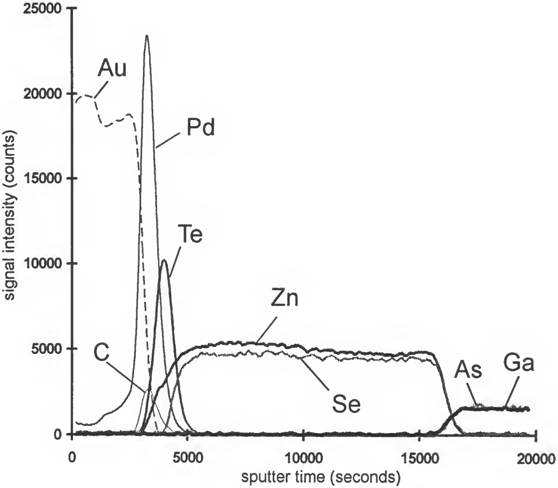

Figure 5.10: Auger depth profile of non-degraded multiquantum well contacts on p-ZnSe with Au/Pd metallizations. This profile shows well resolved Pd and Te (ZnTe) layers.

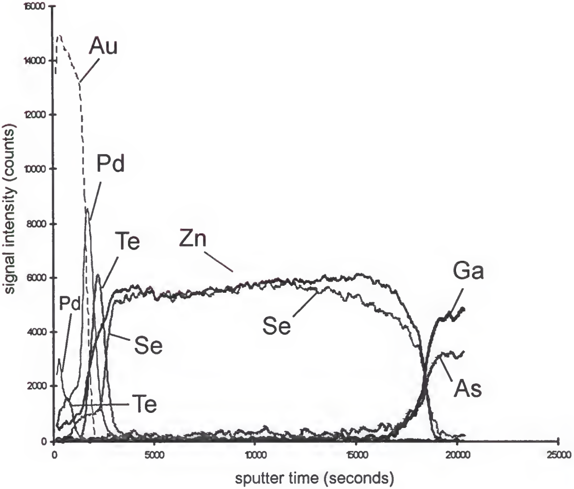

Figure 5.11: Auger depth profile from a multiquantum well contact degraded at 1500 A/cm^2 for 6 minutes at 110 °C. The depth profile shows that Te, Zn, and Se diffuse towards the surface and Pd alloyed with Au.

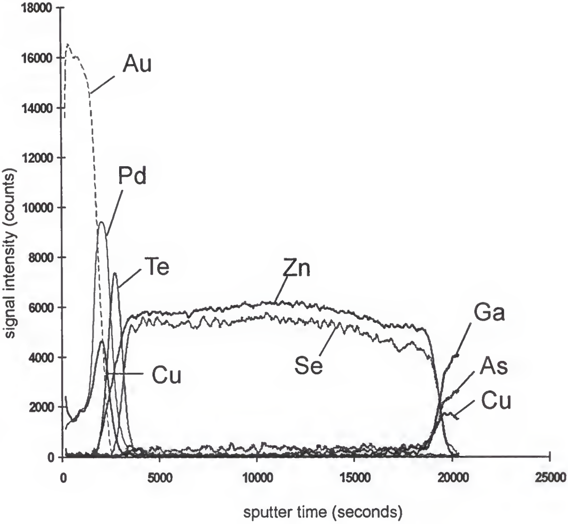

Figure 5.12: Auger depth profile through blistered region surrounding the point of contact of a Cu electrical probe following degradation at 1500 A/cm^2 for 6 minutes at 110 °C. The profile shows that Cu rapidly diffused to the ZnSe/GaAs interface. However, the Cu signal is below detectable limits through the ZnSe region.

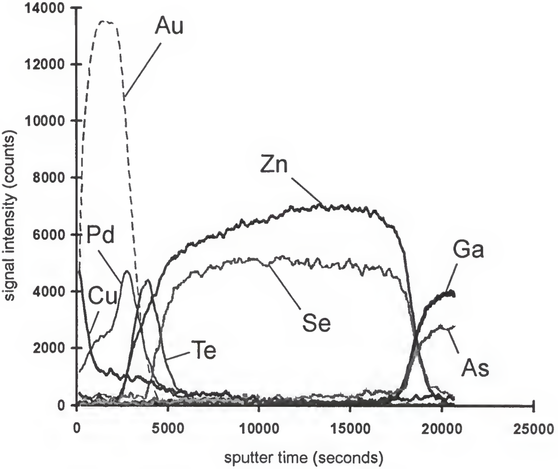

Figure 5.13: Auger depth profile from a multiquantum well contact degraded at 1500 A/cm^2 for 90 minutes at 110 °C. The profile shows greater alloying between the Au and Pd, and further loss of Te as compared to the depth profile from samples degraded for 6 minutes. In addition, a loss of Zn is observed through the top half of the ZnSe layer.

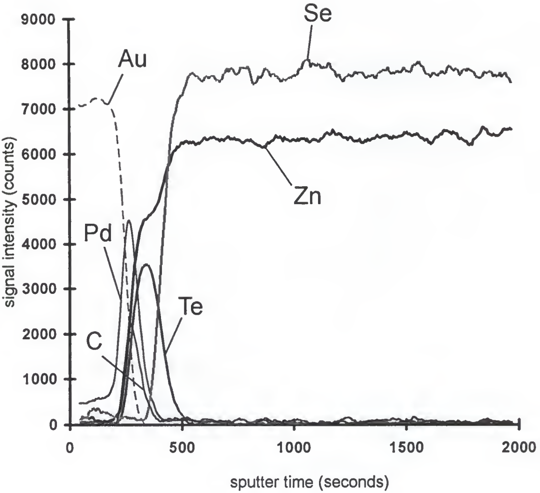

Figure 4.14: Auger depth profile from multiquantum well contact degraded at 40 A/cm^2 for 90 minutes at 14 °C. The sharp Pd peak and pronounced ZnTe layer indicate that little diffusion has occurred during degradation.

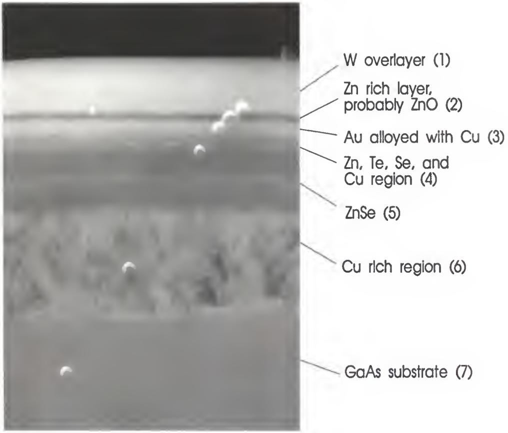

Figure 5.15: SEM micrograph from an FIB cross section through a raised blister region surrounding the Cu probe's point of contact following degradation at 1500 A/cm^2 for 20 minutes at 385 °K. Note the layered structure of the contact.

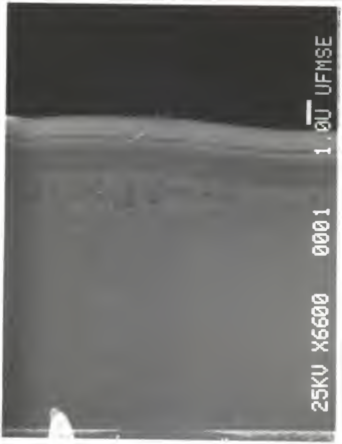

Figure 5.16: Lower magnification SEM image of FIB cross section. Note that the surface topography of the sample follows the shape of the underlying Cu rich region. Also note the defects generated by the EDS analysis.

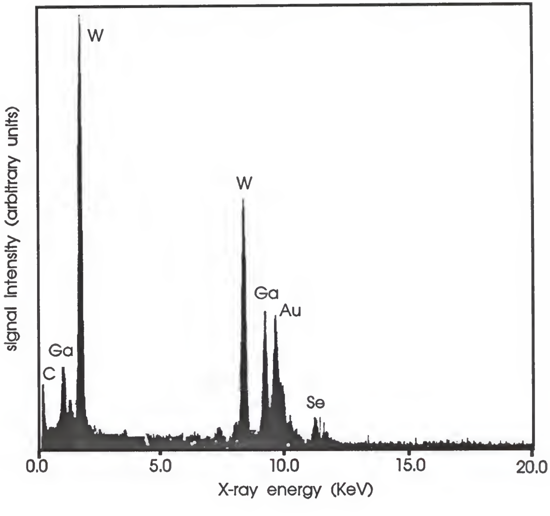

Figure 5.17: EDS data from W overlayer (1) in the degraded multiquantum well FIB cross sectional sample.

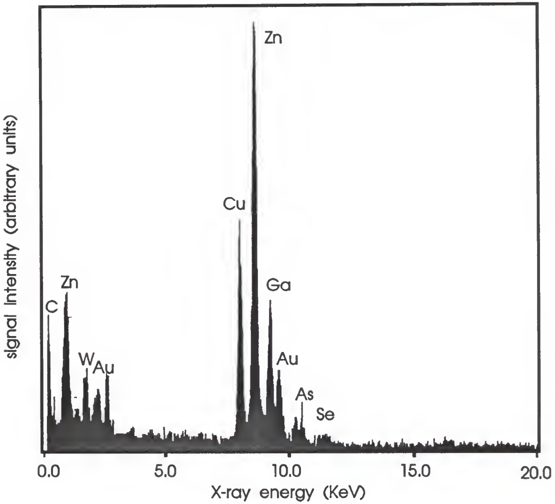

Figure 5.18: EDS data from Zn surface layer (2) in the degraded multiquantum well FIB cross sectional sample.

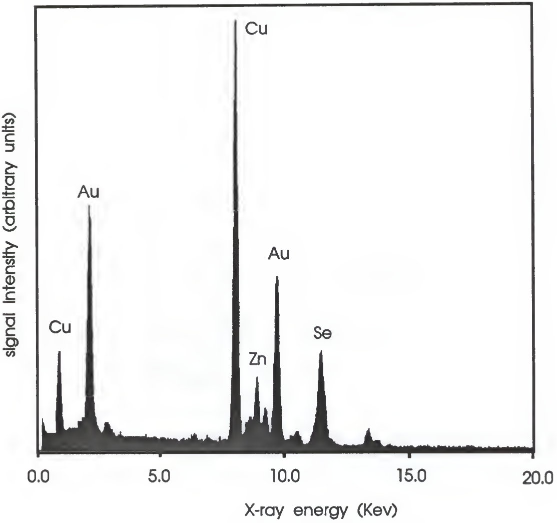

Figure 5.19: EDS data from the Au layer (3) in the multiquantum well FIB cross sectional sample. Note the high Cu signal indicating alloying between Au and Cu.

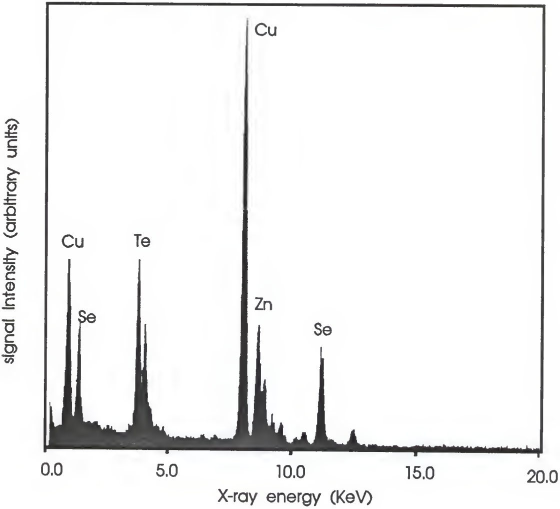

Figure 5.20: EDS data from Zn, Te, and Se region (4) of the degraded multiquantum well FIB cross sectional sample. The large Cu signal indicates that Cu is present in this region.

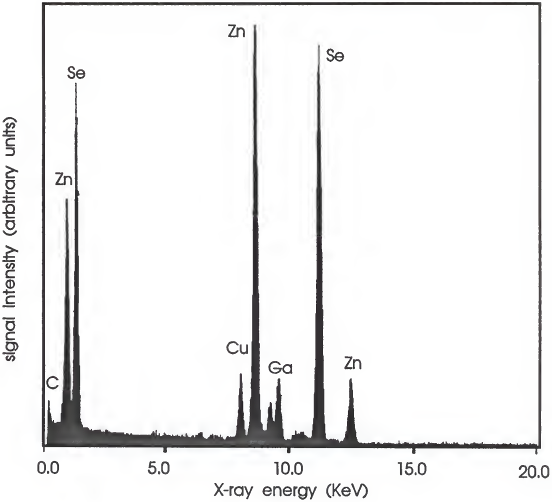

Figure 5.21: EDS data from ZnSe region (5) of the degraded multiquantum well FIB cross sectional sample. Note the relatively small Cu signal in comparison to other layers.

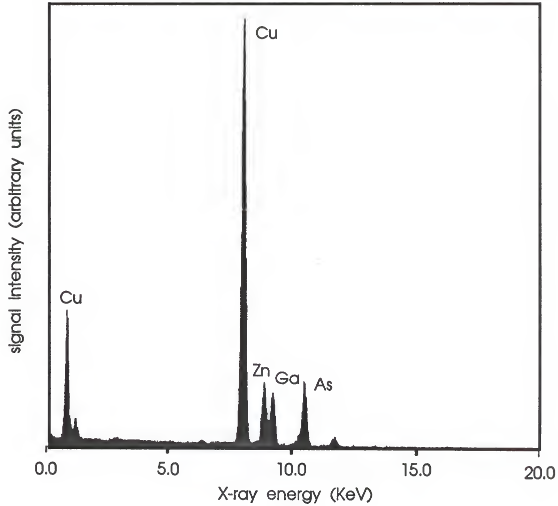

Figure 5.22: EDS data from Cu rich region (6) at the ZnSe/GaAs interface of a degraded multiquantum well FIB cross sectional sample.

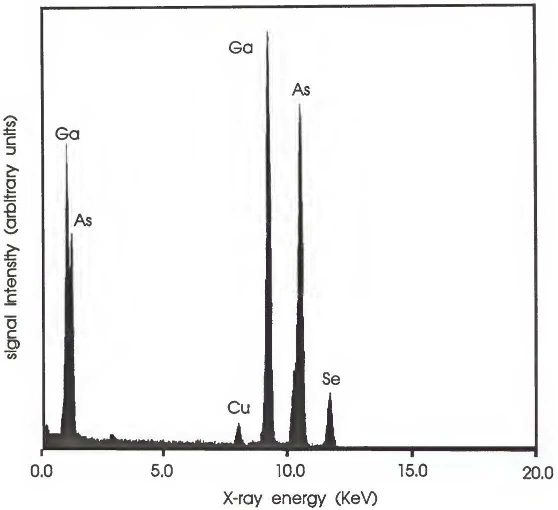

Figure 5.23: EDS data from GaAs substrate (7) of degraded multiquantum well FIB cross sectional sample.

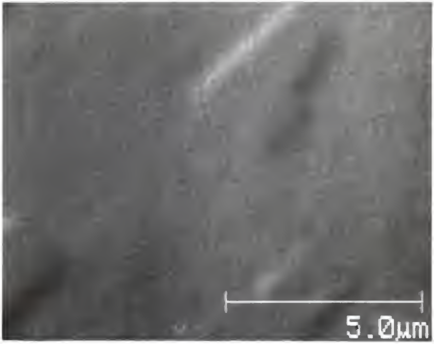

Figure 5.24: SEM micrograph showing raised rectangular features forming after degradation.

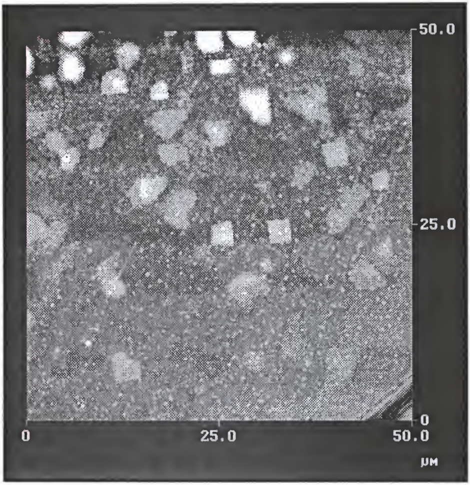

Figure 5.25: AFM image of raised rectangular features which formed following degradation. Note that the features are oriented to each other. The Cu probe was located off the top of the image where the taller (brighter) features were located.

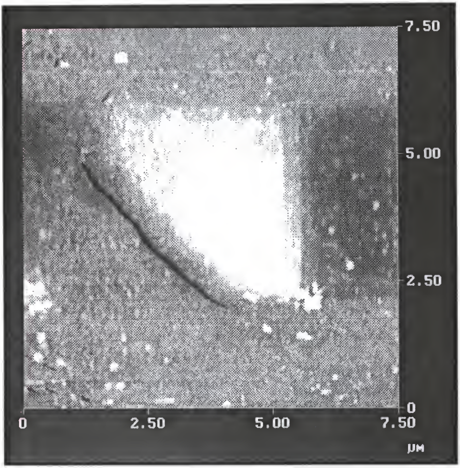

Figure 5.26: AFM image of a raised rectangular feature accompanied by a crack on the surface of a degraded multiquantum well contact. The image was obtained after the Au layer was stripped by wet chemical etching.

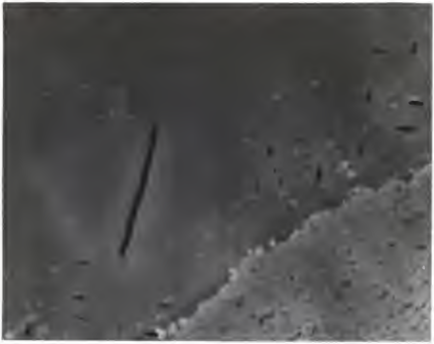

Figure 5.27: SEM image of rectangular features and an accompanying crack seen on the surface of a degraded multiquantum well contact with the metallization removed by wet chemical etching. Note that smaller cracks are observed with the sam orientation as the large crack on the rectangular feature's edge.

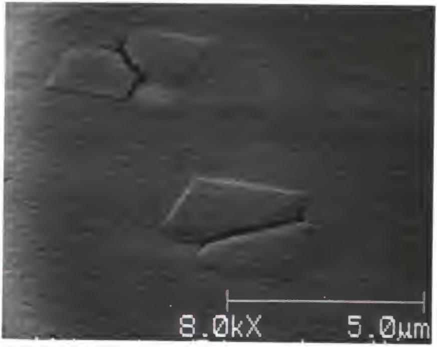

Figure 5.28: SEM micrograph of double rectangular features on either side of an elongated crack. Note propagation of the crack along <110> directions at the end of the raised features.

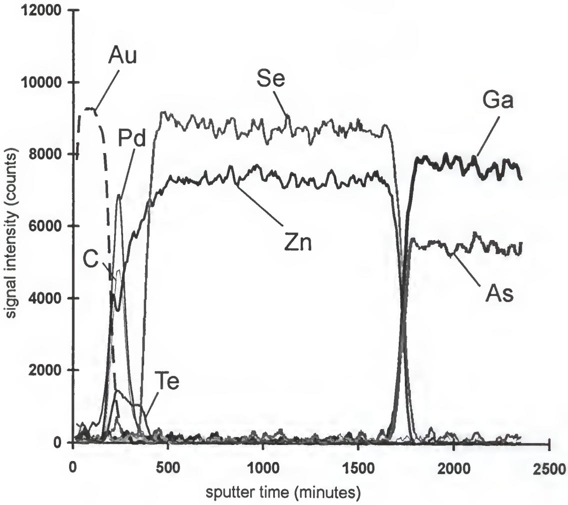

Figure 5.29: Auger depth profile from a multiquantum well contact degradation at 40 A/cm^2 for 12 hours at 110 °C using a silver paint contact. The depth profile shows a low Te signal and the formation of a Pd/Zn/Te compound as compared to the non-degraded sample (Fig. 5.10). Note the limited alloying between the Au and Pd.

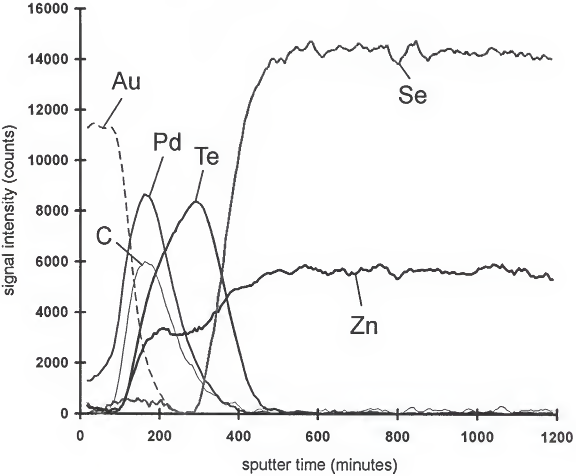

Figure 5.30: Auger depth profile from a multiquantum well contact heat treated at 200 °C for 60 minutes. The profile shows alloying between the Au and Pd, slight diffusion of Se toward the sample surface, and indicates the formation of a Pd/Zn/Te compound.

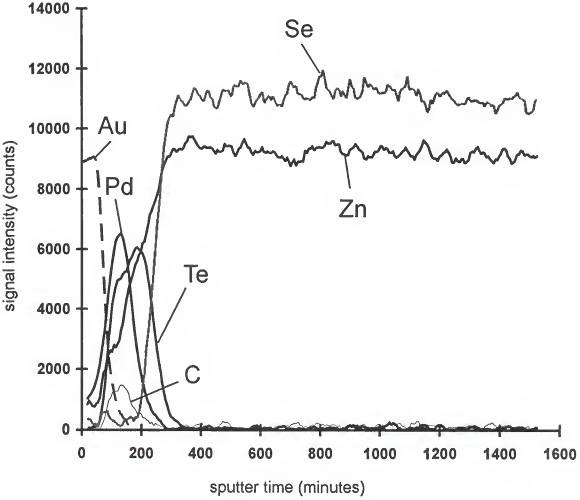

Figure 5.31: Auger depth profile from a multiquantum well contact heat treated at 300 °C for 60 minutes. The depth profile shows the formation of a Pd/Zn/Te compound at the Pd/ZnTe interface.

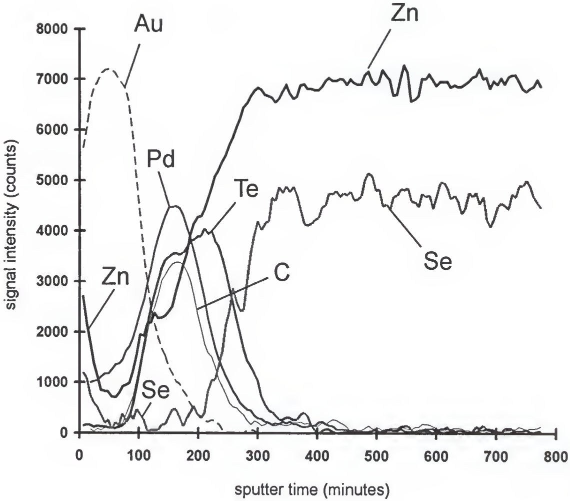

Figure 5.32: Auger depth profile from a multiquantum well contact heat treated at 400 °C for 5 minutes. The profile shows alloying between the Au and Pd, and the formation of a Pd/Zn/Te compound. Note also that Zn and Se are evident near the sample surface.

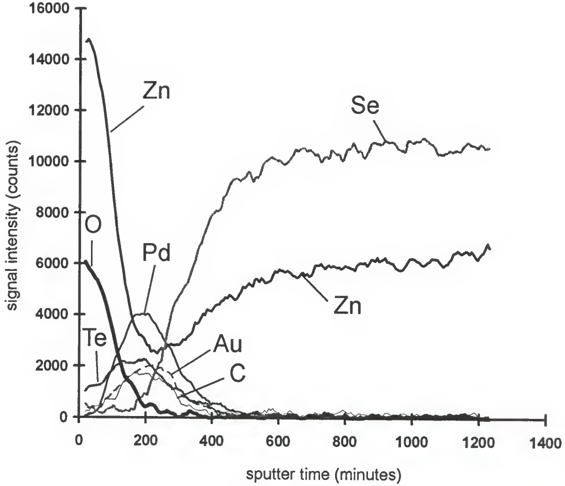

Figure 5.33: Auger depth profile from a multiquantum well contact heat treated at 400 °C for 60 minutes. The profile shows a ZnO surface layer, alloying between the Au and Pd layer, and loss of Zn and Te.

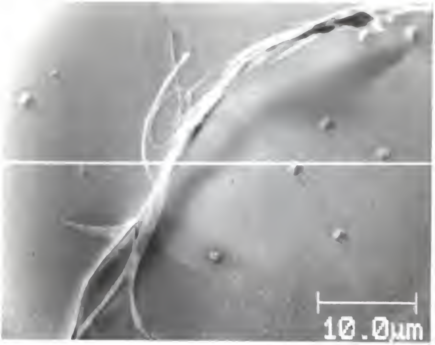

Figure 5.34: SEM micrograph showing whisker-like features which form on the surface of degraded multiquantum well contacts ~3 weeks after degradation.

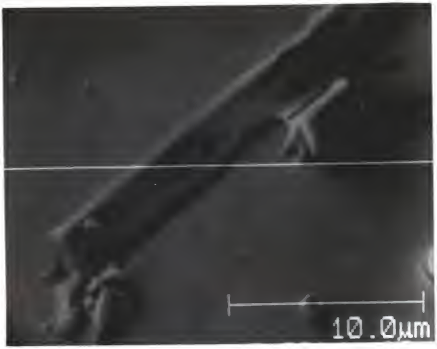

Figure 5.35: SEM micrograph showing rectangular features which form on the surface of degraded samples ~3 months after degradation.

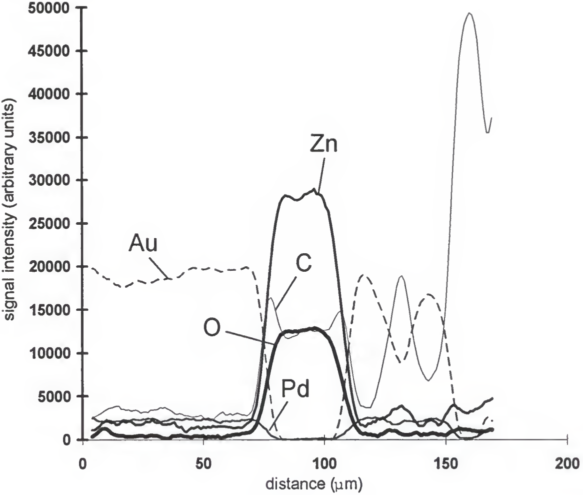

Figure 5.36: Auger line scan across crystals which formed on the surface of multiquantum well contacts 3 months after degradation. The scan shows that the crystals are composed of Zn, C, and O.

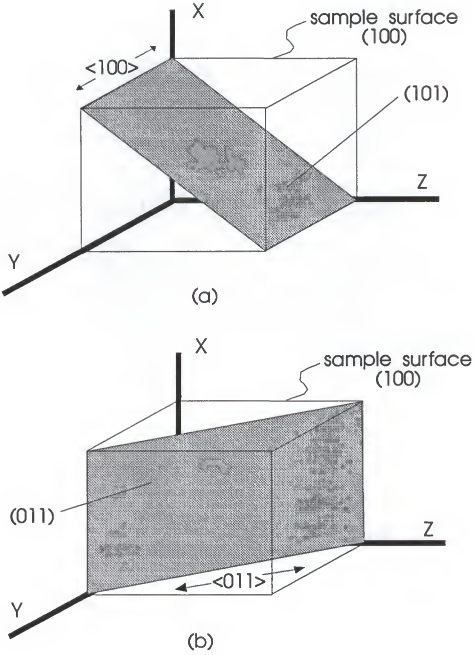

Figure 5.37: Diagram showing a) {110} cleavage planes which intersect the sample surface in the <110> directions, b) {110} cleavage planes which intersect the sample surface in the <110> directions.

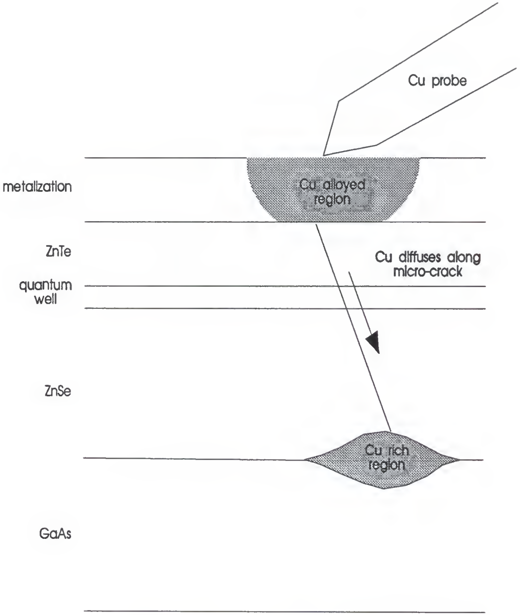

Figure 5.38: Schematic diagram of diffusion paths in multiquantum well contacts during degradation.

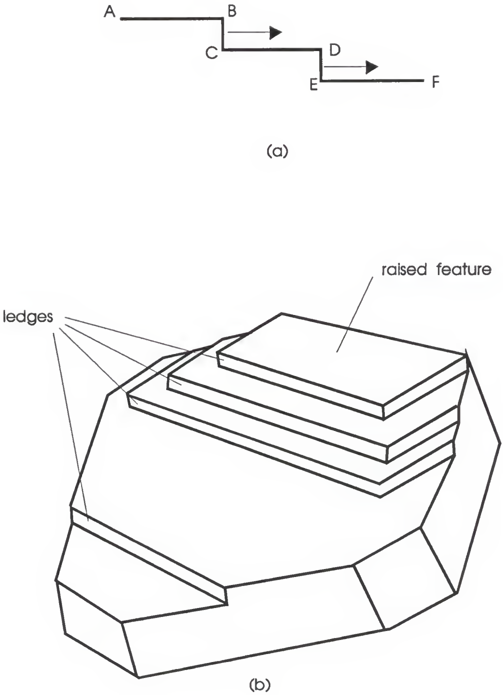

Figure 5.39: Schematic diagram showing a) side view of surface with atomic ledges. Sections AB, CD, and EF are parallel to the sample surface, and BC, and DE are the ledge faces. b) the features which result due to a ledge mechanism.

CHAPTER 6

CONCLUSIONS

Metal Contacts

Both Au and Ag contacts were observed to be rectifying in their as deposited condition. The sputter deposited Au contacts were found to have large reverse bias breakdown voltages of 12 to 15 volts prior to any heat treatment. These I-V characteristics were found to remain constant at heat treatment temperatures of 150, 200 and 300 °C for 15 minutes, but a large decrease in reverse bias breakdown voltage was observed to occur after heat treatment at 350 and 400 °C for 15 minutes. Samples heat treated at both 350 and 400 °C behaved very similar with the reverse bias breakdown voltage decreasing to ~ 3 volts after 15 minutes of heat treatment time. The breakdown voltage remained constant for heat treatment times up to 45 minutes, but increased for longer times. Following 90 minutes of heat treatment, the breakdown voltage increased to ~4 volts.

Auger sputter depth profiles and SIMS data from an Au/p-ZnSe sample, heat treated at 350 °C for 90 minutes, indicated that significant interdiffusion occurred between the Au and ZnSe. Au was observed to diffuse into the ZnSe and Zn and Se diffused into the Au layer. The diffusion of Au corresponded to the reduction in reverse bias breakdown voltage observed for the heat treated samples. The Au is believed to generate deep acceptor levels in ZnSe with ionization potentials of 550 meV which lead to defect assisted avalanche breakdown dominating in conduction of charge across the interface. The defect assisted avalanche breakdown resulted in higher conductivity across the Au/ZnSe interface at lower voltages, yielding the reduction in reverse bias breakdown observed for the samples heat treated at 350 and 400 °C.

The as sputter deposited Ag/p-ZnSe contacts were found to have a lower revers bias breakdown voltage (3.5 to 4.5 volts) as compared to the sputtered Au/p-ZnSe contacts (12 to 15 volts). Heat treatment of the Ag contacts at 150, 200, and 300 °C was observed to result in a decrease in revers bias breakdown with a minimum of ~2.3 volts reached after 45 minutes of heat treatment time. The normalized resistance of the contacts was found to increase significantly after only 15 minutes at both 200 and 300 °C, and greater resistance increases were observed following longer and higher temperature heat treatments.

Auger sputter depth profiles and SIMS data from Ag/ZnSe contacts heat treated at 150 °C for 90 minutes and 300 °C for 30 minutes showed no evidence of compound formation or diffusion. However, a large oxygen signal was observed at the Ag/ZnSe interface of the as deposited and 150 °C samples, which was also found to decrease after heat treatment at 300 °C. This oxygen, incorporated during deposition and heat treatment, is believed to act as a shallow (80 meV) co-dopant in the ZnSe resulting in higher carrier concentrations at the ZnSe surface. This in turn led to thermionic field emission currents dominating conduction, resulting in the lower reverse bias breakdown voltages observed for the heat treated Ag/ZnSe contacts.

This relation between reverse bias breakdown voltage and oxygen incorporation for Ag/ZnSe contacts was verified in additional experiments on evaporated Ag/p-ZnSe contacts. In this work, Ag/ZnSe contacts experienced a reduction in breakdown voltage from 4 volts in the as deposited case to 2.3 volts following heat treatment at 150 °C in an oxygen ambient. Similar contacts heat treated in a forming gas ambient (10% hydrogen, 90 % nitrogen devoid of oxygen) did not experience a decrease in breakdown voltage.

These results indicate the significant impact that heat treatments had on Au and Ag contacts to p-ZnSe. In the case of Au, the heat treated contacts demonstrated that the introduction of deep acceptor levels can significantly reduce the reverse bias breakdown voltage of metal/ZnSe contacts. Surprisingly, the results from heat treated Ag contacts showed that despite the smaller work function of Ag, Ag/ZnSe contacts had a breakdown voltage which was 0.7 eV lower that Au/ZnSe contacts. This indicated the potential of increasing the carrier concentration of the near surface region of nitrogen doped p-ZnSe by co-doping with oxygen.

HgSe Contacts

X-Ray, and Auger sputter depth analysis confirmed that HgSe was formed using a new *ex-situ* process discussed above. This process was shown to start with an amorphous Se (a-Se) capping layer deposited on a p-ZnSe sample prior to removal of the sample from the MBE growth chamber. Heating these samples in the presence of Hg vapor produced a metastable solid solution of Hg in a-Se. Upon heating the solid solution above the recrystallization temperature of the a-Se, HgSe precipitated out of solution. Sublimation of excess Se resulted in the formation of a stoichiometric HgSe layer. Cross sectional TEM analysis showed that the HgSe contacts formed isolated regions which were epitaxed to the underlying ZnSe substrate.

The I-V characteristics of the contacts were found to be rectifying, similar to *in-situ* grown HgSe contacts on p-ZnSe with low carrier concentrations (1×10^{17} cm^{-3}). Temperature dependant I-V measurements showed that thermionic emission dominated conduction in HgSe/p-ZnSe contacts under reverse biases of 0 to 3 volts. This data also showed that the valance band offset for the HgSe/p-ZnSe contacts was 0.55 eV. For higher reverse biases (3 to 5 volts), thermionic field emission was found to dominate conduction. The energy parameter for tunneling (E_{oo}), over the range where thermionic fields emission dominated, was found to be 0.007 eV.

Theoretical modeling of the contacts agreed with the experimental results, showing that thermionic emission dominated conduction for reverse biases of 0 to 5 volts. For greater reverse biases, thermionic field emission was calculated to dominate. The higher crossover point (5 volts) in the theoretical calculations, as compared to the experimental value (3 volts) was due to the thermionic field emission equation neglecting the effects of image force reduction.

The HgSe contacts were also found to be unstable at temperatures of 100 °C. During the temperature dependant measurements, the contacts were found to experience an irreversible increase in resistance when heated to 100 °C or above. This increase in resistance was postulated to result from a loss of Hg from the HgSe layer.

This work confirmed the existence of a valence band offset between HgSe and ZnSe and determined the value of the offset to be 0.55 eV. This indicates that even for ZnSe with higher carrier concentrations, a significant impediment to charge flow exists across HgSe/p-ZnSe interfaces. Therefore, additional modifications such as the ZnTe interfacial layers described by Ren et. Al. [Ren94] will be required to obtain ohmic contacts. However, the *ex-situ* method of forming HgSe is a viable method of producing HgSe contacts for further study. It is a much less hardware intensive process, as compared to *in-situ* MBE growth, yet produces stoichiometric, epitaxed HgSe contacts with similar electrical properties.

Multiquantum Well Contacts

The I-V data from multiquantum well contacts degraded under high current densities (1000 to 1500 A/cm^2) showed that the I-V characteristics of the contacts were constant until an abrupt failure occurred. The failure uncured due to a discontinuity in the circuit resulting from damage on the surface of the MQW structure. The damage results from diffusional processes which are accelerated by localized heating, at the point that the electrical probe (used to supply current during degradation) contacts the sample surface. The localized temperature rise occurs due to Joule heating from the high current densities in this region and may have a magnitude, as discussed below, of up to 400 °C.

The Auger sputter depth profiles from MQW contacts degraded for 20 min. at 1500 A/cm^2 and a heat sink temperature of 110 °C using an Au probe provide evidence indicating that localized heating occurs surrounding the electrical probe's point of contact. At a point 20 μm from the probe's point of contact, small amounts of Zn and Te had diffused to the sample surface, and Pd had alloyed with the Au layer. The diffusion of Zn and Te as well as alloying of Pd with Au were found to have progressed to a greater extent at a distance 10 μm, and even more still at 0 μm from the probe's point of contact. This shows that the localized temperature was greater closer to the point of contact, since these reactions are exponentially dependant on temperature.

The effects of the localized temperature on the MQW structure were studied in more detail on samples degraded using a Cu probe. Auger sputter depth profiles from samples degraded for 0, 6, and 90 minutes at 1500 A/cm^2 and a heat sink temperature of 110 °C showed that alloying Pd and Au progressed with longer degradation times. In addition, Zn and Te from the ZnTe layer diffused through the Au layer to the sample surface. These data indicated that Zn and Te continued to diffuse until the ZnTe/ZnSe quantum well was reached. For long degradation times (90 minutes), a loss of Zn from the ZnSe layer was observed, which was postulated to diffuse through the QW region to the sample surface. Following degradation using a larger probe yielding lower current densities (40 A/cm^2 for 12 hours with a heat sink temperature of 110 °C) Zn and Te were still found to have diffused to the sample surface, but no loss of Zn from the ZnSe was observed. This indicates that the degradation rate of the contact structure could be reduced through the use of larger electrical contacts which provide a better distribution of current.

The degradation was also slowed by reducing the heat sink temperature during degradation. For samples degraded for 90 minutes at 1000 A/cm^2 and a heat sink temperature of 14 °C, no alloying or diffusion was observed to occur. While cooling the structures during operation is not a desirable alternative to increase the lifetime of ZnSe devices, these results again illustrated the dependance of MQW contact degradation on temperature.

Measurement of the localized temperature beneath the probe's point of contact were difficult to achieve. A thermocouple mounted on the end of the electrical probe indicated that localized temperatures during the initial stages of degradation were up to 200 °C greater than the heat sink temperature. Once the heat sink warmed up and the temperatures in the system stabilized, the maximum localized temperatures were 150 °C greater than the heat sink. This yielded a maximum localized temperature of 260 °C for heat sink temperatures of 110 °C.

While the thermocouple measurements showed a localized temperature rise, these values are still believed to fall short of the actual temperature at the probe's point of contact. Comparison of Auger sputter depth profiles from samples heat treated at 200, 300, and 400 °C with electrically degraded samples indicated that the localized temperatures must have reached between 300 and 400 °C to produce the alloying and diffusion observed in the electrically degraded samples. At lower temperatures, a compound appeared to form between Pd and ZnTe which was not present in the electrically degraded samples.

The localized temperatures were also shown to cause micro-cracks, which formed in the region surrounding the electrical probe's point of contact. These cracks are believed to have formed during the initial stages of degradation when the heat sink was cool but the localized temperatures was increasing rapidly, and the thermal gradients were at their greatest. Stresses of

53 MPa were calculated to result from these thermal gradients, which were sufficient to cause crack propagation. The cracks were observed to intersect the sample surface (which is the (100) plane) along the <110> directions, and were believed to lie on the {110} cleavage planes. For samples degraded using Cu probes, these cracks were found to act as high diffusivity paths for impurities (Cu atoms) to diffuse into the contact structure. The Cu diffusion was observed to cause significant damage to the contact structure, due to micrometer thick regions of Cu forming at the ZnSe/GaAs interface.

Rectangular defects were also found to form on the degraded sample surfaces which were oriented to the micro-cracks. These defects were 1 to 5 μm in size and 500 to 1000 nm high. The rectangular geometry and orientation of these features to the micro-cracks resembled the dislocation patches (referred to as dark line defects) which form in the QW region of degraded ZnSe based diode lasers. This suggests the possibility that patches of dislocations also form in the quantum well region of the MQW contacts.

Due to the large amount of Zn diffusing to the surface of the electrically degraded samples, post degradation surface reactions were observed to occur. The Zn initially formed a ZnO layer upon diffusing to the sample surface. However, after several week to several months, the ZnO reacted with residual CO_2 and formed $ZnCO_3$ crystals. The driving force for the formation of $ZnCO_3$ was the difference in free energy between ZnO (-320 Kcal/mol) and $ZnCO_3$ (-731 Kcal/mol).

In conclusion, the degradation studies of MQW contacts showed that localized Joule heating (generated under high current densities) led to dissociation of the ZnTe region and diffusion of Zn and Te to the sample surface. For longer degradation times, Zn from the ZnSe regions also diffused to the sample surface, leaving behind nonstoichiometric ZnSe. The localized heating was also shown to result in the formation of micro-cracks which acted as high diffusivity paths for impurity atoms. The implications from this work for ZnSe based QW lasers are that the combination of localized heating and micro-cracking will accelerate the formation of DLDs by providing high diffusivity paths for impurities and increasing the impurities' rate of diffusion.

CHAPTER 7

FUTURE WORK

The following chapter proposes additional work to be performed in the study of electrical contacts to p-ZnSe based on the review of the literature and the results presented in this dissertation

Au and Ag Contacts

The most significant continuation of the work performed on the Au and Ag contacts would be a further study of the effects of oxygen as a co-dopant in nitrogen doped p-ZnSe. The goal of this work would be to characterize the defect states generated by oxygen in nitrogen doped p-ZnSe. These experiments would begin by fabricating Ag/p-ZnSe contacts as described in the experimental setup section of chapter 3. To control the oxygen content in the contacts, the argon used to backfill the sputter system during the deposition of Ag would be replaced with by an argon/oxygen mixture. By varying the ratio of argon to oxygen, the amount of oxygen incorporated into the contacts could be controlled.

Electrical characterization of the contacts as a function of the argon/oxygen ratio would provide additional data regarding the relation between the reverse bias breakdown voltage of Ag/ZnSe and interfacial oxygen. More importantly, characterization of the contacts by photoluminescence measurements would identify if interfacial oxygen generated defect states in the ZnSe surface region, similar to the shallow (80 meV) acceptor levels reported by Akimoto et. Al. [Aki89b]. Wet chemical etching of the Ag layer from the sample surface would expose the surface region of the ZnSe, allowing photoluminescence measurements to be performed on the exposed area. Note that similar experiments would verify the deep 550 meV acceptor levels generated by Au diffusion into the Au/ZnSe contacts.

HgSe Contacts

The results from the HgSe contacts show that the *ex situ* formation process is a viable method of forming HgSe contacts. However, while the valence band offset between HgSe and ZnSe is less than that of metal contacts, it is still large enough to prevent ohmic behavior. Ren et. Al. [Ren94] reported that *in situ* contacts were significantly improved by depositing a 100 Å interfacial layer of $ZnTe_{0.2}Se_{0.8}$. Deep levels in this heavily doped layer reportedly led to resonant tunneling, yielding ohmic behavior. Therefore, *ex situ* formed contacts should also be improved by the addition of a ZnTeSe interfacial layer.

The formation of these contacts would begin as described by Ren et. al. [Ren94]. In this work, Ren grew ZnSe and $ZnTe_{0.2}Se_{0.8}$ layers in a single MBE system, then capped them with Se for transfer to a second MBE system. To further study the *ex situ* contacts, similar structures would be grown, except they would not be transferred to the second MBE system for HgSe growth. Instead, HgSe would be formed on the Se capped samples by the *ex situ* process outlined in chapter 4. The formation of HgSe without the use of a second MBE system would represent a significant reduction in required equipment and processing complexity.

Patterning of the contacts could be accomplished by one of two methods. First, by placing a shadow mask between the sample and effusion cells, in the MBE system, after the growth of the ZnSe. This would result in the growth of independent mesa structures consisting of $ZnTe_{0.2}Se_{0.8}$ and Se layers. The *ex situ* reaction process should form HgSe from the Se capping layers on each mesa. Using this method, care would have to be taken to identify if any reactions occur on the exposed ZnSe regions between the mesas. A second, more standard approach would be to etch mesa structures in to the sample following the growth of the ZnSe, $ZnTe_{0.2}Se_{0.8,}$ layers and *ex situ* formation of HgSe.

By repeating the temperature dependant I-V measurements on the contacts with the ZnTeSe interfacial layer, the activation energy for tunneling through the interfacial layer would be determined. This would serve as a measure of comparison between the samples with and without the interfacial layer. Provided the contacts yielded ohmic behavior, as in the *in situ* case, transmission line measurements could be used to determine the specific contacts resistance of HgSe/$ZnTe_{0.2}Se_{0.8}$/ZnSe contacts. This would act as a measure of comparison between these contacts and multiquantum well contacts.

Multiquantum Well Contacts

In chapter 5 of this dissertation, MQW contacts were studied to identify degradation mechanisms and potential links between contact degradation and the degradation of ZnSe based LEDs and laser diodes. The work was limited to studying structures which consisted of MQW contacts on ZnSe epilayers, but without an active light emitting region. This configuration was chosen so that an in depth study of the contact structure alone could be performed. The results indicated solute and solvent diffusion as well as micro-crack formation occur in the degraded contacts, all of which were postulated to accelerate the degradation of LEDs and laser didoes.

Based on these results, continuing studies should be performed to directly observe the effect of MQW contact degradation on ZnSe diode structures. This work could be performed by repeating the high current electrical degradation, described in the experimental setup section of chapter 4, on samples which consist of a MQW contact on ZnSe based single QW laser structures. SEM and

AFM images of the sample surfaces following degradation could be used to identify any micro-cracks formation and Auger depth profiles could be used to indicate any diffusion of solute or solvent atoms through the structure.

In chapter 5, the problem of micro-cracking was alleviated by increasing the size of the electrical probe used to supply power during electrical degradation. However, the diffusion of Zn and Te from the ZnTe layer was observed to be a more persistent problem which occurred even with the large area silver paint contacts. Therefore, further research should be aimed at identifying methods to prevent the diffusion of these species.

The Au/Pd metallization has been shown to produce contacts to ZnTe with low specific contact resistances and has been readily incorporated into the MQW contacts. However, Ozawa et. al. [Oza93] indicates that Pd is disruptive to ZnSe and was incorporated into the contacts to increase the reactivity between the Au and ZnTe layers. Therefore, the degree of reactivity between Pd and ZnTe should be studied to determine if reactions between Pd an ZnTe are leading to the large amounts of Zn and Te diffusing out of the contact structure.

The reaction between Au/Pd and ZnTe metllizations should begin with samples fabricated by depositing a Pd layer, followed by an Au layer onto ZnTe substrates. The ratio of Au and Pd layer thicknesses should be varied to provide a matrix of samples. In order to keep the results relevant to the device structures, the range of the Pd layer thickness should be between ~ 0 and 300 Å, while the Au layer should be between ~ 0 and 3000 Å. Since the results in chapter 5 indicated that the diffusion of Zn and Te was primarily a thermally activated process, the samples could be heat treated as opposed to electrically degraded. The heat treatment range should vary between 0 and 500 °C. Auger depth profiles could then be used to identify compositonal profiles through the heat treated structures and cross sectional TEM analysis would provide detailed information concerning compound or defect formation.

Additional experimental work which would be important to understanding the degradation of MQW contacts would be plan view TEM analysis of the degraded MQW contacts in the region where the rectangular raised features were observed. As indicated in the discussion section of Chapter 5, the similarity between the rectangular features oriented about the micro-cracks and DLDs in degraded laser structures suggest that dislocation patches may be forming in the quantum well region of the MQW contacts. Plan View TEM images were used by Hovinen et. al. [Hov95] and Hua et. al. [Hua94] to identify the dislocation patches in degraded laser structures. Therefore, similar plan view TEM analysis could be used on electrically degraded samples (as described in the experimental setup section of chapter 5) to characterize defect formation in the region of degraded MQW contacts containing raised rectangular features. This would verify to origin of the rectangular features and potentially identify additional relationships between the degradation of MQW contacts and the active region of light emitting devices.

REFERENCES

Aki89a Akimoto, K., Miyajima, T., & Mori, Y., J. Appl. Phys., **28**, L531 (1989)

Aki89b Akimoto, K., Miyajima, T., & Mori, Y., Phys. Rev. B, **39**, 3138 (1989)

Aki91 Akimoto, K., Miyajima, T., Okuyama, H., & Mori, Y., J. Cryst. Growth, **115**, 683 (1991)

And93 Anderson, S., Laser Focus World, **8**, 27 (1993)

Ask94 Askeland, D., The Science and Engineering of Materials, Third Edition, (PWS Publishing, Boston, MA, 1994) p. 708

Ave61 Aven, M., Marple, D., & Segall, B., J. Appl. Phys. Supp., **32**, 2261 (1961)

Bar47 Bardeen, J., Phys. Rev., **71**, 717 (1947)

Bel94 Belsinger, H., Wilner, B., Tach, U., Topoleski, L., Engng Fracture Mech., **48**,199 (1994)

Bes76 Best, J., Mcaldin, J., McGill, T., Mead, C., & Mooney, J., Appl. Phys. Lett., **29**, 433 (1976)

Che94 Chen, W., Kahn, A., Soukiassian, P., Mangat, P., Gaines, J., Ponzoni, C., & Olego, D., J. Vac. Sci. Technol. B, **12**, 2693 (1994)

Dea82 Dean, P., Fitzpatrick, B., & Bhargava, R., Phys. Rev., **26**, 2016 (1982)

Die86 Dieter, G., Mechanical Metallurgy, Third Edition, (McGraw-Hill, New York, 1986)

Dux95 Duxstad, K., Haller, E.,Washburn, J., Yu, K., Bourret, E., Walker J., & Lin, X., Appl. Phys. Lett., **67**, 947 (1995)

Ebe92	Eberhart, M., Donovan, M., Outlaw, R., Phys. Rev. B, **46**, 12744 (1992)
Ekp90	Ekpenuma, S., & Mylew, C., J. Phys. Chem. Solids, **51**, 93 (1990)
Eri88	Ericson, F., Johansson, S., and Schweitz, J., Mater. Sci. Eng., **A105/106**, 131(1988)
Fan92	Fan, Y., Han, J., He, L., Saraie, J., Gunshore, R., Hagerott, M., Jeon, J., Nurmikko, A., Hua, G., & Otsuka, N., Appl. Phys. Lett., **61**, 3160 (1992)
Fan93	Fan, Y., Han, J., He, L., Saraie, J., Gunshore, R., Hagerott, M., Jeon, H., Nurmikko, A., Hua, G., & Otsuka, N., J. Vac. Sci. Technol. B, **11**, 1748 (1993)
Gai93	Gaines, J., Drenten, R., Haberern, K., Menz, P., & Petruzzello, J., Appl. Phys. Lett., **62**, 2462 (1993)
Guh94	Guha, S., Cheng, H., Depuydt, J., Haase, M., & Qui, J., Mat. Sci. Eng., **B28**, 29 (1994)
Haa90	Haase, M., Cheng, H., Depuydt, J., & Pots, J., J. Appl. Phys., **67**, 448 (1990)
Haa91	Haase, M., Qui, J., Depuydt, J., & Cheng, H., Appl. Phys. Lett., **59**, 1272 (1991)
Hal50	Hall, R., & Dunlap, W., Phys. Rev., **80**, 467 (1950)
Han58	Hanson, M., Constitutiona of Binary Alloys, (McGraw-Hill, New York, 1958) p. 386
Hel93	Helms, C., Jpn. J. Appl. Phys., **32**, 1558 (1993)
Hie93	Hiei, F., Ikeda, M., Ozawa, M., Miyajima, T., Ishibashi, A., & Akimoto, K., Electronics Lett., **29**, 878 (1993)
Hov95	Hovinen, M., Ding, J., Salokatve, A., Nurmikko, A., Hua, G., Grillo, D., He, L., Han, J., Ringle, M., & Gunshor, R., J. Appl. Phys., **77**, 4150 (1995)
Hsu88	Hsu, C., & Faurie, J., J. Vac. Sci. Technolo. B, **6**, 773 (1988)

Hua94	Hua, G., Otsuka, N., Grillo, D., Fan, Y., Han, J., Ringle, M., Gunshor, R., Hovinen, M., & Nurmikko, A., Appl. Phys. Lett., **65**, 1331 (1994)
Jon88	Jonker, B., Krebs, J., & Prinz, G., J. Appl. Phys., **63**, 5885 (1988)
Kas87	Kasap, S., & Juhasz, C., J. Mater. Sci. Lett., **6**, 397 (1987)
Kas93	Kasap, S., Aiyha, V., & Yannacopoulos, S., J. Phys. D, Appl. Phys., **23**, 553 (1993)
Kol88	Kolodziejski, L., Gunshor, R., Fu, Q., Lee, D., Nurmikko, A., Gonsales, J.,& Otsuka, N., Appl. Phys. Lett., **52**, 1080 (1988)
Kot92	Kotkata, M., J. Mat. Sci., **27**, 4847 (1992)
Kum76	Kumazari, K., Matsushima, E., & Odajima, A., Phys. Stat. Sol. A, **37**, 579 (1976)
Lan92	Lansari, Y., Ren, J., Sneed, B., Bowers, K., Cook, J., & Schetzina, Appl. Phys. Lett., **61**, 2554 (1992)
Lan93	Lansari, Y., Cook, J., & Schetzina, J., J. Elect. Mat., **22**, 809 (1993)
Lar81	Larmagnac, J., Grenet, J., & Michon, P., J. Non-Crystalline Solids, **45**, 157 (1981)
Lid93	Lide, D., (editor) CRC Handbook of Chemistry and Physics, 74th edition, (CRC Press, Boca Raton, 1993) p. 5-20, 5-25
Lid95	Lide, D., (editor) CRC Handbook of Chemistry and Physics, 76th Edition, (CRC press, Boca Raton, 1995)
Man63	Mandel, G., Phys. Rev., **134**, A1073 (1963)
Mcc88	McClune, W., (editor) Inorganic Phases, (International center for Diffration Data, Swarthmore, PA, 1988)
Miy92	Miyajima, T., Okuyama, H., & Akimoto, K., Jpn. J. Appl. Phys., **31**, L1743 (1992)

Ohk87 Ohkawa, K., Mitsuyu, T., & Yamazaki, O., J. Appl. Phys., **62**, 3216 (1987)

Ohk91 Ohkawa, K., Karasawa, T., & Mitsuyu, T., Jpn. J. Appl. Phys., **30**, L152 (1991)

Ohk92 Ohkawa, k., Ueno, A., & Mitsuyu, T., J. Cryst. Growth, **117**, 375 (1992)

Out92 Outlaw, R., Wu. D., Davidson, M., & Hoflund, G., J. Vac. Sci. Technol. A, **10**, 1497 (1992)

Oza93 Ozawa, M., Hiei, F., Ishibashi, A., & Akimoto, K., Electron. Lett., **29**, 503 (1993)

Oze90 Ozenbas, M., Vacuum, **41**, 1339 (1990)

Pad66 Padavani, F., & Stratton, R., Solid. St. Electron., **9**, 695 (1966)

Par77 Park, Y., & Shin, B., Topics Applied Phys., **17**, 133 (1977)

Par90 Park, R., Troffer, M., Rouleau, C., Depuydt, J., & Hase, M., Appl. Phys. Lett., **57**, 2127 (1990)

Pau60 Pauling, L., The Nature of the Chemical Bond, 3rd Edition, (Cornell University Press, New York, 1960) p. 93

Por81 Porter, D., & Easterling, K., Phase Transformations in Metals and Alloys, (T.J. Press (Pastow) Ltd., Great Britain, 1981) p. 176

Qui91 Qui, J., Depuydt, J., Cheng, H., & Haase, M., Appl. Phys. Lett., **59**, 2992 (1991)

Qui93 Qui, J., Cheng, H., Depuydt, J., & Hasse, M., J. Cryst. Growth, **127**, 279 (1993)

Ren91 Ren, J., Bowers, K., Hwang, S., Cook, J., & Schetzina, J., J. Cryst. Growth, **111**, 772 (1991)

Ren94 Ren, J., Eason, D., Churchill, L., Yu, Z., Boney, C., Cook, J., Schetzina, J., & El-Maery, A., J. Crys. Growth, **138**, 455 (1994)

Rou92 Rouleau, C., & Park, R., Appl. Phys. Lett., **60**, 2723 (1992)

Rou93 Rouleau, C., & Park, R., J. Appl. Phys., **73**, 4610 (1993)

Rud86 Ruda, H., J. Appl. Phys., **59**, 1220 (1986)

Sch38 Schottky, Naturwissenchaften, **26**, 843 (1938)

Sch39 Schottky, W., Spenke, E., Wiss. Veroff. Siemens-Werken, **18**, 225 (1939)

Scr77 Scranton, R., Best, J., & McCaldin, J., J. Vac. Sci. Technol., **14**, 930 (1977)

Sha84 Sharma, B., Metal-Semiconductor Schotky Barrier Junctions and Their Applications, (Plenum Press, New York, 1984)

Shi80 Shirakawa, Y., & Kukimoto, H., J. Appl. Phys., **51**, 2014 (1980)

Shu69 Shunk, F., Constitution of Binary Alloys, Second Supplement, (McGraw-Hill, New York, 1969) p. 433

Swa66 Swank, R., Phys. Rev., **153**, 844 (1966)

Sze81 Sze, S., Physics of Semicondictor Devices, (J. Wiley & Sons, New York, 1981)

Sze85 Sze, S., Semiconductor Device Physics and Technology, (J. Wiley & Sons, New York, 1985)

Tru92 Truman, J., Sputter Deposition of Y-Ba-Cu-O Superconductor and SrTio-b3.S Barrier Layer Thin Films, Thesis (Ph.D.), University of Florida, Gainesville, FL (1992)

Vos88 Vos, M., Xu, F., Weaver, J., & Cheng, H., Appl. Phys. Lett., **53**, 1530 (1988)

Wag31 Wagner, C., Phys. A., **32**, 641 (1931)

Wan92 Wang, Y., & Holloway, P., Vacuum, **43**, 1149 (1992)

Wea76 Weast, R., CRC Handbook of Chemistry and Physics (CRC Press, Cleavland, Ohio, 1976) p. E-101

Wer94 Werner, K., IEEE Spectrum, **31**, 30 (1994)

Whi36 Whitney, L., Phys. Rev., **50**, 1154 (1936)

Wil81 Willardson, R., & Beer, A., Semiconductors and Semimetals, (academic Press, New York, 1981) P. 69

Wil85 Wilmsen, C., Physics and Chemistry of III-V Compound Semiconductor Interfaces, (Plenum Press, New York, 1985) p. 129

Woo81 Woodall, J., Freeouf, J., Pettit, G., Jackson, T., & Kirchner, P., J. Vac. Sci. Technol., **19**, 626 (1981)

Woo90 Woodall, J., Hodgson, R., & Gunshore, R., Appl. Phys., Lett., **58**, 379 (1990)

Xu88 Xu, F., Vos, M., Weaver, H., & Cheng, Phys. Rev. B, **38**, 13418 (1988)

Yas88 Yasutake, K., Konishi, Y., Adachi, K., Yoshii, K., Umeno, M., Kawabe, H., **27**, 2238 (1988)

Yas94 Yassievich, I., Semicond. Sci. Technol., **9**, 1433 (1994)

Zor93 Zory, P., Conference Proceedings, Laser and Electro-Optics Society Annual Meeting 1993, Published by IEEE, IEEE service center, Piscataway, NJ, USA, 93CH3297-9, p. 645

BIOGRAPHICAL SKETCH

John Joseph Fijol was born on September 28, 1966, in Hartford, CT and was raised in Longmeadow, MA. He attended Longmeadow High School from 1980 to 1984 and upon completing high school, he pursued further education in the field of engineering. He was accepted into the School of Engineering at Western New England College and took up studies in electrical engineering from 1984 to 1988. In May of 1988, John graduated cum laude from Western New England College with his bachelor's degree in electrical engineering. In June of 1988, he was hired by Galileo Electro-Optics as a Development Engineer. During his employment at Galileo, John's work involved the development of novel electron multipliers which resulted in publications and the issuing of a U.S. patent, on which John was the sole inventor. At the advice of his colleagues, John left Galileo in August 1991 to attend graduate school in the field of materials science and engineering at the University of Florida in Gainesville, FL. Under the supervision of Dr. Paul Holloway, John studied ohmic contacts to p-type ZnSe. As a result of his graduate studies, John received his masters degree in materials science and engineering in December 1994 and his doctoral degree in materials science and engineering in May 1996.

I certify that I have read this study and that in my opinion it conforms to acceptable standards of scholarly presentation and is fully adequate, in scope and quality, as a dissertation for the degree of Doctor of Philosophy.

Paul H Holloway

Paul H. Holloway, Chairman
Professor of Materials Science
and Engineering

I certify that I have read this study and that in my opinion it conforms to acceptable standards of scholarly presentation and is fully adequate, in scope and quality, as a dissertation for the degree of Doctor of Philosophy.

C R Abernathy

Cammy R. Abernathy
Professor of Materials Science
and Engineering

I certify that I have read this study and that in my opinion it conforms to acceptable standards of scholarly presentation and is fully adequate, in scope and quality, as a dissertation for the degree of Doctor of Philosophy.

R. E. Hummel

Rolf E. Hummel
Professor of Materials Science
and Engineering

I certify that I have read this study and that in my opinion it conforms to acceptable standards of scholarly presentation and is fully adequate, in scope and quality, as a dissertation for the degree of Doctor of Philosophy.

Robert Park.

Robert M. Park
Professor of Materials Science
and Engineering

I certify that I have read this study and that in my opinion it conforms to acceptable standards of scholarly presentation and is fully adequate, in scope and quality, as a dissertation for the degree of Doctor of Philosophy.

Peter S Zory

Peter S. Zory
Professor of Electrical
Engineering

This dissertation was submitted to the Graduate Faculty of the College of Engineering and to the Graduate School and was accepted as partial fulfillment of the requirements for the degree of Doctor of Philosophy.

May, 1996

Winfred M. Phillips
Dean, College of Engineering

Karen A. Holbrook
Dean, Graduate School